

UNIVERSITY OF NAPLES “FEDERICO II”

Department of Electrical Engineering
and Information Technology (DIETI)

Ph.D. COURSE IN ELECTRICAL ENGINEERING



Ph.D. thesis in Power Electronics:

GRID-CONNECTED DOUBLE-STAGE AC-AC POWER CONVERTER FOR CSP RENEWABLE ENERGY SYSTEMS

Tutor:
Prof. **Santolo Meo**

Ph.D. student:
Ing. **Vincenzo Sorrentino**

Assistant Tutor:
Ing. **Francesco Esposito**

Ph.D. Coordinator:
Prof. **Claudio Serpico**

XXVII cycle

CONTENTS

ACKNOWLEDGEMENTS	iv
PREFACE	1
<i>Chapter 1: CONCENTRATING SOLAR PLANT FOR COMBINED GENERATION OF HEAT AND POWER</i>	3
1.1 Introduction	3
1.2 CSP subsystem	5
1.2.1 Parabolic Mirror	6
1.2.2 Receiver Tube	8
1.3 Thermodynamic subsystem	10
1.4 Electrical subsystem	13
<i>Chapter 2: SLIDING MODE CONTROL</i>	15
2.1 Classic Sliding Mode Control	16
2.1.1 Existence Conditions of Sliding Mode	19
2.2 Chattering phenomenon	24
2.2.1 Boundary layer technique	25
2.2.2 Observed-based technique	28
2.2.3 Disturbance rejection technique	30
2.3 Discrete-time Sliding Mode Control	32
2.3.1 Discrete-time sliding mode control design	33
2.4 Continuous-time Integral Sliding Mode Control	38
2.4.1 Continuous-time Integral Sliding Mode Control design	39

2.5 Discrete-time Integral Sliding Mode Control	42
2.5.1 Discrete-time Integral Sliding Mode Control design	42
2.5.2 Discrete-time Integral Sliding Mode Control with Disturbances Compensation and Reduced Chattering	47
2.6 Higher-Order Sliding Mode Control	53
2.6.1 2-Sliding Mode Control	54
2.6.1.1 Twisting Algorithm	55
2.6.1.2 Super-Twisting Algorithm	57
2.7 Sliding Mode Observer	59
2.7.1 Conventional Observer	59
2.7.2 Sliding Mode Observer design	60
<i>Chapter 3: ELECTRICAL SUBSYSTEM: MODELING AND DESIGN</i>	63
3.1 Stage 1: Components Modeling and Control Strategy	66
3.1.1 Permanent Magnet Synchronous Generator	66
3.1.2 Three-phase PWM rectifier	67
3.1.3 Control Strategy of Stage 1	69
3.1.3.1 Back-EMFs and rotor angle Sliding Mode Observer	70
3.1.3.2 DC-link Voltage Integral Sliding Mode Controller	72
3.1.3.3 Super-Twisting Integral Sliding Mode Controller 1	75
3.2 Stage 2: Components Modeling and Control Strategy	79
3.2.1 Three-phase Soft-Switched Voltage Source Inverter (VSI)	79
3.2.2 Control Strategy of Stage 2	84
3.2.2.1 Calculation of d-q axis reference components of grid-utility currents	85
3.2.2.2 Super-Twisting Integral Sliding Mode Controller 2	88
3.3 Analysis and Design of Electrical Subsystem	93

3.3.1 Permanent Magnet Synchronous Generator design	93
3.3.2 Quasi-Resonant branch design	105
3.3.3 Discrete-time Space Vector PWM	106
Chapter 4: NUMERICAL AND EXPERIMENTAL RESULTS	108
4.1 Numerical Results	111
4.1.1 Simulation 1: $P^* = 6\text{kW}$; $Q^* = 0\text{kVAr}$ ($v_{dc}^* = 600\text{V}$)	111
4.1.2 Simulation 2: $P^* = 6\div 3\text{kW}$; $Q^* = 0\text{kVAr}$ ($v_{dc}^* = 600\text{V}$)	120
4.1.3 Simulation 1: $P^* = 3\text{kW}$; $Q^* = 0\div 3\text{kVAr}$ ($v_{dc}^* = 600\text{V}$)	130
4.1.4 Simulation 4: $i_{L,d}^* = 6.15\text{A}$; $i_{L,q}^* = 0\text{A}$ ($v_{dc}^* = 600\div 500\text{V}$)	141
<i>Discussion of numerical results</i>	149
4.2 Experimental Results	150
<i>Discussion of experimental results</i>	155
CONCLUSIONS	156
REFERNECES	159

ACKNOWLEDGEMENTS

This work was carried out with the essential support of many people who helped me with their knowledge, their time and most of all, with their friendship. Therefore, I wish to first express my gratitude to my tutor, Prof. Santolo Meo, who supported and encouraged me from the Power Electronics exam, to this PhD thesis.

Moreover I would thank Ing. Francesco Esposito for his time, for all the encouragements, discussions and suggestions, necessary to my PhD experience.

At last I would thank Federica and my family for standing me, for their day by day support.

PREFACE

In the last years the renewable energy sources have known a state of their advanced diffusion considering their advantages compared to the traditional energy sources like fossil fuels. For this reason the combined heat and power (CHP) plant fueled by renewable sources are widely used.

The purpose of this Ph.D. thesis is the design of a new Grid-connected Double-Stage AC-DC/DC-AC Power Converter (DSACPC) for a Concentrating Solar plant for Combined generation of Heat and Power (CS-CHP), that consists of a thermodynamic sub-system fueled by sunlight and an grid-connected electrical sub-system.

The thermodynamic sub-system converts the high-temperature heat, achieved using mirrors to concentrate the sun rays to a receiver tube crossed by thermal fluid, into mechanical energy by means of a coupled Organic Rankine Cycle (ORC). Such mechanical energy outlet by turbine is input to electrical sub-system that uses it to generate active and reactive instantaneous power on the grid supply.

The main advantages of grid-connected CS-CHP proposed are CO₂ emissions operating costs more low and operating costs more content than traditional energy sources, because it use a renewable energy source. However due to some drawbacks like low efficiency of the stream cycle, caused by low operating temperature (400°C for synthetic oil), and high cost of installing (i.e. the Concentrating Solar Plants are much larger than photovoltaic plant), it is necessary maximize efficiency of the electrical sub-system so to maximize the global efficiency of proposed plant.

Therefore a new Grid-connected Double-Stage AC-DC/DC-AC Power Converter (DSACPC) with Second-Order Super-Twisting Integral Sliding

Mode Control for electrical sub-system is proposed, in order to make competitive the grid-connected CS-CHP in small scale application.

The thesis is so structured: in Chapter 1 an overview of CS-CHP systems is given and CSP and thermodynamic sub-systems are described; in Chapter 2 the sliding mode control theory is thoroughly investigated, starting to classical sliding mode control to discrete-time integral sliding mode control and the higher-order sliding mode control; in Chapter 3 the modeling and the design of electrical-subsystem is carried out and the control strategy for DSACPC is presented; Chapter 4 shows the numerical and experimental results to validate the performance of full proposed system.

Chapter 1

CONCENTRATING SOLAR PLANT FOR COMBINED GENERATION OF HEAT AND POWER

1.1 Introduction

Systems called to generate heat and electricity power are the Concentrating Solar Power (CSP), which use mirrors to concentrate and focus the solar radiation, so that a receiver could yield this energy to a thermal fluid in order to increase its temperature.

Nowadays, the research in the field of CSP brought to the born of a great variety of mirror shapes and solar tracking methods, being a trade-off between a good energy storage for the peak loads and the base loads and a significant low CO₂ emissions. Despite in Europe the installed CSP power grew up very quickly in the last years, this kind of energy production is steel marginal in the framework of the energy supply, because the energy generation costs are higher than the competing technologies.

Moreover, the low efficiency of this kind of power plants also limits the diffusion of this technology; the weak point of the chain efficiency is the steam cycle because of the limited operating temperature range of the heat transfer fluid (400°C for synthetic oils and 600°C for molten salts), that makes the turbine inlet steam to range between 370°C and 550°C respectively [1].

CSP plants are typically diffused in large scale (between 50 MW and 280 MW) instead of the photovoltaic plants which are also spread in small scale because of the high costs and the efficiency which are optimized only for large scale installations. For this reason, in this Ph.D. thesis a new electrical sub-system for Concentrating Solar plant for Combined generation of Heat and Power (CS-

CHP) is designed and tested in order to increase the efficiency of the whole proposed system also for small scale installation like over house roofs and factory sheds. Moreover the synthetic oil option is chosen for CSP plant, coupled to Organic Rankine Cycle (ORC) for thermodynamic subsystem in order to avoid a so much high plant complexity so as for the molten salt option, and achieve the best efficiency as currently possible also for the small scale plant. Many efforts were devoted to the study of several CS-CHP plant configurations [2]-[3]-[4]-[5], where a mixture of hydrocarbons gases was used, showing that the regenerative cycles have:

- negative effects on the collector efficiency because of the arise of the average operating temperature of the first-stage collectors;
- positive effects on the ORC efficiency;
- a limiting negative effect on the electrical subsystem's efficiency, which does not overcome about 38%.

The proposed Concentrating Solar plant for Combined generation of Heat and Power (CS-CHP) consists of three subsystems:

- CSP (Concentrated solar power) subsystem;
- Thermodynamic subsystem;
- Electrical subsystem.

The following Fig. 1.1. shows the mentioned subsystems.

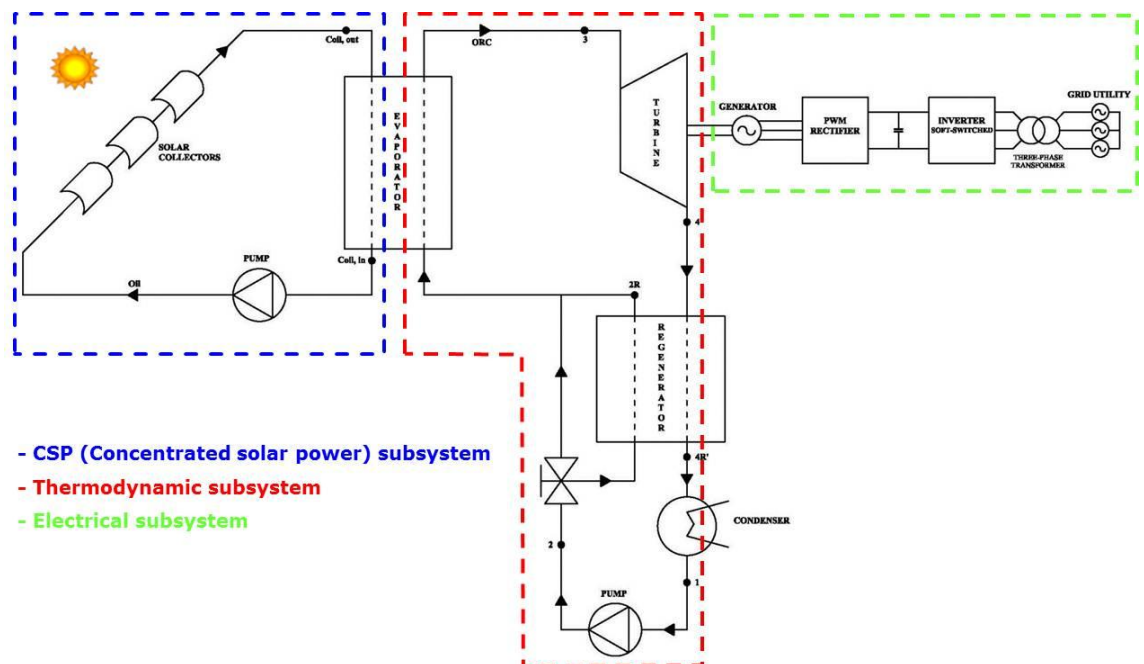


Fig. 1.1. Concentrating Solar plant for Combined generation of Heat and Power (CS-CHP).

In the following, the main CSP's and Thermodynamic subsystem's components will be described; as regard the electrical subsystem, only a short summary of it is given in this chapter because it will be thoroughly depicted in Chapter 3.

1.2 CSP subsystem

The solar collector consist of two main parts: parabolic linear mirrors, that are straight in one direction and parabolically curved in the others, and receiver tube.

The solar radiation is focused by the parabolic mirrors on the receiver tube placed along the focal line. The proposed tube has a xenon filled interspace to prevent vacuum leakages in contrast to it happens in the commercial tubes.

Solar collector's main parameter is the concentration factor:

$$C = \frac{A}{A_r} \quad (1.1)$$

where A is the parabolic mirror surface extension and A_r is the collector tube area.

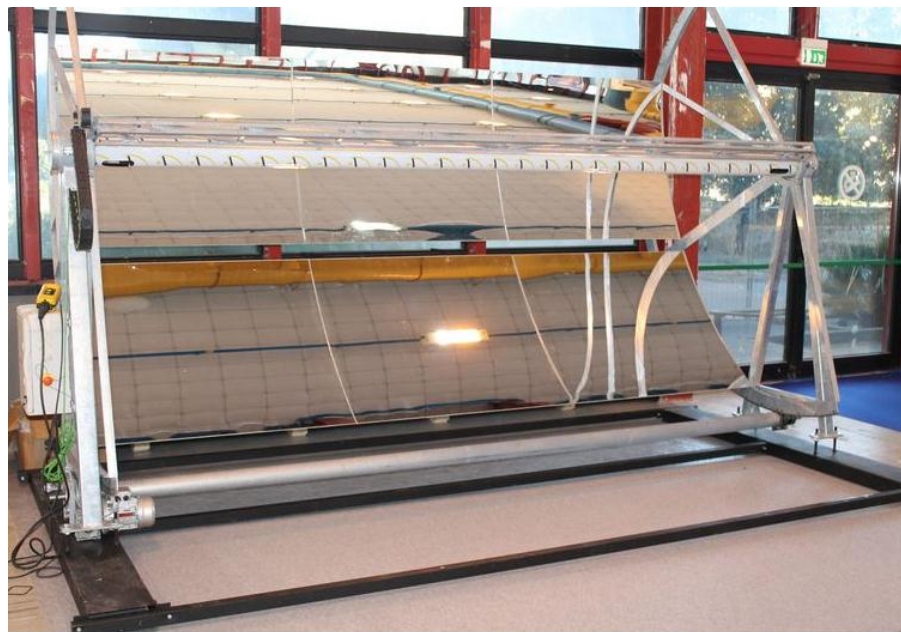


Fig. 1.2. Solar collector with aluminum parabolic structure covered by adhesive polymeric multilayer film with high reflectance

Fig. 1.2. shows the concentration parabolic mirror prototype realized at Department of Mechanical Engineering (DIME) of university of Naples Federico II; it consists of the following two main parts:

- parabolic mirror;
- receiver tube.

Because of the realization issues of the CSP integration with the structure of the building, a prototype was realized instead of using commercial parabolic mirror. For this reason a parabolic mirror in composite materials with steel supporting structure was designed. Moreover a new kind of receiver tube was set up so to increase the efficiency of the whole capture subsystem. Hereafter the mean features of CSP subsystem's components will be depicted.

1.2.1. Parabolic Mirror

The use of glass as reflective material for the parabolic mirrors was not possible due to the high curvature imposed to mirror by the installation constraints on the building structure; in fact, using the estimated values of the parabola opening (2200 mm) and focal distance (1100 mm) the glass may be damaged. Therefore, aluminum parabolic structures coated by adhesive polymeric multilayer films with high reflectance were used.

Fig. 1.3. shows the physical structure of the used reflecting polymeric multilayer film:



Fig. 1.3. Structure of the polymeric multilayer films with silver layer deposited under vacuum.

Such polymeric multilayer film shows good performance in terms of reflectance coefficient for solar radiation whose spectral frequency belongs to the visible, UV and NIR bandwidth.

Because of corrosion issues for silver layer and its property to transmit the UV radiation with wavelength about 320 nm, the presence of corrosion inhibitors and UV radiation absorbers was foreseen on the adhesives used to join the many layers of the film and on the protective coatings (layers 6-7); in this way the UV radiation of the silver is not allowed to decay the BOPET (Bi-Oriented PET) sub-layer (layers 3-4), where the silver was placed over.

The width of multilayer flexible film is some hundreds of micrometers.

The very reflective layer consists of two BOPET layers and silver layer.

The first BOPET layer (layer 4), touching the silver layer, is free of slipping agents in order to enhance the silver reflectance; on the contrary the lower BOPET sub-layer (layer 3) has slipping agents so to improve the joining of the structure. The silver layer is covered with an acrylic coating layer with corrosion inhibitors whose depth is few micrometers (layer 6).

An additional coating layer with UV absorbers is placed over the latter to absorbs the radiations with wavelength $300nm \leq \lambda \leq 400nm$. Under the BOPET layers there is a pressure sensing adhesive layer (layer 2) to fix the reflective structure to that of concentration parabola. An additional acrylic protective film (layer 8-9) can be added to previous structure in order to prevent the rain and others atmospheric agents to damage the whole structure.

The realization of the prototype was carried out by using the SILVERLUX structure (layer 1-7) and a protective layer as KORAD KLEAR 050005.

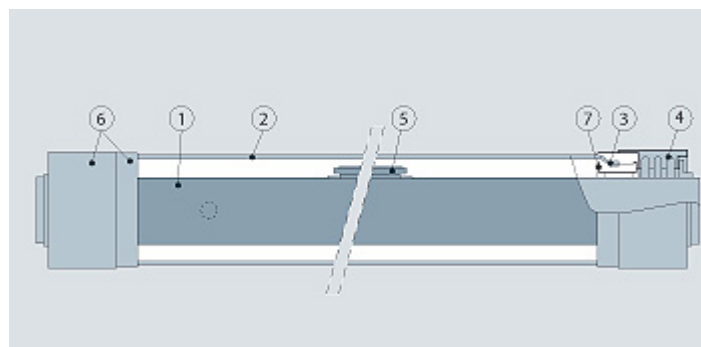
1.2.2. Receiver Tube

The commercial receiver tubes are complex and expensive; moreover the keeping of the vacuum in the interspace is not guarantee. For this reason a new receiver tube has been designed in order to achieve lower costs and constructive simplicity.

Fig. 1.4. shows the schema of proposed receiver tube.



(a)



(b)

Fig. 1.4. The receiver tube: (a) external visualization - (b) structure of the receiver tube.
where:

- (1) internal stainless steel receiver tube;
- (2) external cylindrical glass tube;
- (3) glass-metal junction;
- (4) bellows;
- (5) getter;
- (6) external shields;
- (7) internal shields.

The tube structure is composed by:

- an internal stainless steel tube where the thermal fluid flows;
- an external cylindrical glass tube as screen with respect to radiations generated by internal tube except in correspondence of a fissure

enclosed by a lens that is placed longitudinally along the optical path length of the solar radiation reflected by the mirror and it is transparent with respect to the latter;

- an interspace between the external and the internal tubes containing a thermally insulating gas (Xenon) that has a pressure range about $1 \div 31$ mbar and a low thermal conductivity ($< 0,01$ W/mK);
- three irradiative screens are placed between the external surface of the internal tube and the external cylindrical tube with a low emissivity ($< 7\%$); these screens are composed by aluminum with silver coating.
- additional reflective screens can be add on the sides of a fissure enclosed by a lens in order to reflect the peripheral parts of the radiation flux reflected by the mirror on the internal receiver tube.

A coating is applied on the internal side of the external lens that is with respect to radiations with wavelength $320nm \leq \lambda \leq 2000nm$ (almost the entire solar spectrum) and at the same time reflective with respect to radiations with wavelength $\lambda > 2000nm$ (NIR). An additional coating was applied on the external side of the internal receiver tube in order to guarantee a high absorption coefficient with respect to radiations with wavelength $320nm \leq \lambda \leq 2000nm$ and at the same time a low infrared radiations emissivity of the internal tube.

The coupling joints have been placed at the end of the internal tube so the external cylindrical tube can rotate axially around the internal tube together the parabolic mirror during the sunlight tracking.

The thermal efficiency of the whole receiver tube is greater than the others commercial tubes because Xenon gas prevents the heat loss of the internal receiver tube; moreover the additional irradiative and reflective screens capture the almost the entire solar radiation.

The Table 1.1 lists the main features of the adopted receiver tube with operating temperature about $250 \div 550$ °C.

TABLE 1.1 - MAIN CHARACTERISTICS OF RECEIVER TUBE

PROPERTY	DATA
external glass tube diameter [mm]	115
glass thickness [mm]	3.0
internal steel tube diameter [mm]	70
steel thickness [mm]	3.0
receiver tube length [mm]	4060
active length [mm]	3865
vacuum level	< 1 Pa
absorbance solar coating	> 0.9
remittance coating	< 0.15
maximum differential dilatation [mm]	40
maximum temperature of the receiver tube [°C]	550
maximum temperature of the glass tube [°C]	100
maximum pressure [Mpa]	1,2

1.3 Thermodynamic subsystem

The proposed combined heat and power consists of a Concentrating Solar Plant (CSP) coupled to ORC. The parabolic mirrors focus the sun rays to receiver tube; in this way the thermal fluid archived high temperature (400°C) and by means of ORC generates mechanical energy. In the following will be analyzed the main components of proposed thermodynamic sub-system.

The thermodynamic plant consists of two main circuits, as shown in the Fig. 1.5.: in the primary circuit the primary fluid takes thermal energy from the solar collector and yields it to the secondary fluid trough to the evaporator; in the secondary circuit an organic fluid flows into a Rankine Cycle (ORC).

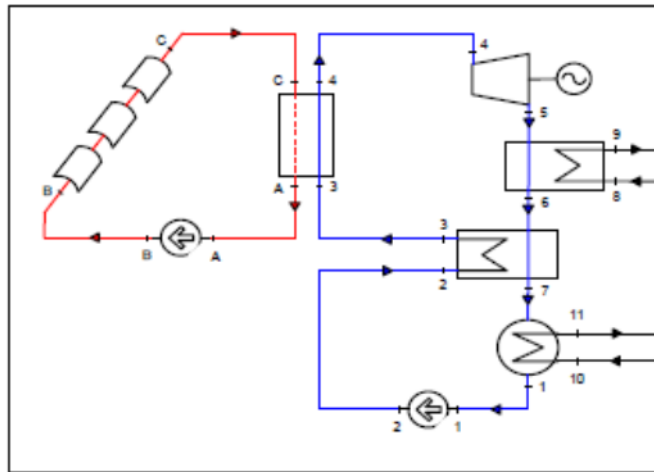


Fig. 1.5. Scheme of thermodynamic sub-system reporting primary (red) and secondary (blue) circuits.

The chosen primary fluid is Dowtherm A, a mixture of two substances: biphenyl (C_6H_{12}) and diphenyl oxide ($C_{12}H_{10}O$).

Since both the substances have the same vapor pressure, the Dowtherm A is thermodynamically equivalent to a unique component.

The main advantages of the Dowtherm A with respect to other thermal fluids are the chemical and physic stability and the wide availability, that makes it not expensive.

Table 1.2 shows Dowtherm A main characteristics.

TABLE 1.2 - MAIN PROPERTIES OF DOWTHERM A

Physical Properties of DOWTHERM A Fluid			
Property	SI Units	Property	SI Units
Atmospheric Boiling Point	257.1°C	Dissipation Factor at 75°F (24°C)	
Freezing Point	12.0°C	frequency 10 ³	0.0012
Flash Point, SETA	113°C	frequency 10 ⁴	0.0001
Fire Point, C.O.C. [†]	118°C	frequency 10 ⁵	0.0001
Auto Ignition Temp. ^{††}	599°C	Dielectric Strength at 75°F (24°C)	20,866 volts/nm
Density at 75°F	1056 kg/m ³ @ 25°C	Surface Tension in Air	40.1 Dynes/cm @ 20°C
Heat of Fusion	98.2 kJ/kg		37.6 Dynes/cm @ 40°C
Specific Resistivity	1.2 x 10 ¹² ohm cm @ 0°C		35.7 Dynes/cm @ 60°C
	6.4 x 10 ¹¹ ohm cm @ 20°C	Critical Temperature	497°C
	3.9 x 10 ¹¹ ohm cm @ 40°C	Critical Pressure	31.34 bar
Dielectric Constant at 75°F (24°C)		Critical Volume	3.17 l/kg
frequency 10 ³	3.26	Heat of Combustion	36,053 kJ/kg
frequency 10 ⁴	3.27	Molecular Weight (Avg.)	
frequency 10 ⁵	3.27		

The maximum operating temperature of the Dowtherm A in the proposed primary circuit is about 400 °C, as reported in the following operating conditions:

- Oil rate: 0,51 kg/s;
- Tube inlet temperature: 370 °C;
- Tube outlet temperature: 400 °C.

As we know, in the Rankine Cycles it is not possible to yield heat to the vapor if the operative temperatures are lower than 550 °C, to prevent the turbine's blades erosion. Therefore an organic fluid was chosen that allows expansion in superheated condition overcrossing condensation problems, because of the low operating temperature; this fluid is called dry fluid.

For secondary circuit about 60 fluids were analyzed and for each of them were considered the same thermodynamic transformations:

- Compression (1-2);
- Pre-heating by turbine outlet fluid (2-3);
- Main heating by primary fluid (3-4);
- Expansion (4-5) turbine outlet;
- Primary cooling at turbine outlet (5-6);
- Condensation in regenerative heat exchanger (6-1).

having the maximum operating temperature of 370 °C.

The chosen dry fluid is the Decane; the choice was made in such a way to optimize the global efficiency η_g of proposed thermodynamic sub-system, defined as:

$$\eta_g = \frac{P_u}{P_s} \quad (1.2)$$

where P_g is the power at turbine outlet fixed at 10 kW and P_s is the solar power collected by parabolic mirrors.

The optimization was carried on by changing the turbine inlet upper pressure for each tested fluid; using the Decane fluid, the global efficiency is 18,3 % with the following operating conditions:

- Upper pressure: 18 bar;
- Lower pressure: 0,5 bar.

The high efficiency achieved using the Decane allows to minimize the parabolic mirrors surface extension about to 60 m^2 with a minimum length of the 15 m for the receiver tube.

1.4 Electrical subsystem

In the case of distributed power generation by renewable source (wind, thermal solar plant and tidal stream generator), the energy supplied by the renewable source is generally converted in electrical energy by means of an electrical subsystem that consists of an electrical machine coupled with a power electronic interface connected to the grid-utility. Moreover a suitable control strategy for the electrical subsystem must be implemented in order to maximize the efficiency of the energy flow conversion. Many control strategies have been proposed in literature to achieve high performance of the whole controlled system [6]-[18]; however the Sliding Mode Control (SMC) has been particularly adopted thanks to its easy configuration and set-up and its advantages about stability and robustness against parameters and load uncertainties with respect to other types of non-linear control strategy for Variable Structure System (VSS) [6]-[18]. Unfortunately, the high performance and robustness of the sliding mode control are achieved only after the occurrence of the sliding mode on a suitable sliding manifold; furthermore the sliding mode may be characterized by chattering phenomena due to unmodeled dynamic of the controlled system and presence of external disturbances. For this reasons the sliding mode control theory is fully treated in Chapter 2 of this Ph.D. thesis, where at first the classic sliding mode control theory and continuous-time formulation of the sliding mode control are explained and after the integral sliding mode control and discrete-time formulation of sliding mode control is treated until the higher-order sliding mode control theory, while a particular attention is reserved for the most used technique to avoid the chattering phenomenon and for sliding mode observer design.

The electrical subsystem of proposed CS-CHP plant is composed by a Permanent Magnet Synchronous Generator (PMSG) coupled with a Double-Stage AC-AC Power Converter (DSACPC) as shown in Fig. 1.6.

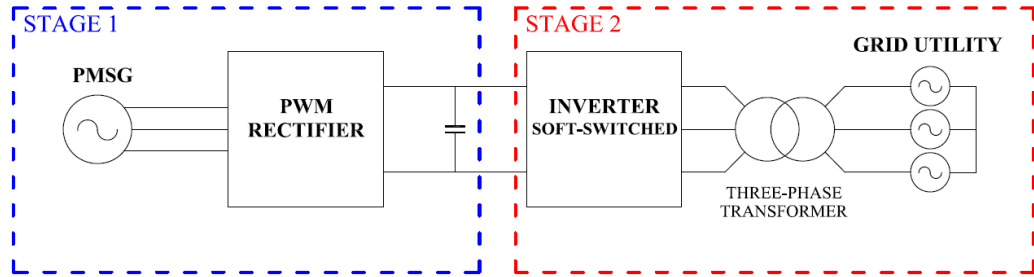


Fig. 1.6. Scheme of proposed electrical subsystem.

The DSACPC consists of two stages: the Stage 1 is composed by the PMSG coupled with a three-phase PWM rectifier and a DC-link capacitor bank, while the Stage 2 is composed by a three-phase soft-switched Voltage Source Inverter connected to the grid-utility by means of a three-phase step-up transformer. The adopted control strategy is focused on the second-order Super-Twisting integral sliding mode control that is able to overcome the cited problems, guaranteeing the robustness of the system against system parameters variation and external disturbances during the whole controlled system response and avoiding the chattering phenomena. Thanks to the proposed control strategy, the first converter stage is able to track the maximum power point drawn from the thermodynamic subsystem and to keep also the DC-link voltage to a desired value; the second converter stage instead giving the desired active power to the grid can be used also a reactive power compensator under balanced conditions of the grid-utility or as a system of current harmonic rejection in the case of unbalanced conditions of the grid-utility.

The modeling and the design of the main components of the proposed electrical subsystem are fully developed in Chapter 3 and the control strategy of both stages of DSACPC is completely described in the same chapter.

Chapter 2

SLIDING MODE CONTROL

The Variable Structure Control (VSC) is a general approach for designing of robust control system and it is composed by a series of continuous subsystems with a suitable logic switching. This type of control has taken on a growing importance over the years since they are suitable for controlling of a wide range of type systems as linear and nonlinear, time-invariant and time-variant systems, single input single output systems (SISO) or multi-input multi-output systems (MIMO), continuous or discrete time systems.

Nowadays the Sliding Mode Control (SMC) has increased its spread thanks to the emergence of new classes of problems and the progress in switching components. The SMC is a control technique very renowned due to its robustness property with respect to the parameters variation of the system and the external disturbances.

However this control technique has drawbacks intrinsic in the discrete and discontinuous nature of VSC as undesired chattering and high-frequency vibrations, that are dangerous for the system.

2.1 Classic Sliding Mode Control

The main feature of the adoption of the sliding mode control for designing of the controller of a VSC consists of forcing the trajectory of the state variables vector to lie on a sliding manifold belonging to the state space.

The sliding surface is coincident with intersection of hyperplanes belonging to the state space. Once the state trajectory vector reaches the sliding surface, the feedback control action adapt automatically in order to obtain the sliding motion on this sliding surface.

Let us an arbitrary system with a vector control defined as follows:

$$\begin{aligned} \dot{\mathbf{x}} &= \mathbf{f}(\mathbf{x}, \mathbf{u}) \quad \mathbf{x}, \mathbf{f} \in \mathfrak{R}^n, \mathbf{u}(\mathbf{x}) \in \mathfrak{R}^m \\ u_i(\mathbf{x}) &= \begin{cases} u_i^+(\mathbf{x}) & \text{for } s_i(\mathbf{x}) > 0 \\ u_i^-(\mathbf{x}) & \text{for } s_i(\mathbf{x}) < 0 \end{cases} \quad i = 1, 2, \dots, m \end{aligned} \quad (2.1)$$

where the components $s_i(\mathbf{x})$ of vector $\mathbf{s}(\mathbf{x})$ are m smooth function and i -th component $u_i(\mathbf{x})$ of vector control $\mathbf{u}(\mathbf{x})$ is discontinuous function on the i -th surface $s_i(\mathbf{x}) = 0$.

The equivalent control method can be used in order to obtain a sliding mode on the sliding manifold $\mathbf{s}(\mathbf{x}) = \mathbf{0}$ [19].

This method consists of the replacement of discontinuous control \mathbf{u} in a neighborhood of sliding manifold by a continuous control called *equivalent control* \mathbf{u}_{eq} such that the solution of system (2.1) exists in conventional sense with the introduction of this new input control vector.

Assuming that the initial state vector of system (2.1) is on the sliding manifold, which is an intersection of the m discontinuous surfaces, after occurring a sliding mode the state trajectories will be confined to the sliding manifold $\mathbf{s}(\mathbf{x}) = \mathbf{0}$ for all time instants such that $t > t_0$; therefore also the time derivative of the sliding function is equal to zero $\dot{\mathbf{s}}(\mathbf{x}) = \mathbf{0}$ for $t > t_0$.

Hence the time derivative of sliding function $\dot{\mathbf{s}}(\mathbf{x}) = \mathbf{0}$ can be used in addition to constraint $\mathbf{s}(\mathbf{x}) = \mathbf{0}$ in order to characterize the state trajectories during the sliding mode.

The discontinuous control \mathbf{u} will be replaced by equivalent control \mathbf{u}_{eq} that is calculated by equating to zero the time derivative of the sliding function:

$$\dot{\mathbf{s}}(\mathbf{x}) = \frac{\partial \mathbf{s}}{\partial \mathbf{x}} \mathbf{f}(\mathbf{x}, \mathbf{u}) = \mathbf{0} \quad (2.2)$$

where $\frac{\partial \mathbf{s}}{\partial \mathbf{x}}$ is $m \times n$ matrix with gradients of functions $s_i(\mathbf{x})$ as rows.

If a solution to algebraic equation (2.2) exists, this is called *equivalent control* \mathbf{u}_{eq} and it is a continuous function that is solution of the following system:

$$\begin{cases} \dot{\mathbf{s}}(\mathbf{x}) = \frac{\partial \mathbf{s}}{\partial \mathbf{x}} \mathbf{f}(\mathbf{x}, \mathbf{u}) = \mathbf{0} \\ \mathbf{u} = \mathbf{u}_{eq} \end{cases} \quad (2.3)$$

Replacing \mathbf{u}_{eq} to \mathbf{u} into system (2.1), the following equation is obtained:

$$\dot{\mathbf{x}} = \mathbf{f}(\mathbf{x}, \mathbf{u}_{eq}) \quad (2.4)$$

which together with the initial conditions $\mathbf{s}(\mathbf{x}(t_0)) = \mathbf{0}$ describes the state motion along the sliding manifold $\mathbf{s}(\mathbf{x}) = \mathbf{0}$. For this reason (2.4) is known as *motion equation of the sliding mode*.

The procedure that has been described for obtaining the motion equation of the sliding mode is the core of the equivalent control method [19].

From a geometrical view point, the equivalent control method consists by the replacement of discontinuous control vector \mathbf{u} by a continuous control vector \mathbf{u}_{eq} such that the velocity state vector (time derivative of the state vector) lies in tangential manifold to the sliding surface at least in a neighborhood in the vicinity of the switching surface, as shown in the next figure:

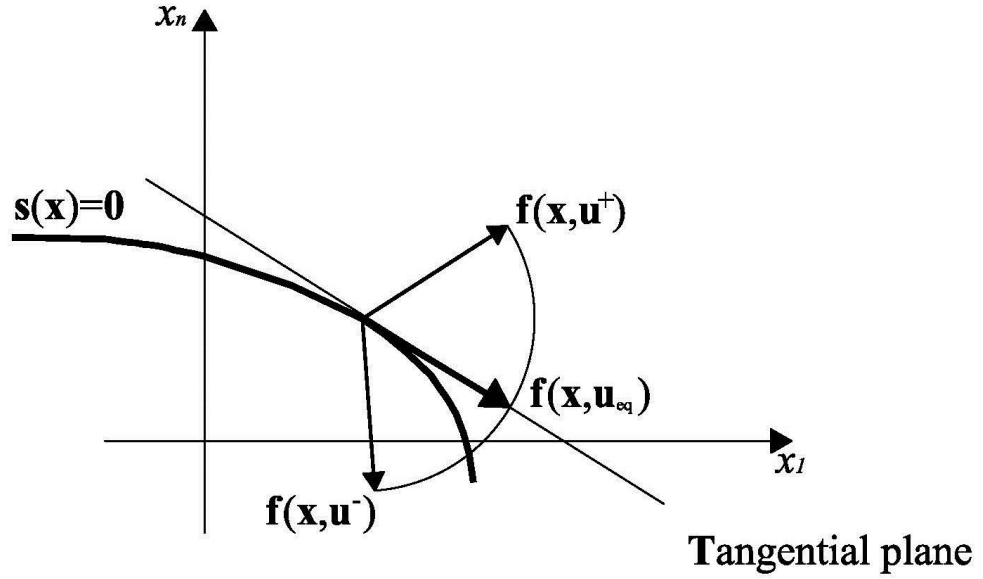


Fig. 2.1. State velocity vector in sliding mode for nonlinear system with equivalent control method

When the state trajectories are confined exactly to the sliding manifold $\mathbf{s}(\mathbf{x}) = \mathbf{0}$, the *ideal sliding mode* occurs for system (2.1). The term “ideal” for the sliding mode is used in this case because an ideal sliding mode is achieved only if the discontinuous control vector switches with a very high frequency or theoretically infinite on the sliding manifold so that the velocity state vector is precisely oriented along the intersection of the discontinuous surfaces (this is required for each component of the control vector).

However, in practical applications the state trajectories run in a boundary layer of width $\Delta > 0$ in a neighborhood in the vicinity of sliding manifold $\mathbf{s}(\mathbf{x}) = \mathbf{0}$ due to the finite switching frequency of input control and unmodeled dynamics such as delay and hysteresis phenomenon, as shown in Fig. 2.2. Under this condition the state vector satisfies the following equation:

$$\|\mathbf{s}(\mathbf{x})\| \leq \Delta \quad \text{with} \quad \|\mathbf{s}\| = (\mathbf{s}^T \mathbf{s})^{1/2} \quad (2.5)$$

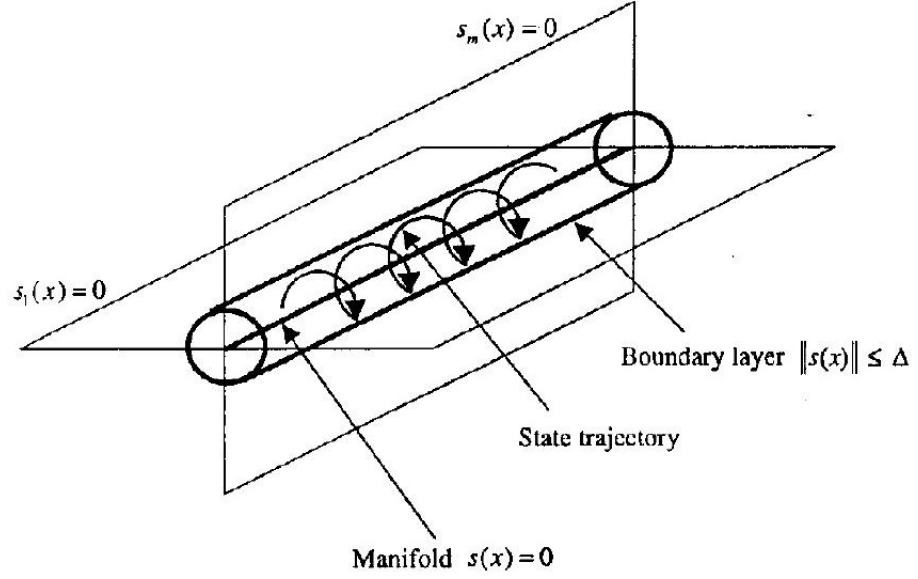


Fig. 2.2. Boundary layer of sliding mode equation

This aspect will be examined in Section 2.2 of this thesis.

2.1.1 Existence Conditions of Sliding Mode

The occurrence of the sliding mode on a switching manifold needs that the existence conditions of sliding mode to be verified in the state space.

In practical applications the most common systems are linear with respect to both the state vector and the control input:

$$\dot{\mathbf{x}}(t) = \hat{\mathbf{f}}(t, \mathbf{x}, \mathbf{u}) = \mathbf{f}(t, \mathbf{x}) + \mathbf{B}(t, \mathbf{x})\mathbf{u}(t) \quad (2.6)$$

where $\mathbf{x}(t) \in \mathfrak{R}^n$ is the state vector, $\mathbf{u}(t) \in \mathfrak{R}^m$ is the control vector and let that each component of $\mathbf{f}(t, \mathbf{x}) \in \mathfrak{R}^n$ and $\mathbf{B}(t, \mathbf{x}) \in \mathfrak{R}^{n \times m}$ to be continuous functions with bounded derivative with respect to \mathbf{x} .

Each component $u_i(t, \mathbf{x})$ of the control vector is a discontinuous function with respect to i -th component of the switching manifold:

$$u_i(t, \mathbf{x}) = \begin{cases} u_i^+(t, \mathbf{x}) & \text{for } s_i(\mathbf{x}) > 0 \\ u_i^-(t, \mathbf{x}) & \text{for } s_i(\mathbf{x}) \leq 0 \end{cases} \quad i = 1, 2, \dots, m \quad (2.7)$$

where $s_i(\mathbf{x})$ is i -th component of the $(n-m)$ dimensional switching surface $\mathbf{s}(\mathbf{x}) = [s_1(\mathbf{x}), s_2(\mathbf{x}), \dots, s_m(\mathbf{x})]^T = \mathbf{0}$. In particular any surface $s_i(\mathbf{x}) = 0$ is a set of points of discontinuity for the respective component $u_i(t, \mathbf{x})$ of the control vector.

The equivalent control method may be used to determine the system motion restricted to the switching surface $\mathbf{s}(\mathbf{x}) = \mathbf{0}$.

To provide this suppose that the state trajectory reaches the switching surface $\mathbf{s}(\mathbf{x}) = \mathbf{0}$ at the time instant t_0 and it remains on the switching surface for all subsequent time instants $t \geq t_0$. In other words a sliding mode exists on the switching surface $\mathbf{s}(\mathbf{x}) = \mathbf{0}$ for $t \geq t_0$.

Since the existence of a sliding mode on the surface $\mathbf{s}(\mathbf{x}) = \mathbf{0}$ implies $\mathbf{s}(\mathbf{x}(t_0)) = \mathbf{0}$ and $\dot{\mathbf{s}}(\mathbf{x}(t)) = \mathbf{0} \forall t \geq t_0$, the application of the equivalent control method yields:

$$\dot{\mathbf{s}} = \frac{\partial \mathbf{s}}{\partial \mathbf{x}} \dot{\mathbf{x}} = \frac{\partial \mathbf{s}}{\partial \mathbf{x}} [\mathbf{f}(t, \mathbf{x}) + \mathbf{B}(t, \mathbf{x}) \mathbf{u}_{eq}] = \mathbf{0} \quad (2.8)$$

The expression of equivalent control \mathbf{u}_{eq} can be derived by (2.8) assuming that the product matrix $\left[\frac{\partial \mathbf{s}}{\partial \mathbf{x}} \right] \mathbf{B}(t, \mathbf{x})$ is nonsingular for each components of the state vector and for all $t \geq t_0$:

$$\mathbf{u}_{eq} = - \left[\left[\frac{\partial \mathbf{s}}{\partial \mathbf{x}} \right] \mathbf{B}(t, \mathbf{x}) \right]^{-1} \frac{\partial \mathbf{s}}{\partial \mathbf{x}} \mathbf{f}(t, \mathbf{x}) \quad (2.9)$$

Then, with constraint $\mathbf{s}(\mathbf{x}(t_0)) = \mathbf{0}$ and by substituting (2.9) into (2.6), the dynamics of system (2.6) on the switching surface $\mathbf{s}(\mathbf{x}) = \mathbf{0}$ for all $t \geq t_0$ will be governed by the following sliding mode equation:

$$\dot{\mathbf{x}} = \mathbf{f}(t, \mathbf{x}) - \mathbf{B}(t, \mathbf{x}) \left[\left[\frac{\partial \mathbf{s}}{\partial \mathbf{x}} \right] \mathbf{B}(t, \mathbf{x}) \right]^{-1} \frac{\partial \mathbf{s}}{\partial \mathbf{x}} \mathbf{f}(t, \mathbf{x}) \quad (2.10)$$

The stability of the state trajectory on the sliding surface $\mathbf{s}(\mathbf{x}) = \mathbf{0}$ at least in a neighborhood of sliding manifold $\{\mathbf{x} | \mathbf{s}(\mathbf{x}) = \mathbf{0}\}$ is required in order to derive

the existence conditions of sliding mode. In other word at least asymptotically convergence of the state vector is required in a neighborhood of sliding surface.

The largest such neighborhood is called the *region of attraction* of state trajectories. From a geometrical viewpoint this means that the velocity state vector must point toward the sliding surface in the region of attraction.

The stability of the projection of state motion of the system (2.6) on the switching manifold $\mathbf{s}(\mathbf{x}) = \mathbf{0}$ can be analyzed by means of the following equation:

$$\dot{\mathbf{s}} = \left[\frac{\partial \mathbf{s}}{\partial \mathbf{x}} \right] \left[\mathbf{f}(t, \mathbf{x}) + \mathbf{B}(t, \mathbf{x}) \mathbf{u}(t) \right] \quad (2.11)$$

where the discontinuous control vector is defined as:

$$\mathbf{u}(t, \mathbf{x}) = \begin{cases} \mathbf{u}^+(t, \mathbf{x}) & \text{for } \mathbf{s}(\mathbf{x}) > \mathbf{0} \\ \mathbf{u}^-(t, \mathbf{x}) & \text{for } \mathbf{s}(\mathbf{x}) \leq \mathbf{0} \end{cases} \quad \text{componentwise} \quad (2.12)$$

The control vector can be expressed as:

$$\mathbf{u}(t, \mathbf{x}) = \mathbf{u}_0(t, \mathbf{x}) + \mathbf{U}(t, \mathbf{x}) \text{sign}(\mathbf{s}(\mathbf{x})) \quad (2.13)$$

where $\mathbf{u}_0(t, \mathbf{x}) = \frac{1}{2}(\mathbf{u}^+(t, \mathbf{x}) + \mathbf{u}^-(t, \mathbf{x}))$, $\mathbf{U}(t, \mathbf{x})$ is a diagonal matrix with

elements $U_i(t, \mathbf{x}) = \frac{1}{2}(\mathbf{u}^+(t, \mathbf{x}) - \mathbf{u}^-(t, \mathbf{x}))$ for $i = 1, \dots, m$ and the each

component of discontinuous function $\text{sign}(\mathbf{s})$ is a sign function:

$$\text{sign}(\mathbf{s})^T = [\text{sign}(s_1), \dots, \text{sign}(s_m)] \quad (2.14)$$

Substituting (2.13) into (2.11) the motion projection on the switching surface is governed by the following equation:

$$\dot{\mathbf{s}} = \mathbf{g}(t, \mathbf{x}) - \mathbf{G}(t, \mathbf{x}) \text{sign}(\mathbf{s}) \quad \text{with} \quad \begin{cases} \mathbf{g}(t, \mathbf{x}) = \left[\frac{\partial \mathbf{s}}{\partial \mathbf{x}} \right] \left[\mathbf{f}(t, \mathbf{x}) + \mathbf{B}(t, \mathbf{x}) \mathbf{u}_0 \right] \\ \mathbf{G}(t, \mathbf{x}) = - \left[\frac{\partial \mathbf{s}}{\partial \mathbf{x}} \right] \left[\mathbf{B}(t, \mathbf{x}) \mathbf{U}(t, \mathbf{x}) \right] \end{cases} \quad (2.15)$$

As mentioned above the sliding mode existence problem involve a stability problem, which can be treated with Lyapunov's second method [20].

In particular the stability of the state trajectory on a sliding manifold requires the existence of a Lyapunov function $V(t, \mathbf{x})$ that is positive definite and it has a negative time derivative in the region of attraction.

The following definition is valid

Definition 2.1: A domain \mathbf{D} in the manifold $\mathbf{s}(\mathbf{x}) = \mathbf{0}$ is a sliding mode domain if for each real $\epsilon > 0$, there is a real $\delta > 0$ such that any motion starting within a n -dimensional δ -vicinity of \mathbf{D} may leave the n -dimensional ϵ -vicinity of \mathbf{D} only through the n -dimensional ϵ -vicinity of the boundary of \mathbf{D} , as shown in Fig. 2.3.

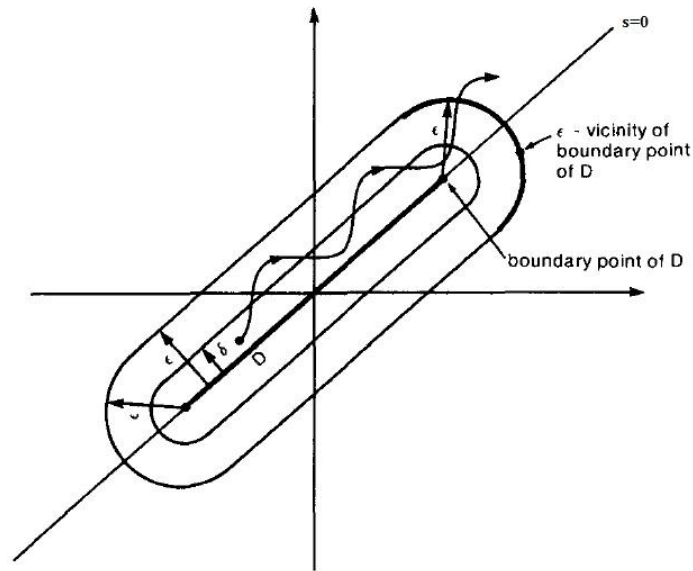


Fig. 2.3. Domain of sliding mode in 2D-dimension

Hence the domain \mathbf{D} lies on the surface $\mathbf{s}(\mathbf{x}) = \mathbf{0}$.

Equivalently it could be said that the domain \mathbf{D} is a sliding mode domain for the motion governed by (2.15) if the origin of the subspace \mathbf{s} is asymptotically stable with finite time convergence for each $\mathbf{x} \in \mathbf{D}$.

The manifold $\mathbf{s}(\mathbf{x}) = \mathbf{0}$ is called a sliding manifold if a sliding mode exists for all its points, so $\mathbf{D}(\mathbf{x}) = \{\mathbf{x} | \mathbf{s}(\mathbf{x}) = \mathbf{0}\}$.

The following theorem can be applied:

Theorem 1: For the $(n-m)$ dimensional domain \mathbf{D} to be the domain of a sliding mode, it is sufficient that in some n -dimensional domain

$\Omega \supset \mathbf{D}$, there exists a function $V(t, \mathbf{x}, \mathbf{s})$ continuously differentiable with respect to all of its arguments, satisfying the following conditions:

- 1) $V(t, \mathbf{x}, \mathbf{s})$ is positive definite with respect to \mathbf{s} ;
- 2) the total time derivative of $V(t, \mathbf{x}, \mathbf{s})$ for the system (2.6) has a negative supremum for all $\mathbf{x} \in \Omega$ except for \mathbf{x} on the switching surface where the control inputs are undefined, and hence the derivative of $V(t, \mathbf{x}, \mathbf{s})$ does not exist.

The sliding mode is globally reachable if the domain of attraction is a subspace of the state space (the sliding mode must exist starting from each point of domain).

Considering the next equation:

$$\dot{\mathbf{s}} = \mathbf{G}(t, \mathbf{x}) \text{sign}(\mathbf{s}) \quad (2.16)$$

if the matrix $\mathbf{G}(t, \mathbf{x})$ is positive definite such that it satisfies the condition:

$$\mathbf{G}(t, \mathbf{x}) + \mathbf{G}(t, \mathbf{x})^T > \mathbf{0} \quad (2.17)$$

as results the origin of subspace \mathbf{s} is a asymptotically stable equilibrium point with a finite time convergence.

A Lyapunov function candidate for (2.6) can be defined as:

$$V(t, \mathbf{x}, \mathbf{s}) = \frac{1}{2} \mathbf{s}^2(\mathbf{x}) \quad (2.18)$$

that is globally positive definite.

If the switched feedback gains are chosen such that the time derivative of $V(t, \mathbf{x}, \mathbf{s})$ is negative in the region of attraction:

$$\frac{1}{2} \frac{d\mathbf{s}^2}{dt} = \mathbf{s} \cdot \dot{\mathbf{s}} < 0 \quad (2.19)$$

then the state trajectories converge to the sliding manifold and are restricted to it for all $t > t_0$.

2.2 Chattering phenomenon

Unmodeled dynamics in the closed loop control are usually neglected in the sliding mode control design; this involves finite width and frequency oscillations of dynamic behavior of the system during the sliding mode.

This phenomenon is known as *chattering phenomenon* and may degrade the performance of the system.

The switching action, that is main element of sliding mode controller, it is not classified as chattering because it is intended and its frequency tends on infinity in the ideal case; the term “chattering” is valid only for the undesired system oscillations with finite frequency caused by unmodeled system imperfections as parameters variations of the system and matched noise.

Accordingly an ideal sliding mode does not exists in the practical applications also because it needs that the control input commutes at an infinite frequency.

The next figure shows the dynamic behavior of the state trajectories in the vicinity of the sliding surface in presence of chattering phenomenon:

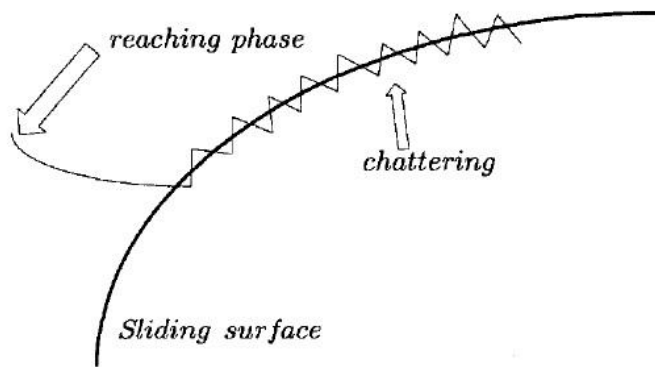


Fig. 2.4. The chattering phenomenon

The chattering phenomenon can excite unmodeled modes with high frequency that may lead the system to instability with high heat losses in power electronic components.

Many procedures have been proposed in literature for reduce or eliminate chattering [21].

In the following several methods will be discussed in order to avoid the chattering phenomenon.

2.2.1 Boundary layer technique

The simplest of technique for avoid chattering is the boundary layer technique that consists of replacing the signum function by a suitable saturation function in the control loop.

The saturation function is a continuous function that approximates the $sign(s)$ term in a boundary layer of sliding surface $s(t)=0$. An ordinary saturation function $sat(s)$ is depicted in the next figure:

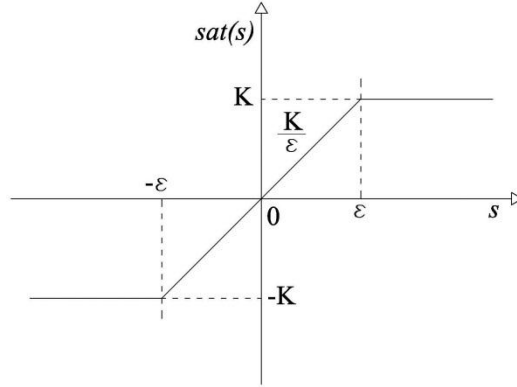


Fig. 2.5. Saturation function $sat(s)$

where $|s(x)| > \varepsilon \Rightarrow sat(s) = sign(s)$. Note that the saturation function $sat(s)$ is a continuous function in a small ε -vicinity of sliding surface with respect to the signum function $sign(s)$. Thus the control law becomes as follows:

$$u(t) = \begin{cases} K \cdot sign(s(t)) & \text{for } |s(t)| > \varepsilon \\ \frac{K}{\varepsilon} s(t) & \text{for } |s(t)| \leq \varepsilon \end{cases} \quad (2.20)$$

where K is a high gain.

For simplicity of treatment, consider the model of a first-order single-input single-output system:

$$\dot{x}(t) = ax(t) + bu(t) + d(x, t) \quad (2.21)$$

where $a^- \leq a \leq a^+$ and $0 < b^- \leq b \leq b^+$ are known parameters within known bounds, $d(x, t)$ is a bounded disturbance for all operating conditions $(x, t) \Rightarrow |d(x, t)| \leq d^+$. Let us know the desired state value x_{ref} and define the sliding function as:

$$s(t) = x_{ref}(t) - x(t) \quad (2.22)$$

A Lyapunov function candidate for the stability analysis of the considered system can be chosen as:

$$V = \frac{1}{2b} s^2(t) \quad (2.23)$$

The differentiation of (2.23) along the system trajectory (2.21) in the case of $|s(t)| > \varepsilon$ yields:

$$\dot{V}(t) = s(t)\dot{s}(t) = f(x_{ref}, x, t)s(t) - K|s(t)| \quad (2.24)$$

where the function:

$$f(x_{ref}, x, t) = \frac{\dot{x}_{ref} - ax(t) - d(x, t)}{b} \quad (2.25)$$

is upper bound under assumption that $x(t) \approx x_{ref}(t)$ as follows:

$$|f(x, x_{ref}, t)| \leq f^+ = \frac{\dot{x}_{ref}^+ + ax_{ref}^+ + d^+}{b^-} \quad (2.26)$$

A suitable choice of the saturation gain $K \geq f^+ + \frac{\varepsilon}{\sqrt{2b^-}}$ with scalar $\varepsilon > 0$ and the substitution of control law (2.20) into (2.24) lead to:

$$\dot{V}(t) \leq -\varepsilon V^{1/2} \quad \text{with } V = \frac{1}{2} \|s\|^2 \quad (2.27)$$

which guarantees a finite time convergence to sliding surface $s(x) = 0$.

Generally the substitution of entire control law (2.20) into (2.24) gives:

$$\dot{V}(t) \leq \begin{cases} -\varepsilon \cdot V^{1/2} & \text{for } |s(t)| > \varepsilon \\ \dot{s}(t) \left(f^+ - \frac{K}{\varepsilon} s(t) \right) & \text{for } |s(t)| \leq \varepsilon \end{cases} \quad (2.28)$$

which in terms of stability analysis proves the convergence of the state trajectory to the boundary layer of sliding surface.

Furthermore it can be noted that the system is continuous and linear in the boundary layer due to the introduction of the saturation function $sat(s)$; therefore the linear control theory can be used in order to analyze thoroughly the system stability. Although this technique reduces the chattering, it may compromise the robustness property the system after sliding mode occurring.

2.2.2 Observer-based technique

With the use the observer-based technique the chattering is avoided by introducing an auxiliary observer in the control loop. The state is estimated by means of an auxiliary observer and it is compared to its desired value; so a ideal sliding mode can be occurred on the observed sliding surface $\hat{s}(t)=0$ since the auxiliary observer loop is free from unmodeled dynamics. After the sliding mode occurred in the auxiliary observer loop, the state trajectory $x(t)$ follows the observed one $\hat{x}(t)$ according to observe error dynamics. The chattering is reduced despite the system has a discontinuous control input $u(t)$. A first-order observer for system (2.21) is defined as follows in order to study the auxiliary observer loop stability:

$$\dot{\hat{x}} = ax(t) + bu(t) + L\bar{x}(t) \quad (2.29)$$

where L is a linear gain of observer, $\bar{x}(t) = x(t) - \hat{x}(t)$ is the error of observation and let us that the system parameters a and b to be known.

The dynamic equation of observer loop is defined as:

$$\dot{\bar{x}} = d(x,t) - L\bar{x}(t) \quad (2.30)$$

If the disturbance is bounded $|d(x,t)| \leq d^+$ then the observation error is bounded too:

$$|\bar{x}(t)| \leq \frac{d^+}{L} \quad (2.31)$$

Defining the observer sliding surface as:

$$\hat{s}(t) = x_{ref}(t) - \hat{x}(t) \quad (2.32)$$

A Lyapunov's function candidate for stability of auxiliary observer loop can be chosen similar to case of boundary layer technique:

$$\hat{V}(t) = \frac{1}{2} \hat{s}^2(t) \quad (2.33)$$

The differentiation of (2.33) along the system trajectory (2.21) yields:

$$\begin{aligned} \dot{\hat{V}}(t) &= \frac{1}{2} \hat{s}(t) \dot{\hat{s}}(t) = \frac{1}{b} (\dot{x}_{ref}(t) - ax(t) - L\bar{x}(t)) \hat{s}(t) - K |\hat{s}(t)| \\ &\leq (\dot{x}_{ref}^+ + a^+ x_{ref}^+ + d^+) |\hat{s}(t)| - K |\hat{s}(t)| \end{aligned} \quad (2.34)$$

under the assumption that $x(t) \approx x_{ref}(t)$ and with the following control law:

$$u(t) = K \text{sign}(\hat{s}(t)) \quad (2.35)$$

The satisfaction of the condition $K \geq f^+ + \frac{\varepsilon}{\sqrt{2b^-}}$ leads to:

$$\dot{V}(t) \leq -\varepsilon V^{1/2} \quad \text{with } V = \frac{1}{2} \|s\|^2 \quad (2.36)$$

So an ideal sliding mode occurs on the observer sliding surface ($\hat{s}(t) = 0$ is exactly satisfied) with a finite time convergence to its. Thus the actual state $x(t)$ follows the observed one without exhibiting any chattering.

The observer-based technique guarantees more flexibility to control design with respect to other techniques to avoid chattering due to the presence of the auxiliary observer; in fact the auxiliary observer may be used to estimate the external disturbances in order to increase the tracking performance of the whole system.

2.2.3 Disturbance rejection technique

The disturbance rejection technique is able to avoid chattering by means of an accurate estimation of the disturbance that may be matched with original system.

This technique consists of dividing the control action in two terms:

$$u(t) = u_1(t) + u_2(t) \quad (2.37)$$

where the continuous component $u_1(t)$ is the proper control action used to control the behavior of the whole system and $u_2(t)$ is the discontinuous component used to reject disturbances and to remove parametric uncertainties.

Considering that the parameter b is known but the parameter a is entirely unknown for the system (2.21) with a unknown matched disturbance $d(x, t)$, the continuous component is designed such that the tracking error $x_e(t) = x_{ref}(t) - x(t)$ to be equal to zero as follows:

$$u_1(t) = \frac{M(x_e(t) + \dot{x}_{ref}(t))}{b} \quad (2.38)$$

where $M > 0$ is a proportional feedback gain.

The substitution of (2.38) into (2.21) according to the disturbance rejection term $u_2(t)$ set to zero in (2.37) ($u_2(t) = 0 \Rightarrow u(t) = u_1(t)$) yields:

$$\dot{x}(t) = ax(t) + bu_1(t) + d(x, t) \Rightarrow \dot{x}_e(t) + K \cdot x_e(t) = f(x, t) \quad (2.39)$$

where $f(x, t) = -ax(t) - d(x, t)$ is the disturbance function.

The stable error dynamic is governed by equation (2.39) and the tracking error $x_e(t)$ does not go to zero at regime due to disturbance presence $f(x, t) \neq 0$.

Therefore the discontinuous component $u_2(t)$ of control input is designed to

estimate the matched disturbance in order to decrease the influence of disturbance function $f(x,t)$ on the tracking performance of the state trajectory.

Defining a sliding surface as:

$$s(t) = x_e(t) + z(t) \quad (2.40)$$

where $z(t)$ is an auxiliary sliding variable such that $\dot{z}(t) = -\dot{x}_{ref}(t)$, the disturbance rejection term $u_2(t)$ can be calculated by using equivalent control method as follows:

$$\begin{aligned} \dot{s}(t) &= \dot{x}_e(t) + \dot{z}(t) = -ax(t) - bu_2(t) - d(x,t) \\ \Rightarrow u_2(t) &= \frac{1}{b}(-ax(t) - d(x,t)) \end{aligned} \quad (2.41)$$

the following dynamic equation of the tracking error can be obtained by replacing the entire control law (2.37) into (2.21):

$$\dot{x}_e(t) + K \cdot x_e(t) = 0 \quad (2.42)$$

where (2.38) and (2.41) were used to reduce the previous expression. the above equation (2.42) assures the asymptotically convergence of actual state $x(t)$ to desired one $x_{ref}(t)$ due to the rejection of disturbance $f(x,t)$ that contains also uncertainty of the system parameter a .

In conclusion the actual state $x(t)$ tracks the reference one $x_{ref}(t)$ exactly despite the presence of unknown system parameter variations and external disturbance matched also simultaneously.

2.3 Discrete-time Sliding Mode Control

A discussion about Discrete-Time Sliding Mode Control is necessary since many practical applications has represented by discrete-time mathematical models as those characterized by implementation of microprocessors or delay systems.

In the case of continuous-time sliding mode control a suitable discontinuous control input is required such that the state trajectory reaches the sliding surface and lies at least in a neighborhood of it for all subsequent time instant, according to that already discussed in the previous sections.

An ideal sliding mode occurs only with use of high switching frequency of control input and in this case the state trajectory lies exactly along the sliding surface. However, in practice the implementation of such high switching frequency of feedback control action is not possible because it involves high switching frequency of the power electronic components of the considered system. As results a limitation of operating voltage of the system is inevitable.

For this reason a discretization of sliding mode control is needs, for example by means of microprocessors. In fact if the same discontinuous control law of continuous-time systems would be used also for the discrete-time systems, a different chattering respect to the chattering phenomenon discussed in the previous sections may occur. This other kind of chattering is called “discretization chattering” and it is due to the fact that the switching frequency of the discrete-time systems is finite and upper limited by the sampling frequency of the system so the occurring of a sliding mode is not guaranteed. Moreover the state trajectory could not reach the sliding surface because the control input is calculated only in correspondence of each sampling time and remains constant during the sampling period.

Increasing the sampling frequency the amplitude of the discretization chattering decreases but its frequency increases; only in the case that the sampling period tends to zero $\Delta T \rightarrow 0$ the discretization chattering is avoided.

However the sampling frequency should be equal to the highest dynamic of the system in order to avoid an undesirable computational burden.

For these reasons for the control of discrete-time systems a discrete-time sliding mode control design is indispensable in contrast to the application of a continuous-time sliding mode control with a corresponding high switching frequency of control input.

2.3.1 Discrete-time sliding mode control design

To design a discrete-time sliding mode control the following continuous-time model of a linear time-invariant system is considered:

$$\dot{\mathbf{x}}(t) = \mathbf{A}\mathbf{x}(t) + \mathbf{B}\mathbf{u}(t) \quad (2.43)$$

where $\mathbf{x}(t) \in \mathbb{R}^n$ is the state vector, $\mathbf{u}(t) \in \mathbb{R}^m$ is the control input, \mathbf{A} and \mathbf{B} are known parameters matrices of the system.

The corresponding discrete-time representation of the model (2.44) with a sampling period ΔT is defined as:

$$\dot{\mathbf{x}}_{k+1} = \mathbf{A}_d \mathbf{x}_k + \mathbf{B}_d \mathbf{u}_k \quad (2.44)$$

where $\mathbf{A}_d = e^{\mathbf{A}\Delta T}$ and $\mathbf{B}_d = \int_0^{\Delta T} e^{\mathbf{A}(\Delta T-\tau)} \mathbf{B} d\tau$ are discrete-time parameters matrices of the system.

According to sliding mode control for continuous-time systems, the control law can be defined as discrete-time discontinuous function as follows:

$$\mathbf{u}_k = \begin{cases} \mathbf{u}_0 & \text{for } \mathbf{s}(\mathbf{x}_k) \geq \mathbf{0} \\ -\mathbf{u}_0 & \text{for } \mathbf{s}(\mathbf{x}_k) < \mathbf{0} \end{cases} \quad (2.45)$$

where $\mathbf{s}(\mathbf{x}_k) = \mathbf{0}$ is a sliding mode manifold. Since the control input \mathbf{u}_k can be switched only at each sampling point $k = t/\Delta T$ and it is constant during the

next sampling interval ΔT , the sliding manifold is reached at each sampling point but the state trajectory may not belong the sliding surface during the sampling period. Therefore, in the case of discrete-time systems the implementation of control law (2.43) produces discretization chatter in the motion trajectory once the sliding manifold is reached for the first time. For this reason the design of a suitable continuous control input is required in order to generate a discrete-time sliding mode control such that it is characterized by a chatter-free motion after reaching the sliding manifold.

The following definition is valid for any discrete-time systems [22]:

Definition 2.2: In the a discrete-time dynamic system:

$$\mathbf{x}_{k+1} = \mathbf{F}(\mathbf{x}_k, \mathbf{u}_k) \quad \mathbf{x} \in \mathbb{R}^n, \mathbf{u} \in \mathbb{R}^m, m \leq n \quad (2.46)$$

a discrete-time sliding mode takes place on the a subset Σ of the manifold $\sigma = \{\mathbf{x} : \mathbf{s}(\mathbf{x}) = \mathbf{0}\}$, $\mathbf{s} \in \mathbb{R}^m$, if there exists an open neighborhood Ω of this subset such that for each $\mathbf{x} \in \Omega$ it follows that $\mathbf{s}(\mathbf{F}(\mathbf{x}_{k+1})) \in \Sigma$.

The following choice of the sliding surface:

$$\mathbf{s}_k = \mathbf{C} \cdot \mathbf{x}_k \quad (2.47)$$

yields:

$$\mathbf{s}_{k+1} = \mathbf{C} \cdot \mathbf{x}_{k+1} = \mathbf{C} \cdot (\mathbf{A}_d \mathbf{x}_k + \mathbf{B}_d \mathbf{u}_k) \quad (2.48)$$

According to definition 2.2 a discrete-time sliding mode exists on manifold (2.47) if the matrix $(\mathbf{C}\mathbf{B}_d)$ is nonsingular and the control input can be calculated by equating (2.48) to zero:

$$\mathbf{s}_{k+1} = \mathbf{0} \Rightarrow \mathbf{u}_{k,eq} = -(\mathbf{C}\mathbf{B}_d)^{-1}(\mathbf{C}\mathbf{A}_d \mathbf{x}_k) \quad (2.49)$$

This control variable $\mathbf{u}_{k,eq}$ is called the *equivalent control* in analogy to continuous-time systems.

Let us represent the equivalent control as the sum of two linear functions:

$$\mathbf{u}_{k,eq} = -(\mathbf{CB}_d)^{-1} \mathbf{s}_k - (\mathbf{CB}_d)^{-1} (\mathbf{CA}_d - \mathbf{C}) \mathbf{x}_k \quad (2.50)$$

For the initial condition $\mathbf{s}_k \neq \mathbf{0}$, the equivalent control may exceed the available control resources when $\Delta T \rightarrow 0$ in order to reaching the sliding manifold. Therefore suppose that the control is bounded $\|\mathbf{u}_{k,eq}\| \leq \mathbf{u}_0$ and the available control resources are such that:

$$\|(\mathbf{CB}_d)^{-1}\| \cdot \|(\mathbf{CA}_d - \mathbf{C}) \mathbf{x}_k\| < \mathbf{u}_0 \quad (2.51)$$

Then the control input \mathbf{u}_k can be defined as follows:

$$\mathbf{u}_k = \begin{cases} \mathbf{u}_{k,eq} & \text{for } \|\mathbf{u}_{k,eq}\| \leq \mathbf{u}_0 \\ \mathbf{u}_0 \frac{\mathbf{u}_{k,eq}}{\|\mathbf{u}_{k,eq}\|} & \text{for } \|\mathbf{u}_{k,eq}\| > \mathbf{u}_0 \end{cases} \quad (2.52)$$

In the case that is $\|\mathbf{u}_{k,eq}\| \leq \mathbf{u}_0 \Rightarrow \mathbf{u}_k = \mathbf{u}_{k,eq}$ the state vector converges asymptotically to the sliding manifold as it is well known by equivalent control theory.

For $\|\mathbf{u}_{k,eq}\| > \mathbf{u}_0 \Rightarrow \mathbf{u}_k = \mathbf{u}_0 \frac{\mathbf{u}_{k,eq}}{\|\mathbf{u}_{k,eq}\|}$, the equation (2.48) can be reformulated as

follows:

$$\mathbf{s}_{k+1} = \mathbf{s}_k + (\mathbf{CA}_d - \mathbf{C}) \mathbf{x}_k + \mathbf{CB}_d \mathbf{u}_k \quad (2.53)$$

and the assumption $\mathbf{u}_k = \mathbf{u}_0 \frac{\mathbf{u}_{k,eq}}{\|\mathbf{u}_{k,eq}\|}$ leads to:

$$\mathbf{s}_{k+1} = \left(\mathbf{s}_k + (\mathbf{CA}_d - \mathbf{C}) \mathbf{x}_k \right) \cdot \left(1 - \frac{\mathbf{u}_0}{\|\mathbf{u}_{k,eq}\|} \right) \quad \text{with } \mathbf{u}_0 < \|\mathbf{u}_{k,eq}\| \quad (2.54)$$

Thus:

$$\|\mathbf{s}_{k+1}\| = \|\mathbf{s}_k + (\mathbf{CA}_d - \mathbf{C})\mathbf{x}_k\| \cdot \left(1 - \frac{\mathbf{u}_0}{\|\mathbf{u}_{k,eq}\|}\right) \quad (2.55)$$

The substitution of the absolute value of (2.50) into (2.55) yields:

$$\begin{aligned} \|\mathbf{u}_{k,eq}\| &= \|(\mathbf{CB}_d)^{-1}[\mathbf{s}_k - (\mathbf{CA}_d - \mathbf{C})\mathbf{x}_k]\| \Rightarrow \\ \Rightarrow \|\mathbf{s}_{k+1}\| &= \frac{\|(\mathbf{CB}_d)^{-1}[\mathbf{s}_k - (\mathbf{CA}_d - \mathbf{C})\mathbf{x}_k]\| - \mathbf{u}_0}{\|(\mathbf{CB}_d)^{-1}\|} \end{aligned} \quad (2.56)$$

Thus:

$$\|\mathbf{s}_{k+1}\| \leq \|\mathbf{s}_k\| + \|(\mathbf{CA}_d - \mathbf{C})\mathbf{x}_k\| - \frac{\mathbf{u}_0}{\|(\mathbf{CB}_d)^{-1}\|} \quad (2.57)$$

The condition (2.51) can be applied for (2.57):

$$\frac{\mathbf{u}_0}{\|(\mathbf{CB}_d)^{-1}\|} > \|(\mathbf{CA}_d - \mathbf{C})\mathbf{x}_k\| \Rightarrow \|\mathbf{s}_{k+1}\| < \|\mathbf{s}_k\| \quad (2.58)$$

The inequality (2.58) proves the convergence to the sliding manifold of behavior of the system (2.44).

in the practical applications may be possible that the system parameter \mathbf{A} is unknown. In this case a suitable control law can be defined similar to (2.52):

$$\mathbf{u}_k = \begin{cases} -(\mathbf{CB}_d)^{-1} \mathbf{s}_k & \text{for } \|(\mathbf{CB}_d)^{-1} \mathbf{s}_k\| \leq \mathbf{u}_0 \\ -\mathbf{u}_0 \frac{(\mathbf{CB}_d)^{-1} \mathbf{s}_k}{\|(\mathbf{CB}_d)^{-1} \mathbf{s}_k\|} & \text{for } \|(\mathbf{CB}_d)^{-1} \mathbf{s}_k\| > \mathbf{u}_0 \end{cases} \quad (2.59)$$

Note that this control law complies with the bounds on the control resources. Substitution of (2.59) into (2.48) yields:

$$\mathbf{s}_{k+1} = \mathbf{s}_k \left(1 - \frac{\mathbf{u}_0}{\|(\mathbf{CB}_d)^{-1} \mathbf{s}_k\|} \right) + (\mathbf{CA}_d - \mathbf{C}) \mathbf{x}_k \quad \text{with } \mathbf{u}_0 < \|(\mathbf{CB}_d)^{-1} \mathbf{s}_k\| \quad (2.60)$$

Similar to (2.57) gives:

$$\begin{aligned} \|\mathbf{s}_{k+1}\| &\leq \|\mathbf{s}_k\| \left(1 - \frac{\mathbf{u}_0}{\|(\mathbf{CB}_d)^{-1} \mathbf{s}_k\|} \right) + \|(\mathbf{CA}_d - \mathbf{C}) \mathbf{x}_k\| \\ &\leq \|\mathbf{s}_k\| - \frac{\mathbf{u}_0}{\|(\mathbf{CB}_d)^{-1}\|} + \|(\mathbf{CA}_d - \mathbf{C}) \mathbf{x}_k\| \end{aligned} \quad (2.61)$$

and according to (2.51):

$$\|\mathbf{s}_{k+1}\| < \|\mathbf{s}_k\| \quad (2.62)$$

Therefore $\|\mathbf{s}_k\|$ decreases monotonically and, after a finite number of steps, control will be within the available resources $\|\mathbf{u}_k\| < \mathbf{u}_0$ as for the case with complete knowledge of system parameters.

In conclusion for a discrete-time system the discrete-time sliding mode control guarantees the avoid of the discretization chattering at least in a neighborhood of the sliding manifold in contrast to case that a continuous-time sliding mode control is implemented for the considered discrete-time system.

2.4 Continuous-time Integral Sliding Mode Control

In the case of classical sliding mode control for continuous systems the robustness property with respect to external disturbances and variation of system parameters is guaranteed only after occurring the sliding mode on the sliding surface $\mathbf{s}(\mathbf{x}) = \mathbf{0}$ in contrast it is not guaranteed during the reaching phase. In fact the main idea of sliding mode control for variable structure system is to force the state trajectory so that it lies on the sliding manifold in the state space, which is an intersection of a set of hyper-surfaces.

The control input commutes only after that sliding surface is reached by the state trajectory in order to confine the state trajectory at least in a neighborhood of the sliding manifold; only from this time instant onwards the behavior of the controlled system is governed by a motion equation with order $(n - m)$ lower compared to that of the original system. Moreover only starting from this time instant the dynamic response of the system is invariant with respect to variations of system parameters and external disturbances. During the reaching phase the robustness property of the control may be improved by using high-gain in the feedback control loop but this can compromise the stability of the whole system.

Integral Sliding Mode Control is an alternative control strategy to overcome the drawbacks of classical sliding mode control. In this case the robustness property of the control is guaranteed starting from the initial time instant and sliding mode occurs without a reaching phase. When the system is in an integral sliding mode on a manifold, the state trajectory is governed by a motion equation that has the same order than the original uncontrolled system (the order of motion equation is n).

In the following the definition of integral sliding mode is given [23]:

Definition 2.2: An sliding mode is said to be an integral sliding mode if the order of its equation motion is the same of the order of system.

Therefore with the implementation of integral sliding mode control the invariance property of the system with respect to variations of system parameters and external disturbances is achieved for the entire response of the system.

Furthermore integral sliding mode control is able to avoid the chattering phenomenon due to unmodeled dynamics that may be excited by the discontinuity of the control input.

2.4.1 Continuous-time Integral Sliding Mode Control design

The following state-space equation can be considered for a continuous-time dynamic system:

$$\dot{\mathbf{x}} = \mathbf{f}(\mathbf{x}) + \mathbf{B}(\mathbf{x})\mathbf{u} + \mathbf{h}(\mathbf{x}, t) \quad (2.63)$$

where $\mathbf{x} \in \mathbb{R}^n$ is the state vector, $\mathbf{u} \in \mathbb{R}^m$ is the control vector, $\mathbf{h}(\mathbf{x}, t)$ is a perturbation terms due to variations of system parameters and external disturbances and it is such that the following matching conditions are fulfilled:

$$\begin{cases} \mathbf{h}(\mathbf{x}, t) = \mathbf{B}(\mathbf{x})\mathbf{u}_h & \text{with } \mathbf{h} \in \mathbb{R}^m \\ |h_i(\mathbf{x}, t)| \leq h_i^+(\mathbf{x}, t) & \forall i = 1, 2, \dots, m \end{cases} \quad (2.64)$$

in other words all components of the vector control influences the perturbation term $\mathbf{h}(\mathbf{x}, t)$ by means of matrix $\mathbf{B}(\mathbf{x})$ and each component $h_i(\mathbf{x}, t)$ of the perturbation term is upper bound by a known positive scalar function $h_i^+(\mathbf{x}, t)$.

Let us that the state trajectory $\mathbf{x}(t)$ follows its reference $\mathbf{x}^*(t)$ when a feedback control law $\mathbf{u}^*(t)$ is applied and that under this control law the motion of state trajectory is invariant with respect to perturbation term:

$$\dot{\mathbf{x}}^*(t) = \mathbf{f}(\mathbf{x}^*) + \mathbf{B}(\mathbf{x}^*)\mathbf{u}^* \quad (2.65)$$

The objective of the integral sliding mode control is to design a suitable control law $\mathbf{u}(t)$ such that the state trajectory of the system (2.63) follows its reference starting from initial condition $\mathbf{x}(0) = \mathbf{x}^*(0)$ similar to case of application of $\mathbf{u}^*(t)$.

The control law can be rewritten as sum of two terms:

$$\mathbf{u}(t) = \mathbf{u}^* + \mathbf{u}_1 \quad (2.66)$$

where the ideal control $\mathbf{u}^* \in \mathbb{R}^m$ is defined by (2.65) and $\mathbf{u}_1 \in \mathbb{R}^m$ is designed in order to reject the perturbation term $\mathbf{h}(\mathbf{x}, t)$. A sliding surface can be defined as sum of two terms in the same manner of the control law:

$$\mathbf{s} = \mathbf{s}^*(\mathbf{x}) + \mathbf{z} \quad (2.67)$$

where $\mathbf{s}^*(\mathbf{x})$ is a linear combination of the state vector and it is designed by using conventional sliding mode theory; \mathbf{z} is an integral term and it is designed in order to achieve the integral sliding mode on the sliding manifold \mathbf{s} .

the substitution of (2.66) into (2.63) yields:

$$\dot{\mathbf{x}} = \mathbf{f}(\mathbf{x}) + \mathbf{B}(\mathbf{x})\mathbf{u}^* + \mathbf{B}(\mathbf{x})\mathbf{u}_1 + \mathbf{h}(\mathbf{x}, t) \quad (2.68)$$

The equivalent control $\mathbf{u}_{1,eq}$ of \mathbf{u}_1 must satisfy the following equation in order to achieve $\mathbf{x}(t) = \mathbf{x}^*(t)$:

$$\mathbf{B}(\mathbf{x})\mathbf{u}_{1,eq} = -\mathbf{h}(\mathbf{x}, t) \quad (2.69)$$

or in terms of (2.64):

$$\mathbf{u}_{1,eq} = \mathbf{u}_h \quad \text{with } \mathbf{h} \in \mathbb{R}^m \quad (2.70)$$

The integral term of the sliding surface (2.67) is designed in order to satisfy (2.70); for this reason the time derivative of sliding surface can be set to zero according to equivalent control theory:

$$\dot{\mathbf{s}} = \mathbf{s}^*(\mathbf{x}) + \dot{\mathbf{z}} = \frac{\partial \mathbf{s}^*}{\partial \mathbf{x}} (\mathbf{f}(\mathbf{x}) + \mathbf{B}(\mathbf{x})\mathbf{u}^* + \mathbf{B}(\mathbf{x})\mathbf{u}_{1,eq} + \mathbf{B}(\mathbf{x})\mathbf{u}_h) + \dot{\mathbf{z}} = \mathbf{0} \quad (2.71)$$

where $\dot{\mathbf{z}}$ is defined in order to guarantee (2.70) as follows:

$$\begin{cases} \frac{\partial \mathbf{s}^*}{\partial \mathbf{x}} (\mathbf{f}(\mathbf{x}) + \mathbf{B}(\mathbf{x})\mathbf{u}^* + \mathbf{B}(\mathbf{x})\mathbf{u}_{1,eq} + \mathbf{B}(\mathbf{x})\mathbf{u}_h) + \dot{\mathbf{z}} = \mathbf{0} \\ \mathbf{u}_{1,eq} = -\mathbf{u}_h \end{cases} \Rightarrow \quad (2.72)$$

$$\Rightarrow \dot{\mathbf{z}} = -\frac{\partial \mathbf{s}^*}{\partial \mathbf{x}} (\mathbf{f}(\mathbf{x}) + \mathbf{B}(\mathbf{x})\mathbf{u}^*)$$

with the initial condition $\mathbf{z}(0) = -\mathbf{s}^*(\mathbf{x}(0))$ derived by $\mathbf{s}(0) = \mathbf{0}$.

So the sliding mode occurs starting from initial time instant.

The motion equation of the system is equal to:

$$\dot{\mathbf{x}}(t) = \mathbf{f}(\mathbf{x}) + \mathbf{B}(\mathbf{x})\mathbf{u}^* \quad (2.73)$$

because choosing \mathbf{z} according to (2.72), the equation (2.70) is satisfied. Note that the motion equation (2.73) is the same of ideal case one (2.65) and its order is the same of the uncontrolled system (2.63). Therefore according to definition (2.2) an integral sliding mode is achieved on the sliding surface $\mathbf{s}(\mathbf{x}) = \mathbf{0}$ with well-known advantages.

2.5 Discrete-time Integral Sliding Mode Control

The advantages of integral sliding mode implementation for continuous-time dynamic systems with respect to a classical sliding mode control have been exposed in the previous Section 2.4.

In the present section the concept of integral sliding mode control will be extended to discrete-time systems in according to considerations of the discrete-time sliding mode control discussed in Section 2.3.

2.5.1 Discrete-time Integral Sliding Mode Control design

For a continuous-time linear dynamic system a corresponding continuous-time dynamic model may be defined as follows:

$$\dot{\mathbf{x}}(t) = \mathbf{A}\mathbf{x}(t) + \mathbf{B}\mathbf{u}(t) + \mathbf{D}(t) \quad (2.74)$$

where $\mathbf{x} \in \mathbb{R}^n$ is the state vector, $\mathbf{u} \in \mathbb{R}^m$ is the control input, \mathbf{A} and \mathbf{B} are system parameters matrices, $\mathbf{D}(t) = \mathbf{C} \cdot \mathbf{r}(t)$ is reference input matrix.

The discrete-time model corresponding to (2.74) is given by:

$$\mathbf{x}_{k+1} = \mathbf{A}_d \mathbf{x}_k + \mathbf{B}_d \mathbf{u}_k + \mathbf{D}_d \quad (\mathbf{A}_d = \mathbf{I} + \mathbf{A}T_s; \mathbf{B}_d = \mathbf{B}T_s; \mathbf{D}_d = \mathbf{D}T_s) \quad (2.75)$$

where the discrete-time matrices are expressed by using Euler's approximation and $\mathbf{x}_k = \mathbf{x}(kT_s)$, $\mathbf{u}_k = \mathbf{u}(kT_s)$ are the sampled vector with sampling period T_s corresponding to continuous-time vectors in (2.74).

The design of sliding manifold Σ should be such that the state trajectory follows its reference with desired dynamic features. The sliding manifold is generally defined as intersection of m switching surfaces $\mathbf{s}_{k,i} = \{\mathbf{x}_k / \mathbf{s}_i(\mathbf{x}_k) = \mathbf{0}\}$ being \mathbf{s}_i the i -th row of the sliding surface vector $\mathbf{s}_k = \mathbf{0}$.

The switching function \mathbf{s}_k should be designed so that the motion of the dynamic system (2.75) is stable when confined at least in a neighborhood of the sliding manifold $\Sigma = \{\mathbf{x}_k | \mathbf{s}_k = \mathbf{s}(\mathbf{x}_k) = 0\}$. Furthermore a suitable control law design is necessary to force the state trajectories on the sliding manifold Σ (reaching condition) keeping them belong the sliding manifold for all subsequent time instants (convergence condition).

According to it has been discussed in the Section 2.3. for the classical discrete-time sliding mode control implementation the switching function \mathbf{s}_k is define as follows:

$$\mathbf{s}_k = \mathbf{K}\mathbf{x}_k \quad (2.76)$$

where \mathbf{K} is a $m \times m$ matrix.

The introduction of an integral term into (2.76) is necessary to achieve an integral sliding mode:

$$\mathbf{s}_k = \mathbf{K}\mathbf{x}_k + \mathbf{z} \quad (2.77)$$

where the integral term is defined as follows:

$$\mathbf{z} = \mathbf{H}T_s \sum_{n=0}^{k-1} \mathbf{x}_n \quad (2.78)$$

The substitution of (2.78) into (2.77) leads to:

$$\mathbf{s}_k = \mathbf{K}\mathbf{x}_k + \mathbf{H}T_s \sum_{n=0}^{k-1} \mathbf{x}_n \quad (2.79)$$

where \mathbf{K} and \mathbf{H} are $m \times m$ matrices chosen according to desired dynamic behavior of the controlled system. The introduction of the integral term in the switching function (2.79) guarantees robustness property of the control against uncertainties of the system parameters starting from initial time instant because a sliding mode occurs without reaching phase similar to case of the continuous-time integral sliding mode control discussed in the Section 2.4.

It is necessary to satisfy the following condition in order to achieve a sliding mode:

$$\mathbf{s}_{k+1} = 0 \quad \text{with } k = 0, 1, 2, 3, \dots \quad (2.80)$$

From equation (2.79) follows that:

$$\mathbf{s}_{k+1} = \mathbf{K}\mathbf{x}_{k+1} + \mathbf{H}T_s \sum_{n=0}^k \mathbf{x}_n = \mathbf{s}_k + \mathbf{K}(\mathbf{x}_{k+1} - \mathbf{x}_k) + \mathbf{H}T_s \mathbf{x}_k \quad (2.81)$$

which according to (2.80) leads to:

$$\mathbf{x}_{k+1} = (\mathbf{I} - \mathbf{K}^{-1}\mathbf{H}T_s) \mathbf{x}_k \quad (2.82)$$

Since motion equation (2.82) has the same order of the original system (2.75) an integral sliding mode occurs on the sliding manifold Σ according to definition 2.2.

When the integral sliding mode occurs on the sliding manifold Σ , the behavior of the system (2.75) is governed by equation (2.82) it is invariant with respect to variations of the system parameters depending only by switching matrices \mathbf{K} and \mathbf{H} as it can be noted by (2.82).

As it has been discussed in the Section 2.3 for continuous-time integral sliding mode control, the control law can be redefined as sum of two terms:

$$\mathbf{u}_k = \mathbf{u}_{eq,k} + \mathbf{u}_{s,k} \quad (2.83)$$

where the continuous term $\mathbf{u}_{eq,k}$ is designed by using equivalent control method and the discontinuous term $\mathbf{u}_{s,k}$ is designed in order to guarantee the invariance of system against parametric uncertainties and external perturbations.

Therefore the first term of (2.83) is designed as solution of (2.81) with substitution of (2.75) into (2.81):

$$\mathbf{u}_{eq,k} = -(\mathbf{KB}_d)^{-1} [(\mathbf{KA}_d + T_s \mathbf{H} - \mathbf{K}) \mathbf{x}_k + \mathbf{KD}_d + \mathbf{s}_k] \quad (2.84)$$

where \mathbf{K} is chosen such that (\mathbf{KB}_d) is a nonsingular matrix. The continuous control $\mathbf{u}_{eq,k}$ is called *discrete-time equivalent control* according to the equivalent control method applied for the continuous- time systems.

The second term of (2.83) is designed as switching function of \mathbf{s}_k in order to improve the robustness property of control starting from the initial time instant and to reduce the reaching time:

$$\mathbf{u}_{s,k} = -(\mathbf{KB}_d)^{-1} [\mathbf{E} \text{sign}(\mathbf{s}_k)] \quad (2.85)$$

where \mathbf{E} is a positive constant matrix.

Since in an integral sliding mode control there is not reaching phase the state vector starting from the initial point \mathbf{x}_0 of the state space reaches theoretically in one sampling period the sliding manifold under the control vector $\mathbf{u}_{eq,k}$. However the control input must respects the bounds of the available control resources in order to prevent that is exceed them. For this reason the following condition must be imposed:

$$\begin{cases} \|\mathbf{u}_k\| \leq u_0 \\ \|(\mathbf{KB}_d)^{-1} \cdot \|[(\mathbf{KA}_d + T_s \mathbf{H} - \mathbf{K}) \mathbf{x}_k + \mathbf{KD}_d]\| < u_0 \end{cases} \quad (2.86)$$

where u_0 is the effective limits of available control resources. Therefore the control law is redesigned as follows:

$$\mathbf{u}_k = \begin{cases} \mathbf{u}_{eq,k} + \mathbf{u}_{s,k} & \text{for } \|\mathbf{u}_{eq,k} + \mathbf{u}_{s,k}\| \leq u_0 \\ u_0 \frac{\mathbf{u}_k}{\|\mathbf{u}_k\|} & \text{for } \|\mathbf{u}_{eq,k} + \mathbf{u}_{s,k}\| > u_0 \end{cases} \quad (2.87)$$

being $\|\mathbf{u}_k\| = (\mathbf{u}_k^T \mathbf{u}_k)^{1/2}$.

The satisfaction of sliding manifold reaching condition and convergence condition is equivalent to guarantee the overall stability of the integral sliding mode control. The following condition is obtained by means of simple equivalence with Lyapunov Theory for continuous-time system:

$$\mathbf{s}_k (\mathbf{s}_{k+1} - \mathbf{s}_k) < 0 \quad (2.88)$$

where the time derivative of \mathbf{s}_k is substituted by a forward difference. However the inequality (2.88) is necessary but not sufficient condition for the existence of a discrete-time sliding mode in contrast to the case of continuous-time systems [24]. In fact the only satisfaction of (2.88) not assures the convergence of the state trajectories on the sliding manifold and it may leads the system to instability exciting the chattering phenomenon in state motion.

The following condition is imposed in order to assure the stability of the whole control:

$$\|\mathbf{s}_{k+1}\| < \|\mathbf{s}_k\| \quad (2.89)$$

The proposed control law (2.87) satisfies (2.89) in the case $\|\mathbf{u}_k\| \leq u_0$ as discussed in the case of continuous-time integral sliding mode control. Therefore is necessary to prove the condition (2.88) in the case that $\|\mathbf{u}_k\| > u_0$. The substitution of (2.84) and (2.85) into (2.81) yields:

$$\mathbf{s}_{k+1} = \begin{bmatrix} (\mathbf{K}\mathbf{A}_d + T_s\mathbf{H} - \mathbf{K})\mathbf{x}_k + \\ + \mathbf{K}\mathbf{D}_d + \mathbf{s}_k \end{bmatrix} \left(1 - \frac{u_0}{\|\mathbf{u}_k\|} \right) - \mathbf{E} \text{sign}(\mathbf{s}_k) \frac{u_0}{\|\mathbf{u}_k\|} \quad (2.90)$$

Thus:

$$\|\mathbf{s}_{k+1}\| \leq \|\mathbf{s}_k\| + \left\| \begin{bmatrix} (\mathbf{K}\mathbf{A}_d + T_s\mathbf{H} - \mathbf{K})\mathbf{x}_k + \mathbf{K}\mathbf{D}_d \end{bmatrix} \right\| - \frac{u_0}{\|(\mathbf{K}\mathbf{B})^{-1}\|} < \|\mathbf{s}_k\| \quad (2.91)$$

by using (2.86). Hence similar to continuous-time integral sliding mode control discussed in Section 2.4, the value of $\|\mathbf{s}_k\|$ decreases monotonically and after a

finite number of sampling periods the control will be within the available control resources $\|\mathbf{u}_k\| \leq u_0$. Therefore the entire control law (2.87) satisfies the inequality (2.89) and guarantees a finite time convergence of the state vector to the sliding manifold and the state vector will be confined at least in a neighborhood of the sliding manifold for all subsequent time instants.

The constant matrices \mathbf{K} and \mathbf{H} of switching function (2.79) have rank m and these are chosen in order to achieve a desired dynamic behavior of the state trajectories in vicinity of the sliding manifold. If $\mathbf{s}_k \in \mathbb{R}^m$ and $\mathbf{x}_k \in \mathbb{R}^n$ the matrices \mathbf{K} and \mathbf{H} may be defined taking into account the following conditions [25]:

for \mathbf{K} :

- k.1) (\mathbf{KB}_d) is a nonsingular matrix;
- k.2) the $\left[\mathbf{A}_d - \mathbf{B}_d (\mathbf{KB}_d)^{-1} \mathbf{KA}_d \right]$ has m zero poles and $n - m$ poles inside the unit disk in the complex z -plane;

for \mathbf{H} :

- h.1) $\mathbf{H} = -\mathbf{K}[\mathbf{A}_d - I - \mathbf{B}_d \mathbf{G}]$ where \mathbf{G} is a matrix defined such that the poles of the $\mathbf{A}_d - \mathbf{B}_d \mathbf{G}$ matrix are distinct and within the unite circle around the origin of the complex z -plane.

2.5.2 Discrete-time Integral Sliding Mode Control with Disturbances Compensation and Reduced Chattering

In the following a discrete-time integral sliding mode control is designed in order to compensate the external disturbances and to reduce chattering phenomenon. Introducing into (2.74) a vector \mathbf{z} for tacking in account unmodeled dynamics and external disturbances, the model of system becomes:

$$\dot{\mathbf{x}}(t) = \mathbf{A}\mathbf{x}(t) + \mathbf{B}\mathbf{u}(t) + \mathbf{f}(t) \quad \text{with} \quad \mathbf{f}(t) = \mathbf{D} + \mathbf{z}(t) \quad (2.92)$$

where $\mathbf{z}(t)$ is a perturbation term representing matched disturbances.

The discrete-time representation of the system (2.92) with a sampling period T_s is given by;

$$\mathbf{x}_{k+1} = \mathbf{A}_d \mathbf{x}_k + \mathbf{B}_d \mathbf{u}_k + \mathbf{d}_k \quad \left(\begin{array}{l} \mathbf{A}_d = e^{A T_s}; \mathbf{B}_d = \int_0^{T_s} e^{A \lambda} \mathbf{B} d\lambda; \\ \mathbf{d}_k = \int_0^{T_s} e^{A \lambda} \mathbf{f}((k+1)T_s - \lambda) d\lambda \end{array} \right) \quad (2.93)$$

where $\mathbf{x}_k = \mathbf{x}(kT_s)$ and $\mathbf{u}_k = \mathbf{u}(kT_s)$ are the sampled vectors of the corresponding quantities in (2.92).

As it is well-known the first objective of the sliding mode control is to design a sliding manifold $\Sigma = \{\mathbf{x}_k : \mathbf{s}_k = \mathbf{s}(\mathbf{x}_k) = \mathbf{0}\}$ such that the state trajectories of the system have a desired dynamic behavior at least in a neighborhood of the sliding manifold, which is an intersection of m switching planes $\mathbf{s}_{k,i}$ (m is the dimension of the vector control $\mathbf{u}_k \in \mathbb{R}^m$), where $\mathbf{s}_{k,i} = \{\mathbf{x}_k : \mathbf{s}_i(\mathbf{x}_k) = \mathbf{0}\}$, being \mathbf{s}_i the i -th row of the matrix \mathbf{s}_k . Thus the problem is to design a switching function \mathbf{s}_k so that the motion of the dynamic system is stable when it is confined at least in a neighborhood of Σ .

An integral term is introduced in the switching function in order to overcome the main drawbacks of the classical discrete-time sliding mode control as it is discussed in the previous section:

$$\mathbf{s}_k = \mathbf{K} \mathbf{x}_k + \mathbf{H} T_s \sum_{n=0}^{k-1} \mathbf{x}_n \quad (2.94)$$

The occurring of a sliding mode on the sliding manifold Σ implies that:

$$\mathbf{s}_{k+1} = \mathbf{0} \quad \text{with } k = 0, 1, 2, 3, \dots \quad (2.95)$$

and substituting (2.94) into (2.95):

$$\mathbf{s}_{k+1} = \mathbf{K}\mathbf{x}_{k+1} + \mathbf{H}T_s \sum_{n=0}^k \mathbf{x}_n = \mathbf{s}_k + \mathbf{K}(\mathbf{x}_{k+1} - \mathbf{x}_k) + \mathbf{H}T_s \mathbf{x}_k \quad (2.96)$$

The motion equation of the state trajectories when the system is in the sliding mode is defined as follows:

$$\mathbf{x}_{k+1} = (\mathbf{I} - \mathbf{K}^{-1}\mathbf{H}T_s) \mathbf{x}_k \quad (2.97)$$

The control vector can be formulated similar to one of previous section:

$$\mathbf{u}_k = \mathbf{u}_{eq,k} + \mathbf{u}_{s,k} \quad (2.98)$$

where the discrete-time equivalent control $\mathbf{u}_{eq,k}$ is obtained by substituting (2.93) into (2.96) with the discontinuous control term $\mathbf{u}_{s,k}$ set to zero:

$$\mathbf{u}_{eq,k} = -(\mathbf{K}\mathbf{B}_d)^{-1} \left[(\mathbf{K}\mathbf{A}_d + T_s\mathbf{H} - \mathbf{K}) \mathbf{x}_k + \mathbf{K}\hat{\mathbf{d}}_k + \mathbf{s}_k \right] \quad (2.99)$$

The continuous term $\mathbf{u}_{eq,k}$ of the vector control is the proper control since under it the state vector starting from an initial point reaches the sliding manifold in finite time and remains along the sliding manifold or at least in a neighborhood of it for all subsequent time instants; in addition the chattering phenomenon does not occur because $\mathbf{u}_{eq,k}$ is a continuous function.

The discontinuous term $\mathbf{u}_{s,k}$ of the control vector is designed such that a reduced reaching time is achieved in order to improve the robustness property of the whole sliding mode control:

$$\mathbf{u}_{s,k} = -(\mathbf{K}\mathbf{B}_d)^{-1} \left[\mathbf{E} \text{sign}(\mathbf{s}_k) \right] \quad (2.100)$$

where \mathbf{E} is a positive constant matrix.

Moreover, the following conditions must be satisfied in order to respects the bounds u_0 of the available control resources since in integral sliding mode there is not a reaching phase and the control input may exceed the available

control resources tending to infinity if the initial state is far from the sliding manifold Σ or if the sampling period T_s is very small as it has been discussed in the previous sub-section 2.5.1.:

$$\begin{cases} \|\mathbf{u}_k\| \leq u_0 \\ \left\| (\mathbf{KB})^{-1} \cdot \left\| [(\mathbf{KA}_d + T_s \mathbf{H} - \mathbf{K})\mathbf{x}_k + \mathbf{K}\hat{\mathbf{d}}_k] \right\| \right\| < u_0 \end{cases} \quad (2.101)$$

As a result of these issues the control law is reformulated as follows:

$$\mathbf{u}_k = \begin{cases} \mathbf{u}_{eq,k} + \mathbf{u}_{s,k} & \text{for } \|\mathbf{u}_{eq,k} + \mathbf{u}_{s,k}\| \leq u_0 \\ u_0 \frac{\mathbf{u}_k}{\|\mathbf{u}_k\|} & \text{for } \|\mathbf{u}_{eq,k} + \mathbf{u}_{s,k}\| > u_0 \end{cases} \quad (2.102)$$

being $\|\mathbf{u}_k\| = (\mathbf{u}_k^T \mathbf{u}_k)^{1/2}$ control law guarantees the global stability of the sliding mode control as proved in sub-section 2.5.1. Note that the implementation of control law (2.102) would requires the a priori knowledge of the disturbance term \mathbf{d}_k ; for this reason \mathbf{d}_k may be estimated by its value corresponding to previous sampling point \mathbf{d}_{k-1} with some continuity assumption on the disturbances [8]

$$\hat{\mathbf{d}}_k = \mathbf{d}_{k-1} = \mathbf{x}_k - \mathbf{A}_d \mathbf{x}_{k-1} - \mathbf{B}_d \mathbf{u}_{k-1} \quad (2.103)$$

thus, the discrete-time equivalent control (2.99) becomes:

$$\mathbf{u}_{eq,k} = -(\mathbf{KB}_d)^{-1} \left[(\mathbf{KA}_d + T_s \mathbf{H})\mathbf{x}_k + \mathbf{s}_k + \right. \\ \left. - \mathbf{K}(\mathbf{A}_d \mathbf{x}_{k-1} + \mathbf{B}_d \mathbf{u}_{k-1}) \right] \quad (2.104)$$

The choice of matrices \mathbf{K} and \mathbf{H} can be carried out as it has been discussed into sub-section 2.5.1. in order to assure a desired convergence of the state vector to the sliding manifold.

By the application of (2.103) a reduced chattering phenomenon is achieved in the sliding motion of the state trajectories at least in a neighborhood of the sliding manifold Σ .

When the system is in sliding mode on the sliding manifold equation (2.95) is verified for all time instants such that $t = kT_s$ with $k = 1, 2, \dots$

Consider the amplitude of the boundary layer of the sliding motion in the inter-sampling instant $t = kT_s + \tau$ with $0 < \tau < T_s$ in order to evaluate the maximum deviation of the state by the sliding manifold.

Considering the continuous-time system (2.92) and the corresponding continuous-time representation of the sliding function (2.94), the time derivative of the sliding surface equation $\mathbf{s} = 0$ is defined as:

$$\dot{\mathbf{s}} = \mathbf{K}\dot{\mathbf{x}} + \mathbf{H}\mathbf{x} = \mathbf{K}(\mathbf{A}\mathbf{x} + \mathbf{f}(t)) + \mathbf{H}\mathbf{x} + \mathbf{K}\mathbf{B}\mathbf{u} \quad (2.105)$$

Calculating the value of (2.93) for the inter-sample instant $t = kT_s + \tau$ and integrating both sides of (2.93) from T_s to $t = kT_s + \tau$:

$$\mathbf{s}(kT_s + \tau) = \mathbf{s}_k + \int_{kT_s}^{kT_s + \tau} [\mathbf{K}(\mathbf{A}\mathbf{x} + \mathbf{f}(t)) + \mathbf{H}\mathbf{x} + \mathbf{K}\mathbf{B}\mathbf{u}] dt \quad (2.106)$$

where $\mathbf{s}_k = \mathbf{s}(kT_s)$. Since in discrete-time integral sliding mode control the control law is a piecewise constant function, $\mathbf{u}(t) = \mathbf{u}_k$ during the sampling period, the (2.106) becomes:

$$\mathbf{s}(kT_s + \tau) = \mathbf{s}_k + \int_{kT_s}^{kT_s + \tau} [\mathbf{K}(\mathbf{A}\mathbf{x} + \mathbf{f}(t)) + \mathbf{H}\mathbf{x}] dt + \tau \mathbf{K}\mathbf{B}\mathbf{u}_k \quad (2.107)$$

In sliding mode $\mathbf{s}_{k+1} = \mathbf{s}_k = 0$ and the substitution of (2.99) into (2.107) yields:

$$\begin{aligned} \mathbf{s}(kT_s + \tau) = & \int_{kT_s}^{kT_s + \tau} [\mathbf{K}(\mathbf{A}\mathbf{x} + \mathbf{f}(t)) + \mathbf{H}\mathbf{x}] dt + \\ & -\tau(\mathbf{K}\mathbf{B})(\mathbf{K}\mathbf{B}_d)^{-1} \left[\begin{array}{l} (\mathbf{K}\mathbf{A}_d + T_s\mathbf{H} - \mathbf{K})\mathbf{x}_k + \\ + \mathbf{K}\hat{\mathbf{d}}_k \end{array} \right] \end{aligned} \quad (2.108)$$

Since the state vector \mathbf{x} and the perturbation term $\mathbf{f}(t)$ are smooth and bounded, the integration term of (2.108) can be approximated by using Euler's method as follows:

$$\begin{aligned} & \int_{kT_s}^{kT_s+\tau} [\mathbf{K}(\mathbf{Ax} + \mathbf{f}(t)) + \mathbf{Hx}] dt = \\ & = \tau [\mathbf{K}(\mathbf{Ax}(kT_s) + \mathbf{f}(kT_s)) + \mathbf{Hx}(kT_s)] + O(\tau^2) \end{aligned} \quad (2.109)$$

Similarly, \mathbf{A}_d , \mathbf{d}_k and \mathbf{B}_d can be approximated by using Euler's method and Taylor's series expansion truncated to the first term:

$$\begin{aligned} \mathbf{A}_d &= \mathbf{I} + \mathbf{A}T_s + O(T_s^2); \quad \mathbf{B}_d = \mathbf{B}T_s + O(T_s^2); \\ \mathbf{d}_k &= T_s \mathbf{f}((k+1)T_s - t) + O(T_s^2) = T_s \mathbf{f}(kT_s) + O(T_s^2) \end{aligned} \quad (2.110)$$

The substitution of (2.110) into second side of (2.108) yields:

$$\begin{aligned} & (\mathbf{KB})(\mathbf{KB}_d)^{-1} [(\mathbf{KA}_d + T_s \mathbf{H} - \mathbf{K})\mathbf{x}_k + \mathbf{K}\hat{\mathbf{d}}_k] = \\ & = [\mathbf{KAx}_k + \mathbf{Hx}_k + \mathbf{Kf}(kT_s)] + O(T_s^2) \end{aligned} \quad (2.111)$$

With the introduction of two auxiliary variables defined as follows:

$$q_1 = \int_{kT_s}^{kT_s+\tau} [\mathbf{K}(\mathbf{Ax} + \mathbf{f}(t)) + \mathbf{Hx}] dt - \tau [\mathbf{K}(\mathbf{Ax}(kT_s) + \mathbf{f}(kT_s)) + \mathbf{Hx}(kT_s)] \quad (2.112)$$

$$\begin{aligned} q_2 &= (\mathbf{KB})(\mathbf{KB}_d)^{-1} [(\mathbf{KA}_d + T_s \mathbf{H} - \mathbf{K})\mathbf{x}_k + \mathbf{K}\hat{\mathbf{d}}_k] + \\ & - [\mathbf{KAx}_k + \mathbf{Hx}_k + \mathbf{Kf}(kT_s)] \end{aligned} \quad (2.113)$$

equation (2.108) becomes:

$$\mathbf{s}(kT_s + \tau) = q_1 - \tau q_2 \leq O(T_s^2) \quad (2.114)$$

The last inequality proved that the maximum deviation of the state trajectory by the sliding manifold is equal to $O(T_s^2)$, which is lower than what can be achieved by means of a classical discrete-time sliding mode control, that instead has thickness $O(T_s)$ [26].

2.6 Higher-Order Sliding Mode Control

As discussed in previous sections the sliding mode control is able to guarantee high performance in the tracking of the reference values with respect to variations of the system parameters and external disturbances; in contrast it is characterized by chattering phenomenon due to unmodeled dynamics which are neglected in the control design.

The chattering phenomenon can be avoided by using high-order sliding mode control (HOSMC), that involves the high-order time-derivatives of the switching function in contrast to the classical sliding mode control that involves only the first time-derivative of the switching function. So the chattering phenomenon can be avoided and at the same time the robustness property of the classical sliding mode control are kept.

Considering the following sliding surface:

$$s = 0 \tag{2.115}$$

the r -th order sliding mode is defined as follows:

$$s = \dot{s} = \ddot{s} = \dots = s^{(r-1)} = 0 \tag{2.116}$$

In other words, the order of the sliding mode corresponds to the number of the time-derivatives of the switching function s set to zero (including the zero-order) in a small vicinity of the sliding manifold.

As can be noted by (2.116) the r -th order sliding mode involves an r -dimensional condition on the system state.

However the HOSMC assures typically an asymptotically convergence of the state trajectories to the sliding manifold in contrast to the classical sliding mode control that assure a finite time convergence being a first order sliding mode (\dot{s} is discontinuous function). Moreover only in the case of finite time convergence, the maximum r -th order of accuracy with respect to the sampling period is achieved by using HOSMC.

The main drawbacks of HOSMC implementation consist of it needs $s = \dot{s} = \ddot{s} = \dots = s^{(r-1)}$ to be available and only in the case of Super-Twisting 2-sliding mode control the only knowledge of s is sufficient.

In the following sections the second-order sliding mode control (or called as “2-sliding mode control”) will be discussed.

2.6.1 2-Sliding Mode Control

A general continuous-time system can be defined as:

$$\dot{\mathbf{x}} = \mathbf{f}(t, \mathbf{x}, \mathbf{u}) \quad (2.117)$$

where $\mathbf{x} \in \mathbb{R}^n$ is the state vector, $\mathbf{u} = \mathbf{u}(t, \mathbf{x}) \in \mathbb{R}^m$ is the control input and $\mathbf{f}(t, \mathbf{x}, \mathbf{u})$ a smooth function. Let us consider a discontinuous control law:

$$\mathbf{u}(t, \mathbf{x}) = \begin{cases} \mathbf{u}_0 & \text{for } \mathbf{s}(\mathbf{x}) > \mathbf{0} \\ -\mathbf{u}_0 & \text{for } \mathbf{s}(\mathbf{x}) \leq \mathbf{0} \end{cases} \quad (2.118)$$

where $\mathbf{s}(t, \mathbf{x}) = \mathbf{0}$ is the sliding manifold.

Two different cases may arise considering time-derivatives of $\mathbf{s}(t, \mathbf{x})$ [27]:

$$\begin{aligned} 1) \quad r=1 &\Rightarrow \dot{\mathbf{s}} \neq \mathbf{0} \\ 2) \quad r=2 &\Rightarrow \mathbf{s}^{(i)} = \mathbf{0} \text{ for } i=1,2,\dots,r-1 \text{ and } \mathbf{s}^{(r)} \neq \mathbf{0} \end{aligned} \quad (2.119)$$

where r is the relative order of the system. Moreover a 2-sliding mode control can be implemented in order to avoid chattering phenomenon; in this case the considered control variable is $\dot{\mathbf{u}}$ (the first time-derivative of control input) that is calculated by keeping $\mathbf{s} = \mathbf{0}$ in the 2-sliding mode control such that the control input \mathbf{u} of the plant to be a continuous function and chattering is avoided.

Assuming that function $\mathbf{f}(t, \mathbf{x}, \mathbf{u})$ into (2.117) to be a C^1 function and \mathbf{s} to be a C^2 function and that available current information corresponding only to the current values of t , $\mathbf{u}(t)$ and $\mathbf{s}(t, \mathbf{x})$; thus the second derivative of the sliding variable \mathbf{s} is defined as follows:

$$\begin{aligned} \dot{\mathbf{s}} &= \frac{\partial \mathbf{s}(t, \mathbf{x})}{\partial t} + \frac{\partial \mathbf{s}(t, \mathbf{x})}{\partial \mathbf{x}} \mathbf{f}(t, \mathbf{x}, \mathbf{u}) \\ \ddot{\mathbf{s}}(t) &= \frac{\partial \dot{\mathbf{s}}(t, \mathbf{x}, \mathbf{u})}{\partial t} + \frac{\partial}{\partial \mathbf{x}} \dot{\mathbf{s}}(t, \mathbf{x}, \mathbf{u}) \mathbf{f}(t, \mathbf{x}, \mathbf{u}) + \frac{\partial}{\partial \mathbf{u}} \dot{\mathbf{s}}(t, \mathbf{x}, \mathbf{u}) \dot{\mathbf{u}}(t) \end{aligned} \quad (2.120)$$

Let the second order derivative of the switching variable \mathbf{s} to be uniformly bounded in a boundary domain. Therefore the equivalent control theory can be used in order to compute the equivalent control $\mathbf{u}_{eq}(t, \mathbf{x})$ such that the equality $\dot{\mathbf{s}}=0$ is satisfied. Moreover, if the uncontrolled system is represented by a second-order equations system the control input \mathbf{u} can be considered as state variable and $\dot{\mathbf{u}}$ becomes the control variable.

2.6.1.1 Twisting Algorithm

With the introduction of two auxiliary variables defined as:

$$\begin{cases} y_1 = \mathbf{s} \\ y_2 = \dot{\mathbf{s}} \end{cases} \quad (2.121)$$

the second-order sliding mode control has the following associated second-order system:

$$\begin{cases} \dot{y}_1 = y_2 \\ \dot{y}_2 = \varphi(t, \mathbf{x}) + \gamma(t, \mathbf{x})\dot{\mathbf{u}} \end{cases} \quad \text{with} \quad \begin{cases} |\varphi| \leq \Phi, \Phi > 0 \\ 0 < \Gamma_m \leq \gamma \leq \Gamma_M \end{cases} \quad (2.122)$$

where $\varphi(t, \mathbf{x})$ and $\gamma(t, \mathbf{x})$ are uncertain functions such that the control law to be [10]:

$$\dot{\mathbf{u}}(t) = \begin{cases} -\mathbf{u} & \text{if } \|\mathbf{u}\| > 1 \\ -V_m \cdot \text{sign}(y_1) & \text{if } y_1 y_2 \leq 0, \|\mathbf{u}\| \leq 1 \\ -V_M \cdot \text{sign}(y_1) & \text{if } y_1 y_2 > 0, \|\mathbf{u}\| \leq 1 \end{cases} \quad (2.123)$$

To achieve the finite time convergence to the sliding manifold the following conditions are sufficient:

$$\begin{cases} V_M > V_m \\ V_m > \frac{4\Gamma_M}{s_0} \\ V_m > \frac{\Phi}{\Gamma_m} \\ \Gamma_m V_M - \Phi > \Gamma_M V_m + \Phi \end{cases} \quad (2.124)$$

In this case the state trajectories converge to the origin of the 2-sliding plane $y_1 O y_2$ with finite time performing an infinite number of rotations which decrease in geometrical progression as shown in Fig. 2.6. The derivative value of the control $\dot{\mathbf{u}}$ commutes at each axis crossing; for this reason is necessary that the sign of the time-derivative of the sliding variable (y_2) to be available.

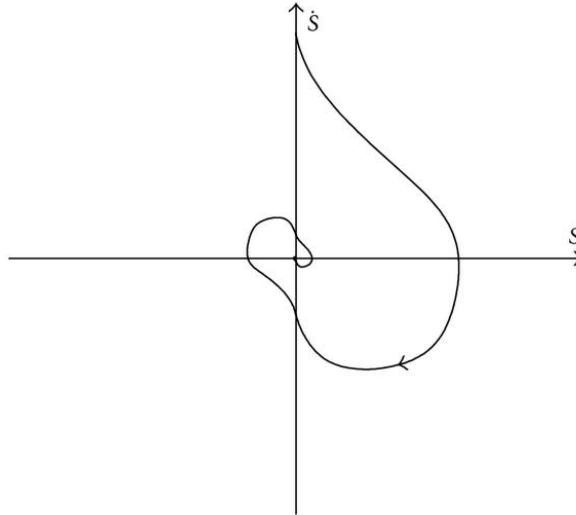


Fig. 2.6. Twisting-algorithm phase trajectory

In the practical applications y_2 may be immeasurable; therefore its sign can be evaluated by the sign of the first difference of the available sliding variable y_1 in a time interval τ as follows:

$$\text{sign}(y_2(t)) = \text{sign}(y_1(t) - y_1(t - \tau)) \quad (2.125)$$

In this last case the 2-sliding accuracy with respect to the sampling period τ is achieved and boundary layer size of the sliding manifold is about $O(\tau^2)$.

2.6.1.2 Super-Twisting Algorithm

The use of Super-Twisting algorithm provides that the state trajectories converge to the origin of the 2-sliding plane y_1Oy_2 performing in twisting around the origin as it has been shown in the previous case of twisting algorithm.

By using Super-Twisting Algorithm the control law is defined as sum of two terms:

$$\mathbf{u}(t) = \mathbf{u}_1(t) + \mathbf{u}_2(t) \quad (2.126)$$

where the first component is defined by means of its discontinuous time-derivative and the second component is defined as continuous function of sliding variable y_1 as follows:

$$\begin{aligned} \dot{\mathbf{u}}_1(t) &= \begin{cases} -\mathbf{u} & \text{if } \|\mathbf{u}\| > 1 \\ -W \cdot \text{sign}(y_1) & \text{if } \|\mathbf{u}\| \leq 1 \end{cases} \\ \mathbf{u}_2(t) &= \begin{cases} -\lambda |s_0|^\rho \cdot \text{sign}(y_1) & \text{if } \|y_1\| > s_0 \\ -\lambda |y_1|^\rho \cdot \text{sign}(y_1) & \text{if } \|y_1\| \leq s_0 \end{cases} \end{aligned} \quad (2.127)$$

The satisfaction of the following conditions is sufficient to achieved a finite time convergence of the state trajectories to the sliding manifold [27]:

$$\begin{cases} W > \frac{\Phi}{\Gamma_m} \\ \lambda^2 \geq \frac{4\Phi \Gamma_M (W + \Phi)}{\Gamma_m^2 \Gamma_m (W - \Phi)} \\ 0 < \rho \leq 0.5 \end{cases} \quad (2.128)$$

If the controlled system is linearly dependent on control input $\mathbf{u}(t)$, the control law can be simplified as follows:

$$\begin{aligned}\mathbf{u} &= -\lambda \|\mathbf{s}\|^p \cdot \text{sign}(y_1) + \mathbf{u}_1 \\ \dot{\mathbf{u}}_1 &= -W \cdot \text{sign}(y_1)\end{aligned}\tag{2.129}$$

As it can be noted the Super-Twisting algorithm implementation does not need to know the sign of the time-derivative of the sliding variable y_2 but only that the sliding function $y_1 = \mathbf{s}$ to be available; this is its main advantage with respect to implementation of other second-order sliding mode control.

Furthermore details on other higher-order sliding mode control technique can be found into [28].

2.7 Sliding Mode Observer

In practice the state vector is typically available only in part (only a part of its components is known). However the components not available of the state vector can be estimated by means of an observer starting from the part of components directly measured. These components are called “observed” components.

In the following before a conventional observer will be explained and then a sliding mode observer for linear time-invariant systems will be discussed.

2.7.1 Conventional Observer

Let us consider a linear time-invariant multidimensional system:

$$\begin{cases} \dot{\mathbf{x}} = \mathbf{A}\mathbf{x} + \mathbf{B}\mathbf{u} \\ \mathbf{y} = \mathbf{C}\mathbf{x} \end{cases} \quad (2.130)$$

where \mathbf{x} and \mathbf{u} are n and m dimensional state and control vector respectively, \mathbf{A} and \mathbf{B} are constant matrices with $\text{rank}(\mathbf{B}) = m$, \mathbf{y} is the output vector of the system with $\mathbf{y} \in \mathbb{R}^l$ and \mathbf{C} is a constant matrix with $\text{rank}(\mathbf{C}) = l$. In addition let that the pair (\mathbf{C}, \mathbf{A}) to be observable. Considering the difference between the actual value and the observed value of the output vector, a conventional observer may be designed with the same form of system (2.130) as follows:

$$\dot{\hat{\mathbf{x}}} = \mathbf{A}\hat{\mathbf{x}} + \mathbf{B}\mathbf{u} + \mathbf{K}(\mathbf{C}\hat{\mathbf{x}} - \mathbf{y}) \quad (2.131)$$

where $\hat{\mathbf{x}}$ is the observed value of the state vector and $\mathbf{K} \in \mathbb{R}^{n \times l}$ is the constant observation matrix.

Subtracting (2.131) from (2.130) the following motion equation for the mismatch $\bar{\mathbf{x}} = \hat{\mathbf{x}} - \mathbf{x}$ is obtained:

$$\dot{\bar{\mathbf{x}}} = \mathbf{A}\bar{\mathbf{x}} + \mathbf{K}\mathbf{C}\bar{\mathbf{x}} = (\mathbf{A} + \mathbf{K}\mathbf{C})\bar{\mathbf{x}} \quad (2.132)$$

Assigning the eigenvalues of the matrix $(\mathbf{A} + \mathbf{K}\mathbf{C})$ by means of a suitable choice of observation matrix \mathbf{K} , the desired convergence rate of the mismatch $\bar{\mathbf{x}}$ to zero is achieved (or equivalently the desired convergence rate of the estimated state vector $\hat{\mathbf{x}}$ to actual one \mathbf{x}). Consequently any control algorithms with vector $\hat{\mathbf{x}}$ are applicable, also full-state control algorithms.

2.7.2 Sliding Mode Observer design

In a sliding mode observer design for linear time-invariant system (2.130) has a structure very similar to conventional observer (2.131) with replacement of the continuous additional term by a discontinuous function of the output observation error [29]:

$$\dot{\hat{\mathbf{x}}} = \mathbf{A}\hat{\mathbf{x}} + \mathbf{B}\mathbf{u} + \mathbf{K} \text{sign}(\mathbf{y} - \mathbf{C}\hat{\mathbf{x}}) \quad (2.133)$$

Choosing a suitable gain observation matrix \mathbf{K} , the sliding mode for system (2.133) occurs on the surface $\mathbf{y} - \mathbf{C}\hat{\mathbf{x}} = \mathbf{0}$ and (2.133) becomes equivalent to A reduced order observer [30].

This result will be proved in the following.

Set:

$$\mathbf{x}^T = [\mathbf{x}_1 \quad \mathbf{x}_2]^T \quad \text{with } \mathbf{x}_1 \in \mathbb{R}^{n-l}, \mathbf{x}_2 \in \mathbb{R}^l, \text{rank}(\mathbf{C}) = l \quad (2.134)$$

thus:

$$\mathbf{y} = \mathbf{C}_1\mathbf{x}_1 + \mathbf{C}_2\mathbf{x}_2 \quad \text{with } \det(\mathbf{C}_2) \neq 0 \quad (2.135)$$

In this case is sufficient to design an observer only for vector \mathbf{x}_1 because the components of vector \mathbf{x}_2 may be calculated as function of \mathbf{x}_1 [30]:

$$\mathbf{x}_2 = \mathbf{C}_2^{-1}(\mathbf{y} - \mathbf{C}_1\mathbf{x}_1) \quad (2.136)$$

The system (2.130) can be rewritten by using linear transformation of state variables as follows:

$$\begin{cases} \dot{\hat{\mathbf{x}}}_1 = \mathbf{A}_{11}\mathbf{y} + \mathbf{A}_{12}\mathbf{x}_1 + \mathbf{B}_1\mathbf{u} & \text{(a)} \\ \dot{\hat{\mathbf{y}}} = \mathbf{A}_{21}\mathbf{y} + \mathbf{A}_{22}\mathbf{x}_1 + \mathbf{B}_2\mathbf{u} & \text{(b)} \end{cases} \quad (2.137)$$

where:

$$\mathbf{TAT}^{-1} = \begin{bmatrix} \mathbf{A}_{11} & \mathbf{A}_{12} \\ \mathbf{A}_{21} & \mathbf{A}_{22} \end{bmatrix}, \mathbf{TB} = \begin{bmatrix} \mathbf{B}_1 \\ \mathbf{B}_2 \end{bmatrix}, \mathbf{T} = \begin{bmatrix} \mathbf{I}_{n-l} & \mathbf{0} \\ \mathbf{C}_1 & \mathbf{C}_2 \end{bmatrix} \quad (2.138)$$

with the coordinate transformation is nonsingular $\Rightarrow \det(\mathbf{T}) \neq 0$.

The motion preceding the sliding mode and the motion on the intersection of sliding manifold can be considered independently for design the sliding mode observer. According to that has been discussed above, the corresponding sliding mode observer for (2.137 (b)) is:

$$\dot{\hat{\mathbf{y}}} = \mathbf{A}_{21}\hat{\mathbf{y}} + \mathbf{A}_{22}\hat{\mathbf{x}}_1 + \mathbf{B}_2\mathbf{u} + \mathbf{L}_2 \text{sign}(\mathbf{y} - \hat{\mathbf{y}}) \quad (2.139)$$

Subtracting (2.317 (b)) from (2.139) the following system respect to mismatch $\bar{\mathbf{y}} = \hat{\mathbf{y}} - \mathbf{y}$ can be obtained:

$$\dot{\bar{\mathbf{y}}} = \mathbf{A}_{21}\bar{\mathbf{y}} + \mathbf{A}_{22}\bar{\mathbf{x}}_1 - \mathbf{L}_2 \text{sign}(\bar{\mathbf{y}}) \quad (2.140)$$

Choosing a suitable gain matrix \mathbf{L}_2 the sliding mode occurs for system (2.140) on the sliding surface $\bar{\mathbf{y}} = \mathbf{0}$, then $\hat{\mathbf{y}}$ tends to \mathbf{y} .

The corresponding sliding mode observer for (2.137 (a)) is structured similar to (2.139):

$$\dot{\hat{\mathbf{x}}}_1 = \mathbf{A}_{11}\mathbf{y} + \mathbf{A}_{12}\hat{\mathbf{x}}_1 + \mathbf{B}_1\mathbf{u} - \mathbf{L}_1\mathbf{L}_2 \text{sign}(\mathbf{y} - \hat{\mathbf{y}}) \quad (2.141)$$

The subtraction of (2.137 (a)) from (2.141) gives the following equation for the mismatch $\bar{\mathbf{x}}_1 = \hat{\mathbf{x}}_1 - \mathbf{x}_1$:

$$\dot{\bar{\mathbf{x}}}_1 = \mathbf{A}_{12}\bar{\mathbf{x}}_1 - \mathbf{L}_1\mathbf{L}_2 \text{sign}(\bar{\mathbf{y}}) \quad (2.142)$$

Let us consider the term $\mathbf{L}_2 \text{sign}(\bar{\mathbf{y}})$ as control variable for (2.142). According to equivalent control theory, in sliding mode the system (2.142) behaves as if $\mathbf{u} = \mathbf{L}_2 \text{sign}(\bar{\mathbf{y}})$ is replaced by its equivalent value $\mathbf{u}_{eq} = (\mathbf{L}_2 \text{sign}(\bar{\mathbf{y}}))_{eq}$, that can be calculated by system (2.140) with the constraints $\bar{\mathbf{y}} = \mathbf{0}$ and $\dot{\bar{\mathbf{y}}} = \mathbf{0}$:

$$(\mathbf{L}_2 \text{sign}(\bar{\mathbf{y}}))_{eq} = \mathbf{A}_{22}\bar{\mathbf{x}}_1 \quad (2.143)$$

The substitution of (2.143) into (2.142) yields:

$$\dot{\bar{\mathbf{x}}}_1 = (\mathbf{A}_{12} - \mathbf{A}_{22}\mathbf{L}_1)\bar{\mathbf{x}}_1 \quad (2.144)$$

Consequently if the system (2.130) is observable (the pair (\mathbf{C}, \mathbf{A}) is observable) then the pair $(\mathbf{A}_{12}, \mathbf{A}_{22})$ is observable too. Thus designing an appropriate observation gain matrix \mathbf{L}_1 for (2.142) a sliding mode occurs on the surface $\bar{\mathbf{x}}_1 = \mathbf{0}$ with a desired convergence rate to it ($\hat{\mathbf{x}}_1$ tends to \mathbf{x}_1).

In conclusion the vector \mathbf{x}_2 can be calculated by (2.136) and any full-state control algorithms are applicable to considered system.

Chapter 3

ELECTRICAL SUBSYSTEM: MODELING AND DESIGN

In this Section the proposed electrical subsystem is explained and its main components are modeled and designed. The control strategy adopted for the converters of the proposed electrical sub-system is a feedback modulation based on the sliding mode control because it is able to guarantee good dynamic performance and high robustness property.

The proposed electrical sub-system that can be treated as a Double Stage AC-AC Power Converter (DSACPC) consists of two fundamental parts as shown in Fig. 3.1:

- the **Stage 1** consists of a PMSG coupled in axis with turbine, a boost-type PWM rectifier and a DC-link capacitors bank; these components are controlled by means of full sliding mode control that is constituted by the Back-EMF and rotor angle sliding mode observer, an Integral Sliding Mode Control (ISMC) for the DC-link voltage control, a Super-Twisting Integral Sliding Mode Control (ST-ISMC1) in order to achieve a sliding mode current control of the Stage 1;

- the **Stage 2** consists of a three-phase Voltage Source Inverter (VSI) and a three-phase step-up transformer connected to the grid utility; the VSI is controlled by means of a Super-Twisting Integral Sliding Mode Control (ST-ISMC2) in order to achieve a sliding mode current control of the Stage 2.

The Space Vector PWM (SVPWM) has been used for generate the switching pulses of the power electronic converters of both stages.

For the Stage 1 the control strategy is based on a full-sliding mode control and it is formulated in a rotating reference frame synchronous with the electrical angular velocity of the PMSG in order to achieve the following goals:

- 1.a) keeping the DC-link voltage at a desired value;
- 1.b) tracking of the maximum power point draw from the thermodynamic sub-system.

For the Stage 2 the control strategy is based on second-order integral sliding mode control that is formulated in a rotating reference frame synchronous with the electrical angular velocity of the grid utility in order to achieve the following goals depending on the balancing grid utility conditions:

- 2.a) generation of desired values of instantaneous active and reactive power on the grid utility, in the case of balanced conditions of the grid utility;
- 2.b) current harmonic rejection, in the case of unbalanced conditions of the grid utility.

In the following the mathematical models and principal characteristics of the main components of both stages are treated.

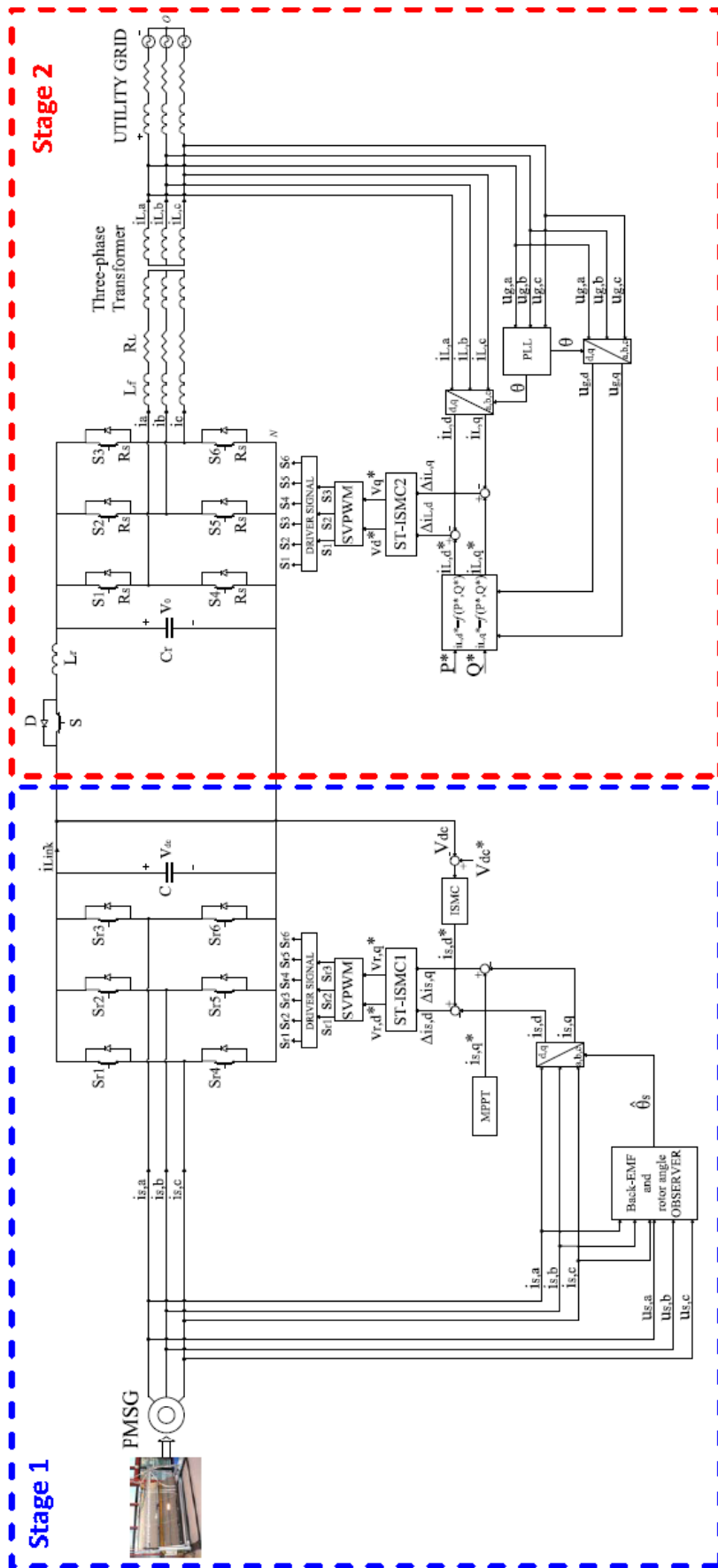


Fig. 3.1. Schema of the proposed Electrical sub-system.

3.1 Stage 1: Components Modeling and Control Strategy

In this section the mathematical model of the PMSG and the three-phase boost-type PWM rectifier is explained; according to latter the proposed control strategy of Stage 1 will be discussed with a thorough explanation of all its parts.

3.1.1 Permanent Magnet Synchronous Generator

A Permanent Magnet Synchronous Generator (PMSG) has been adopted for power electric generation because of its many advantages, such as simple configuration and lossless field circuit with respect to other types of electrical generator.

Fig. 3.2 shows the electrical schema of the PMSG stator winding:

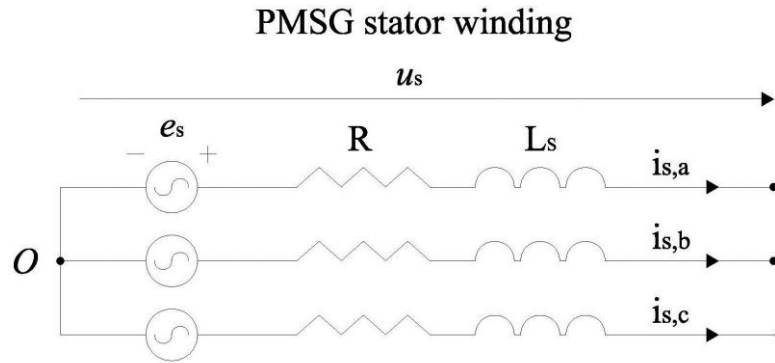


Fig. 3.2. Electrical schema of the PMSG stator winding.

The mathematical model of PMSG in the rotating reference frame (d,q frame) having the d-axis coincident with direction of the magnetic flux of the permanent magnets is defined as:

$$\begin{cases} \frac{di_{sd}}{dt} = -\frac{R}{L_{sd}}i_{sd} + \frac{L_{sq}}{L_{sd}}\omega_s i_{sq} + \frac{u_{sd}}{L_{sd}} \\ \frac{di_{sq}}{dt} = -\frac{R}{L_{sq}}i_{sq} - \frac{L_{sd}}{L_{sq}}\omega_s i_{sd} - \frac{\omega_s \Psi}{L_{sq}} + \frac{u_{sq}}{L_{sq}} \end{cases} \quad (3.1)$$

where u_{sd} and u_{sq} are the d-q axis components of the output phase voltages of the stator, i_{sd} and i_{sq} are the d-q axis components of the output phase currents of the stator, Ψ is the magnetic flux of permanent magnets, ω_s is the electrical angular velocity of the rotor, R is the resistance of the stator winding, L_{sd} and L_{sq} the self-inductance in d-q frame of the stator winding.

The PMSG electromagnetic torque expression is:

$$T_e = \frac{3}{2} p \Psi i_{sq} + \frac{3}{2} p (L_{sd} - L_{sq}) i_{sd} i_{sq} \quad (3.2)$$

where p is the number of pole pairs of the stator winding.

3.1.2 Three-phase PWM rectifier

The main power electronic converter of the Stage 1 is the three-phase PWM rectifier as shown in Fig. 3.1, which is directly connected to the stator of the PMSG.

The electrical diagram of the three-phase PWM rectifier is shown in Fig. 3.3.

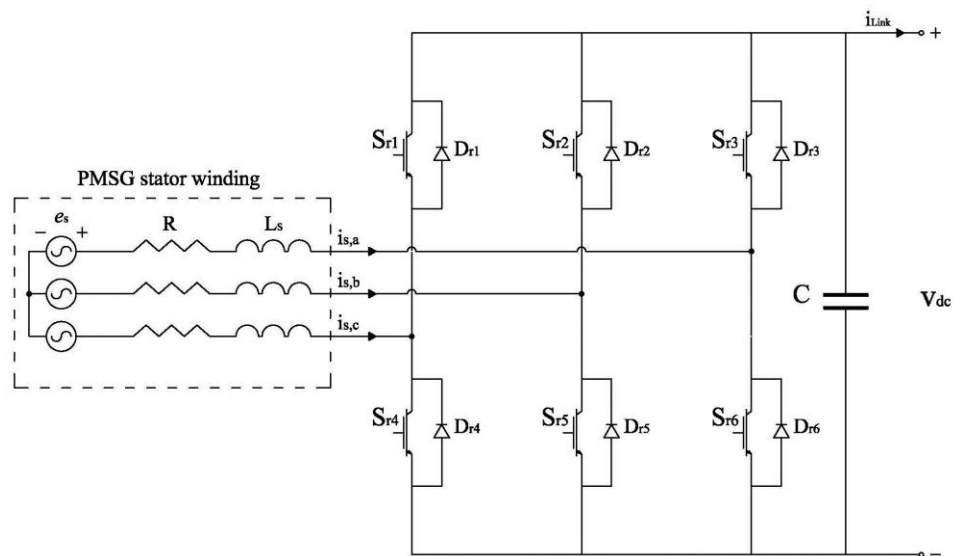


Fig. 3.3. Electrical schema of the three-phase PWM rectifier.

The dynamic model of three-phase PWM rectifier in synchronous reference frame (d,q) rotating at the angular frequency of the back-EMF of the PMSG is given by [31]:

$$\begin{cases} \frac{di_{sd}}{dt} = -\frac{R}{L_{sd}}i_{sd} + \hat{\omega}_s \frac{L_{sq}}{L_{sd}}i_{sq} - \frac{s_{rd}v_{dc}}{L_{sd}} + \frac{\hat{e}_{sd}}{L_{sd}} \\ \frac{di_{sq}}{dt} = -\hat{\omega}_s \frac{L_{sd}}{L_{sq}}i_{sd} - \frac{R}{L_{sq}}i_{sq} - \frac{s_{rq}v_{dc}}{L_{sq}} + \frac{\hat{e}_{sq}}{L_{sq}} \\ \frac{dv_{dc}}{dt} = \frac{s_{rd}i_{sd} + s_{rq}i_{sq}}{C} - \frac{i_{Link}}{C} \end{cases} \quad (3.3)$$

where \hat{e}_{sd} and \hat{e}_{sq} are the estimated d-q axis components of the back-EMF of the PMSG; $\hat{\omega}_s$ is the estimated electrical angular velocity of the PMSG rotor; i_{sd} , i_{sq} are the d-q axis components of the output phase currents of the PMSG; R is the resistance of the stator winding, L_{sd} and L_{sq} the self-inductance in d-q frame of the stator winding; C is the filter capacitor; v_{dc} is the output voltage on the DC-link and i_{Link} is the current on the DC-link; s_{rd} and s_{rq} are the d-q axis components of the switching pulses vector of the power electronic devices of the rectifier.

The system (3.3) with the equations (3.1- 3.2) are the starting point for the control strategy of the Stage 1.

3.1.3 Control Strategy of Stage 1

The control of the Stage 1, shown in Fig.3.1, is a Full Sliding Mode Control, expressed in a rotating reference frame synchronous with the electrical angular velocity of the PMSG.

The three-phase PWM rectifier control algorithm takes the following inputs:

- the desired q-axis component of the stator phase currents of the PMSG i_{sq}^* , related to the maximum power extracted from the thermodynamic sub-system by means of a suitable MPPT;
- the desired d-axis component of the stator phase currents of the PMSG i_{sd}^* , that is given in output by Integral Sliding Mode Controller (ISMC) controlling the error between the desired DC-link voltage and the actual one;
- the actual d-q components i_{sd} and i_{sq} of the stator phase currents of the PMSG.

The d-q axis components of the stator phase currents of the PMSG are computed via Park's transformation and then compared with the respective desired values i_{sd}^* and i_{sq}^* , after the d-q axis components current errors $x_{sd} = i_{sd} - i_{sd}^*$ and $x_{sq} = i_{sq} - i_{sq}^*$ are processed by the proposed Super-Twisting Integral Sliding Mode Controller (ST-ISMC1) to achieve the previous mentioned targets:

- 1.a) keeping of the DC-link voltage v_{dc} to a desired value v_{dc}^* ;
- 1.b) tracking of the maximum power point draw from the thermodynamic sub-system.

In the following the main components of the control loop of the Stage 1 are discussed.

3.1.3.1 Back-EMFs and rotor angle Sliding Mode Observer

The proposed sliding-mode observer estimates the back-EMF vector and the rotor angle starting by the measure of the PMSG phase currents and voltages [32].

The model of PMSG can be formulated in the α, β coordinate from equations (3.1), as follows:

$$\begin{cases} \frac{di_{s\alpha}}{dt} = -\frac{R}{L_s}i_{s\alpha} - \frac{1}{L_s}e_\alpha + \frac{1}{L_s}u_{s\alpha} \\ \frac{di_{s\beta}}{dt} = -\frac{R}{L_s}i_{s\beta} - \frac{1}{L_s}e_\beta + \frac{1}{L_s}u_{s\beta} \end{cases} \quad (3.4)$$

where $u_{s\alpha}$, $u_{s\beta}$ and $i_{s\alpha}$, $i_{s\beta}$ are the $\alpha - \beta$ axis components of the output phase voltages and current of the PMSG stator respectively, $L_s = L_{s\alpha} = L_{s\beta}$ is the self-inductance in $\alpha - \beta$ frame of the stator winding for isotropic machine with round rotor and the $\alpha - \beta$ axis components of the back-EMF e_α and e_β are expressed by:

$$\begin{cases} e_\alpha = -\omega_s \Psi \sin \theta_s \\ e_\beta = \omega_s \Psi \cos \theta_s \end{cases} \quad (3.5)$$

where θ_s is the electrical rotor angle of the PMSG.

Considering the back-EMF time derivative:

$$\begin{cases} \dot{e}_\alpha = -\omega_s e_\beta \\ \dot{e}_\beta = \omega_s e_\alpha \end{cases} \quad (3.6)$$

and the model (3.4), the state space equations of PMSG become:

$$\begin{bmatrix} \dot{i}_{s\alpha} \\ \dot{i}_{s\beta} \\ \dot{e}_\alpha \\ \dot{e}_\beta \end{bmatrix} = \mathbf{A} \cdot \begin{bmatrix} i_{s\alpha} \\ i_{s\beta} \\ e_\alpha \\ e_\beta \end{bmatrix} + \mathbf{B} \cdot \begin{bmatrix} u_{s\alpha} \\ u_{s\beta} \end{bmatrix} \quad (3.7)$$

where:

$$\mathbf{A} = \begin{bmatrix} -\frac{R}{L_s} & 0 & -\frac{1}{L_s} & 0 \\ 0 & -\frac{R}{L_s} & 0 & -\frac{1}{L_s} \\ 0 & 0 & 0 & -\omega_s \\ 0 & 0 & \omega_s & 0 \end{bmatrix}, \quad \mathbf{B} = \begin{bmatrix} \frac{1}{L_s} & 0 \\ 0 & \frac{1}{L_s} \\ 0 & 0 \\ 0 & 0 \end{bmatrix} \quad (3.8)$$

The model of the proposed Sliding Mode Observer is defined as:

$$\begin{bmatrix} \dot{\hat{i}}_{s\alpha} \\ \dot{\hat{i}}_{s\beta} \\ \dot{\hat{e}}_\alpha \\ \dot{\hat{e}}_\beta \end{bmatrix} = \hat{\mathbf{A}} \cdot \begin{bmatrix} \hat{i}_{s\alpha} \\ \hat{i}_{s\beta} \\ \hat{e}_\alpha \\ \hat{e}_\beta \end{bmatrix} + \mathbf{B} \cdot \begin{bmatrix} u_{s\alpha} \\ u_{s\beta} \end{bmatrix} + \mathbf{K} \cdot \text{sgn}(\boldsymbol{\sigma}) \quad (3.9)$$

where the apex “^” is related to the estimated values of the quantities shown in (3.7), while:

$$\hat{\mathbf{A}} = \begin{bmatrix} -\frac{R}{L_s} & 0 & -\frac{1}{L_s} & 0 \\ 0 & -\frac{R}{L_s} & 0 & -\frac{1}{L_s} \\ 0 & 0 & 0 & -\hat{\omega}_s \\ 0 & 0 & \hat{\omega}_s & 0 \end{bmatrix}, \quad \boldsymbol{\sigma} = \begin{bmatrix} error_\alpha \\ error_\beta \end{bmatrix} \quad (3.10)$$

The observer sliding surface $\boldsymbol{\sigma}$ is defined as a proportional action on the phase current errors in the $\alpha - \beta$ frame $error_\alpha = i_{s\alpha} - \hat{i}_{s\alpha}$ and $error_\beta = i_{s\beta} - \hat{i}_{s\beta}$.

The observer gain matrix \mathbf{K} is designed in order to guarantee the sliding conditions.

The electrical rotor angle is estimated as follows:

$$\hat{\theta}_s = \tan^{-1} \left(\frac{-\hat{e}_\alpha}{\hat{e}_\beta} \right) \quad (3.11)$$

Moreover the magnetic flux $\hat{\Psi}$ necessary for the evaluation of the reference component i_{sq}^* can be computed by means of the equation (3.2).

3.1.3.2 DC-link Voltage Integral Sliding Mode Controller

The control of the DC-link voltage is carried out by means of an Integral Sliding Mode Controller (ISMC), which gives in output the reference d-axis component i_{sd}^* of the stator phase currents of the PMSG (that is coincident with the phase current of the rectifier), as shown in Fig. 3.1.

Let us consider the following power balance condition for the three-phase PWM rectifier:

$$\frac{dv_{dc}}{dt} = \frac{s_{rd}i_{sd} + s_{rq}i_{sq}}{C} - \frac{i_{Link}}{C} \quad (3.12)$$

The equation (3.12) can be reformulated with respect to reference values of the of all its variables as follows:

$$\frac{dv_{dc}^*}{dt} = \frac{s_{rd}^*i_{sd}^* + s_{rq}^*i_{sq}^*}{C} - \frac{i_{Link}^*}{C} \quad (3.13)$$

The subtraction of (3.12) from (3.13) gives the following equation for the mismatch between the reference value and the actual one of the DC-link voltage:

$$\frac{d(v_{dc}^* - v_{dc})}{dt} = \frac{(s_{rd}^*i_{sd}^* + s_{rq}^*i_{sq}^* - s_{rd}i_{sd} - s_{rq}i_{sq})}{C} - \frac{(i_{Link}^* - i_{Link})}{C} \quad (3.14)$$

The control of DC-link voltage is implemented considering the reference d-axis component i_{sd}^* of the stator phase currents of the PMSG as control variable:

$$\dot{x} = bu + c \quad (3.15)$$

where:

$$b = \frac{1}{C} s_{rd}^* \quad , \quad c = \frac{(s_{rq}^* i_{sq}^* - s_{rd} i_{sd} - s_{rq} i_{sq})}{C} - \frac{(i_{Link}^* - i_{Link})}{C} \quad (3.16)$$

with $x = v_{dc}^* - v_{dc}$ is the mismatch between the reference value and the actual one of the DC-link voltage and $u = i_{sd}^*$ is the control variable.

Since the dynamic of the internal current control loop is faster than the external DC-link voltage control loop we can assume that the d-q axis components of the switching pulses vector of the power electronic devices of the rectifier have already reached their reference values ($s_{rd} = s_{rd}^*$ and $s_{rq} = s_{rq}^*$). Furthermore the reference value of the load current can be expressed as function of the reference d-q axis components i_{sd}^* and i_{sq}^* of the stator phase currents of the PMSG and of the reference value of the DC-link voltage v_{dc}^* as follows:

$$i_{Link}^* = \sqrt{i_{sd}^{*2} + i_{sq}^{*2}} - C \frac{dv_{dc}^*}{dt} \quad (3.17)$$

The integral sliding surface is defined as sum of a proportional and an integral action on the error x as follows:

$$s = \alpha x + \beta \int_0^t x dt \quad (3.18)$$

where α and β are positive constants.

Since (3.15) is linear equation, the equivalent control theory can be used; according to this theory the equivalent control u_{eq} can be calculated by equating the time-derivative of (3.18) to zero:

$$\dot{s} = \alpha \dot{x} + \beta x = 0 \Rightarrow u_{eq} = -\frac{(\alpha c + \beta x)}{\alpha b} \quad (3.19)$$

Substituting (3.19) into (3.15) the following motion equation for the mismatch x can be obtained:

$$\dot{x} + \frac{\beta}{\alpha} x = 0 \quad (3.20)$$

Note that (3.20) is invariant with respect to c which can be treated as perturbation term depending only by positive sliding constants α and β these are chosen in order to achieve a desired rate of convergence of the state trajectory to sliding surface $s = 0$.

It is necessary that control input is bounded in order to not exceed the available control resources u_0 as it is discussed in the previous sections. For this reason the control law can be reformulated as follows:

$$u = \begin{cases} u_{eq} & \text{for } |u_{eq}| \leq u_0 \\ u_0 \frac{u_{eq}}{|u_{eq}|} & \text{for } |u_{eq}| > u_0 \end{cases} \quad (3.21)$$

The control law (3.21) is able to guarantee the stability of the state trajectory as it has been discussed in Section 2.4.

3.1.3.3 Super-Twisting Integral Sliding Mode Controller 1

The current control of Stage 1 is achieved by Second-Order Super-Twisting Integral Sliding Mode Controller (ST-ISMC1) as shown in Fig. 3.1.

The control strategy is formulated in a rotating reference frame synchronous with the observed electrical angular velocity $\hat{\omega}_s$ of the back-EMF of the PMSG.

The inputs to the current control loop are:

- the desired q-axis component of the stator phase currents of the PMSG i_{sq}^* , related to the maximum power extracted from the thermodynamic sub-system by means of a suitable MPPT;
- the desired d-axis component of the stator phase currents of the PMSG i_{sd}^* , given as output of the ISMC controlling the error between the desired DC-link voltage and the actual one, as it has been discussed in previous sub-section 3.1.3.2.;
- the actual d-q components i_{sd} and i_{sq} of the stator phase currents of the PMSG.

According to the observed electrical rotor angle $\hat{\theta}_s$ that is estimated by sliding mode Observer as discussed in sub-section 3.1.3.1., the Park's transformation block of the stage 1 computes the d-q axis components i_{sd} and i_{sq} of the stator phase currents of the PMSG which are compared with the respective reference values i_{sd}^* and i_{sq}^* ; after the d-q axis components current errors $x_{sd} = i_{sd} - i_{sd}^*$ and $x_{sq} = i_{sq} - i_{sq}^*$ are processed by the proposed ST-ISMC1 according to ISMC discussed in previous sub-section in order to achieve the following targets:

- DC-link voltage control;
- tracking of the maximum power point drawn from the thermodynamic sub-system.

Considering the dynamic model (3.3) of the three-phase PWM rectifier, the following system for the d-q axis components current errors

$\mathbf{x}_s = [x_{sd} \ x_{sq}]^T = [i_{sd} - i_{sd}^* \ i_{sq} - i_{sq}^*]^T$ of the stator of PMSG is obtained:

$$\dot{\mathbf{x}}_s = \mathbf{A}\mathbf{x}_s + \mathbf{B}\mathbf{v}_r + \mathbf{C} \quad (3.22)$$

with:

$$\mathbf{A} = \begin{bmatrix} -\frac{R}{L_{sd}} & \hat{\omega}_s \frac{L_{sq}}{L_{sd}} \\ -\hat{\omega}_s \frac{L_{sd}}{L_{sq}} & -\frac{R}{L_{sq}} \end{bmatrix}; \mathbf{B} = \begin{bmatrix} -\frac{1}{L_{sd}} & 0 \\ 0 & -\frac{1}{L_{sq}} \end{bmatrix}; \quad (3.23)$$

$$\mathbf{C} = \begin{bmatrix} -\frac{\hat{e}_{sd}}{L_{sd}} - \frac{R}{L_{sd}} i_{sd}^* + \omega_s \frac{L_{sq}}{L_{sd}} i_{sq}^* & -\frac{\hat{e}_{sq}}{L_{sq}} - \hat{\omega}_s \frac{L_{sd}}{L_{sq}} i_{sd}^* - \frac{R}{L_{sq}} i_{sq}^* \end{bmatrix}$$

where $\mathbf{v}_r = [v_{rd} \ v_{rq}]^T = v_{dc} [s_{rd} \ s_{rq}]^T$ is rectifier input voltages vector that is treated as control vector and $\hat{\mathbf{e}}_s = [\hat{e}_{sd} \ \hat{e}_{sq}]^T$ is the estimated back-EMF vector of the PMSG that is obtained by Park' Transformation of observed back-EMF $\hat{\mathbf{e}}_{\alpha\beta} = [\hat{e}_\alpha \ \hat{e}_\beta]^T$ by mean of observed electrical rotor angle $\hat{\theta}_s$.

The equivalent discrete-time representation of (3.23) is defined as follows:

$$\mathbf{x}_{s,k+1} = \mathbf{A}_d \mathbf{x}_{s,k} + \mathbf{B}_d \mathbf{v}_{r,k} + \mathbf{C}_d \quad (3.24)$$

with (Euler approximation):

$$\mathbf{A}_d = \mathbf{I} + \mathbf{A}T_s; \mathbf{B}_d = \mathbf{B}T_s; \mathbf{C}_d = \mathbf{C}T_s \quad (3.25)$$

where T_s is the sampling period and for generic vector \mathbf{a} is:

$$\mathbf{a}_k = \mathbf{a}(kT_s) \quad (3.26)$$

The sliding surfaces in the ST-ISMC1 of the Stage 1 are defined as the sum of a proportional and an integral action on the current errors:

$$\begin{aligned}
s_{1d,k} &= \alpha_{1d} \cdot x_{sd,k} + \beta_{1d} \sum_{\rho=0}^{k-1} x_{sd,\rho} \\
s_{1q,k} &= \alpha_{1q} \cdot x_{sq,k} + \beta_{1q} \sum_{\rho=0}^{k-1} x_{sq,\rho}
\end{aligned} \tag{3.27}$$

where $\mathbf{s}_1 = [s_{1d} \quad s_{1q}]^T = \mathbf{0}$ is the sliding manifold of the ST-ISMC1, the α_{1d} , α_{1q} , β_{1d} , β_{1q} are positive gains of sliding surface in according with the desired dynamic state trajectories behavior.

According to Super-Twisting algorithm discussed in sub-section 2.6.1.2., the reaching law can be expressed as follows:

$$\begin{cases}
s_{1d,k+1} = -k_{11} \sum_{\rho=0}^{k-1} \text{sgn}(s_{1d,\rho}) - k_{12} |s_{1d,k}|^{0.5} \text{sgn}(s_{1d,k}) = v_{rd,k}^* \\
s_{1q,k+1} = -k_{21} \sum_{\rho=0}^{k-1} \text{sgn}(s_{1q,\rho}) - k_{22} |s_{1q,k}|^{0.5} \text{sgn}(s_{1q,k}) = v_{rq,k}^*
\end{cases} \tag{3.28}$$

where $\text{sgn}(s_{1d,k})$ and $\text{sgn}(s_{1q,k})$ represent the signum function of $s_{1d,k}$ and $s_{1q,k}$ respectively, while k_{11} , k_{12} , k_{21} , k_{22} represent control parameters determined by Lyapunov stability analysis for the convergence velocity and steady-state error.

Considering the corresponding continuous-time representation of (3.28):

$$\begin{cases}
\frac{ds_{1d}}{dt} = -k_{11} \int \text{sgn}(s_{1d}) dt - k_{12} |s_{1d}|^{0.5} \text{sgn}(s_{1d}) \\
\frac{ds_{1q}}{dt} = -k_{21} \int \text{sgn}(s_{1q}) dt - k_{22} |s_{1q}|^{0.5} \text{sgn}(s_{1q})
\end{cases} \tag{3.29}$$

A Lyapunov function candidate can be defined as follows:

$$\mathbf{V} = \begin{cases}
\frac{ds_{1d}}{dt} = 0.5 \left(k_{11} \int \text{sgn}(s_{1d}) dt \right)^2 + k_{12} \int_0^{s_{1d}} \text{sgn}(z) dz \\
\frac{ds_{1q}}{dt} = 0.5 \left(k_{21} \int \text{sgn}(s_{1q}) dt \right)^2 + k_{22} \int_0^{s_{1q}} \text{sgn}(z) dz
\end{cases} \tag{3.30}$$

that is a positive definite function. The time-derivative of (3.29) yields:

$$\dot{\mathbf{V}} = \frac{d\mathbf{V}}{dt} = - \begin{bmatrix} k_{11}k_{12} |s_{1d}|^{0.5} \\ k_{21}k_{22} |s_{1q}|^{0.5} \end{bmatrix} \leq 0 \quad (3.31)$$

By the equation (3.31) can be noted that the time-derivative of the Lyapunov function \mathbf{V} is definitely negative. So the switching function s_1 and its first time-derivative \dot{s}_1 tend to zero according to that has been discussed in subsection 2.1.1. Therefore this proves that the control system is asymptotically stable; this results also by (3.28) in which we can note that the control actions $v_{rd,k}^*$ and $v_{rq,k}^*$ become weaker and weaker as s_1 approach to 0 making the control enough smooth.

3.2 Stage 2: Components Modeling and Control Strategy

The main component of Stage 1 is the three-phase soft-switched Voltage Source Inverter (VSI) that consist of Quasi-Resonant branch and a three-phase PWM inverter as shown in Fig. 3.1. This converter is connected too grid utility by means of three-phase step-up transformer. The dynamic models of the mentioned power electric components and the control strategy of Stage 1 will be explained in this section.

3.2.1 Three-phase Soft-Switched Voltage Source Inverter (VSI)

The three-phase soft-switched Voltage Source Inverter (VSI) is the most important component of the Double Stage AC-AC Power Converter in order to maximize the efficiency of energy conversion. This converter has high performance due to the presence of Quasi-Resonant branch.

Although there are many configurations of soft-switching inverter in the literature, the configuration scheme shown in Fig.3.4. has been adopted in order to obtain a very inexpensive and simple structure, but at the same time a robust converter.

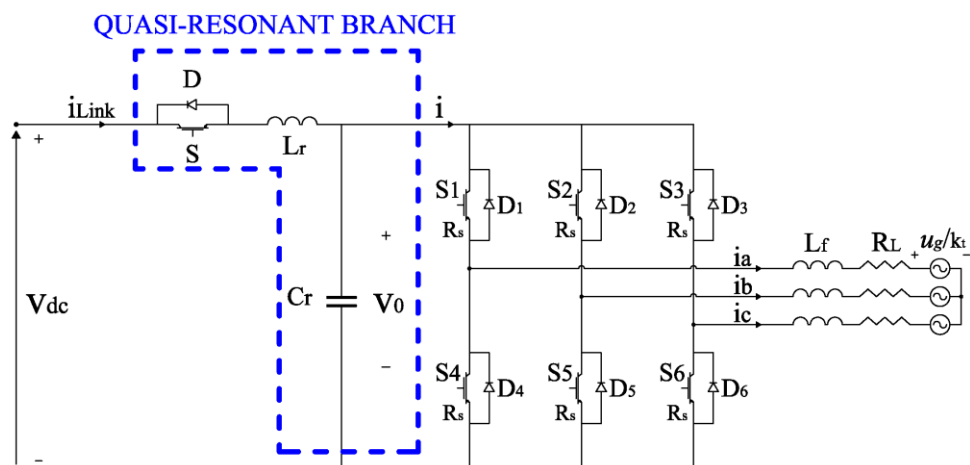


Fig. 3.4. Electrical scheme of the there-phase Quasi-Resonant VSI.

Indeed the soft-switched VSI differs from a traditional three-phase VSI only for the introduction of the quasi-resonant branch, that consists of a single electronic switch component as shown in Fig. 3.4.

The dynamic model of PWM VSI in synchronous reference frame (d,q) rotating at the angular frequency ω of the grid voltages is defined as

$$\left\{ \begin{array}{l} \frac{di_d}{dt} = -\frac{(R_L + R_s)}{L_f} i_d - \omega i_q + \frac{1}{L_f} s_d v_0 - \frac{1}{L_f} \frac{u_{g,d}}{k_t} \\ \frac{di_q}{dt} = \omega i_d - \frac{(R_L + R_s)}{L_f} i_q + \frac{1}{L_f} s_q v_0 - \frac{1}{L_f} \frac{u_{g,q}}{k_t} \\ \frac{dv_0}{dt} = \frac{i_{Link}}{C_r} - \frac{s_d i_d + s_q i_q}{C_r} \\ \frac{di_{Link}}{dt} = \frac{v_{dc} - v_0}{L_r} \end{array} \right. \quad (3.32)$$

where: i_d and i_q are the d-q axis components of the output phase currents of VSI; v_0 is the resonant capacitor voltage; v_{dc} is the output voltage on the DC-link; i_{Link} is the current on the DC-link; s_d and s_q are the d-q axis components of the switching pulses vector of the VSI switches, $u_{g,d}$ and $u_{g,q}$ are the d-q axis components of the grid voltages; k_t is the transformer ratio; R_s is the VSI components' ESR, R_L and L_f are the phase inductance and resistance of the output filter to VSI, respectively; L_r and C_r are the inductance and capacitor of the quasi-resonant branch, respectively.

The main advantages of use soft-switched VSI are: high switching frequencies of VSI, therefore improved quality of output waveforms; high efficiency (minimum equal to 96%); reduced dimensions of the output filters. However, there is the voltage overshoot problem (the voltage of electronic switch component can reach twice the voltage on the DC-link). Thus the use of grid-connected step-up tree-phase transformer is necessary for operate with low voltage on the DC-link.

In the following the Quasi-Resonant phenomenon will be explained.

The equivalent single-phase scheme of soft-switched VSI is shown in Fig. 3.5.

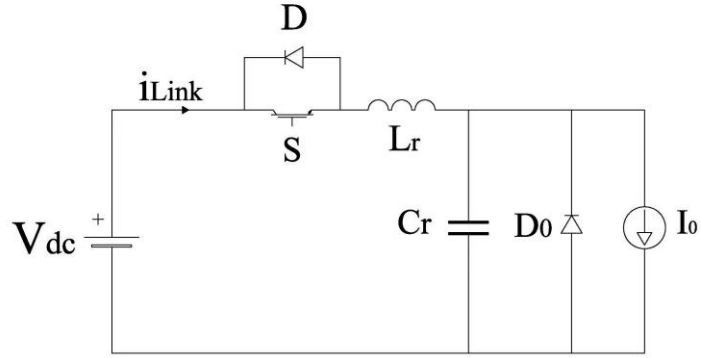


Fig. 3.5. Equivalent single-phase scheme of three-phase soft-switched VSI

where VSI is considered equivalent to an ideal current source and the DC-link voltage is considered constant with respect to the time.

The DC-link current i_{Link} and the voltage v_0 at the terminals of the resonant capacitor C_r as time functions are depicted in the next figure:

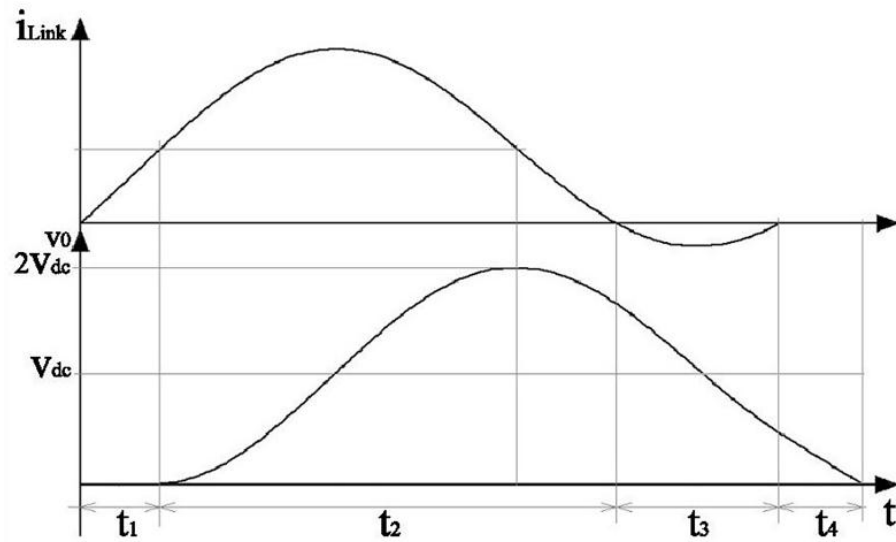


Fig. 3.6. DC-link current i_{Link} and resonant capacitor voltage v_0 as time functions

It is assumed that the diode D_0 is conducting the full current I_0 and the electronic switch component is turn-on at initial time instant $t=0$. The behavior of the DC-link current i_{Link} is governed by the following equation in the first time interval $[0, t_1]$:

$$i_{Link}(t) = \frac{V_{dc}}{L_r} t \quad \text{for } 0 \leq t \leq t_1 \quad (3.33)$$

Therefore the DC-link current i_{Link} increase linearly with respect to the time until reaching the value I_0 at instant time t_1 as it can be noted by (3.33). Thus the instant time t_1 may be calculated by:

$$i_{Link}(t) = I_0 \Rightarrow t_1 = \frac{L_r I_0}{V_{dc}} \quad (3.34)$$

After the time interval t_1 the diode D_0 is turn-off and so starting the resonant phenomenon. When the electronic switch component S of the quasi-resonant branch conducts, the dynamic of resonant capacitor voltage v_0 can be expressed as:

$$L_r C_r \frac{d^2 v_0}{dt^2} + v_0 = V_{dc} \quad \text{for } t_1 < t \leq t_3 \quad (3.35)$$

with the following initial conditions:

$$\begin{cases} i_c(0) = 0 \\ v_c(0) = 0 \end{cases} \quad (3.36)$$

The expression of resonant capacitor voltage and DC-link current are:

$$\begin{aligned} v_0(t) &= V_{dc} [1 - \cos(\omega_0 t)] \\ i_{Link}(t) &= i_c + I_0 = \frac{V_{dc}}{Z_0} \sin(\omega_0 t) + I_0 \end{aligned} \quad (3.37)$$

where $\omega_0 = \frac{1}{\sqrt{L_r C_r}}$, $Z_0 = \sqrt{\frac{L_r}{C_r}}$ and I_0 is coincident with the average load current value.

After the time interval $t_1 + t_2$, the diode D_1 turn on and the component S can be switch off with current practically equal to zero due to the DC-link current became negative. Therefore the switching losses of quasi-resonant branch are very low because the component S can be turned-off with zero current value (ZCS) and it will be characterized only diode voltage that is very low in direct conduction.

The expression of current on the DC-Link (3.37) shows that the following inequality must be satisfied so that the current i_{Link} becomes negative:

$$Z_0 I_0 < V_{dc} \quad (3.38)$$

Equation (3.38) is the starting point for quasi-resonant branch design that will be discussed in the later sections.

According to (3.38) the DC-link current reaches the zero value at instant time:

$$t_1 + t_2 = \frac{\pi}{\omega_0} - \frac{1}{\omega_0} \arcsin\left(-\frac{Z_0 I_0}{V_{dc}}\right) \quad (3.39)$$

At the time interval $t_1 + t_2 + t_3$ the DC-link current reaches the zero value again:

$$i_{Link}(t_1 + t_2 + t_3) = 0 \Rightarrow t_3 = \frac{\pi}{\omega_0} - (t_1 + t_2) \quad (3.40)$$

$$v_0(t_1 + t_2 + t_3) = V_{dc}(1 - \cos \omega_0 t_3) = V_3 \quad (3.41)$$

Therefore the resonant capacitor discharges linearly during the interval time t_4 according to the following equation:

$$v_0(t) = V_3 - \frac{I_0}{C_r} t \quad (3.42)$$

and the last time interval t_4 is given by:

$$v_0(t_1 + t_2 + t_3 + t_4) = 0 \Rightarrow t_4 = \frac{V_3 C_r}{I_0} - (t_1 + t_2 + t_3) \quad (3.43)$$

The resonant period T_r is expressed as:

$$T_r = \sum_1^4 t_i \quad (3.44)$$

After the resonant period T_r the resonant capacitor voltage v_0 shows down to zero until the turn-on of the switch S. Thus the switches of the VSI can be switched with zero voltage value (ZVS) after the resonant period T_r .

As a result the soft-switched VSI is a zero voltage and zero current switching converter if the switching frequency of the soft-switched VSI is chosen as integer multiple of resonant frequency defined as inverse of the resonant period T_r .

3.2.2 Control Strategy of Stage 2

The control strategy of Stage 2 is formulated in a rotating reference frame synchronous with the electrical angular velocity ω of the grid utility vector voltages, as shown in Fig. 3.1, in order to achieve the following targets depending on the balancing grid utility conditions:

- control instantaneous active and reactive power values on the grid utility, in the case of balanced conditions of the grid utility;
- current harmonic rejection, in the case of unbalanced conditions the grid utility.

The Stage 2 is consists of a Phase Locked Loop (PLL) for the synchronization on d-q reference rotating frame having the same angular frequency as the grid voltages and two Park's transformation blocks for the estimation of the d-q axis components of the grid voltages ($u_{g,d}, u_{g,q}$) and currents (i_{Ld}, i_{Lq}), the three-phase soft-switched Voltage Source Inverter and a grid-connected three-phase step-up transformer as shown in Fig. 3.1.

The proposed control of the Stage 2 is a High-Order Super-Twisting Integral Sliding Mode Control (ST-ISMC2), expressed in a rotating reference frame synchronous with the electrical angular velocity of the utility grid.

The control strategy is formulated in a rotating reference frame synchronous with the electrical angular velocity of the utility grid as it has been mentioned above.

The d-q axis reference components of grid currents i_{Ld}^* and i_{Lq}^* are computed according to the apparent power given by the PMSG and their values depend on the following two grid utility conditions:

- in the balanced grid utility condition i_{Ld}^* and i_{Lq}^* are computed from the desired values of the instantaneous active and reactive power, respectively;
- in the unbalanced grid utility condition i_{Ld}^* and i_{Lq}^* are computed from the desired value of the grid currents vector.

These reference currents are compared with the respective actual values and the related errors $x_d = i_{Ld} - i_{Ld}^*$ and $x_q = i_{Lq} - i_{Lq}^*$ are used to define the sliding surfaces in the Super-Twisting Integral Sliding Mode Controller (ST-ISMC2) as more explained in the following subsection 3.2.2.2.

3.2.2.1 Calculation of d-q axis reference components of grid-utility currents

Under balanced grid utility condition the d-q axis reference components of the grid utility currents i_{Ld}^* and i_{Lq}^* are computed from the desired values of the instantaneous active and reactive power, respectively. In this subsection a demonstration of this result will be given.

Considering the grid utility a three-phase sinusoidal system, the voltages space vector and the currents space vector can be defined as follows:

$$\begin{aligned} \mathbf{u}_g &= \frac{2}{3} \left(u_{g,a} + u_{g,b} e^{j\frac{2\pi}{3}} + u_{g,c} e^{j\frac{4\pi}{3}} \right) = u_g(t) e^{j\theta(t)} \\ \mathbf{i}_L &= \frac{2}{3} \left(i_{L,a} + i_{L,b} e^{j\frac{2\pi}{3}} + i_{L,c} e^{j\frac{4\pi}{3}} \right) = i_L(t) e^{j(\theta(t) - \varphi(t))} \end{aligned} \quad (3.45)$$

where $u_{g,a}$, $u_{g,b}$, $u_{g,c}$ are the phase voltages instantaneous values of the grid utility, $i_{L,a}$, $i_{L,b}$, $i_{L,c}$ are the phase currents instantaneous values of the grid utility and $\varphi(t)$ is the displacement phase between \mathbf{u}_g and \mathbf{i}_L as shown in Fig.3.7.

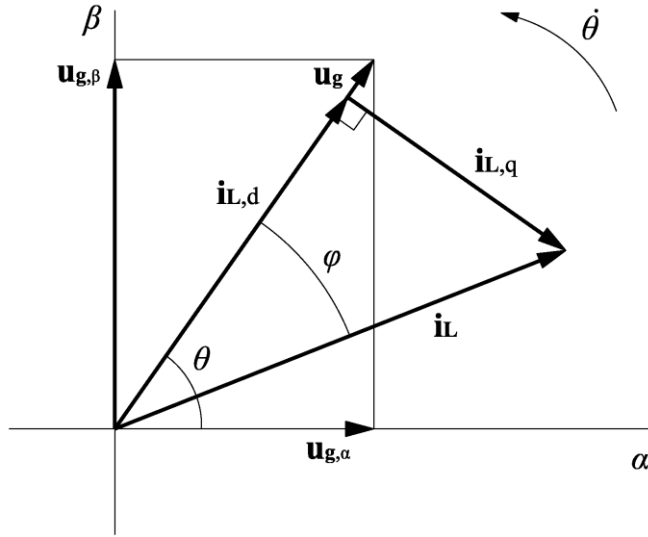


Fig. 3.7. Grid voltages and currents space vectors in the $\alpha - \beta$ frame

Under balanced grid utility conditions the amplitude of the space vectors (3.45) and the displacement phase $\varphi(t)$ remain constants with respect to time.

The space vectors (3.45) can be reformulated by multiplying (3.45) for $e^{-j\theta(t)}$ as follows:

$$\begin{aligned} \mathbf{u}_g &= u_g(t) \\ \mathbf{i}_L &= i_L(t)e^{-j\varphi(t)} \end{aligned} \quad (3.46)$$

So the space vectors defined by (3.46) are referred to rotating reference frame synchronous with the constant electrical angular velocity $\omega = \frac{d\theta(t)}{dt}$ of the grid utility voltages space vector as shown in Fig. 3.8. This change of reference frame is equivalent to Park's transformation applied to space vectors (3.45) for the estimation of the d-q axis components of the grid voltages ($u_{g,d}, u_{g,q}$) and currents ($i_{L,d}, i_{L,q}$).

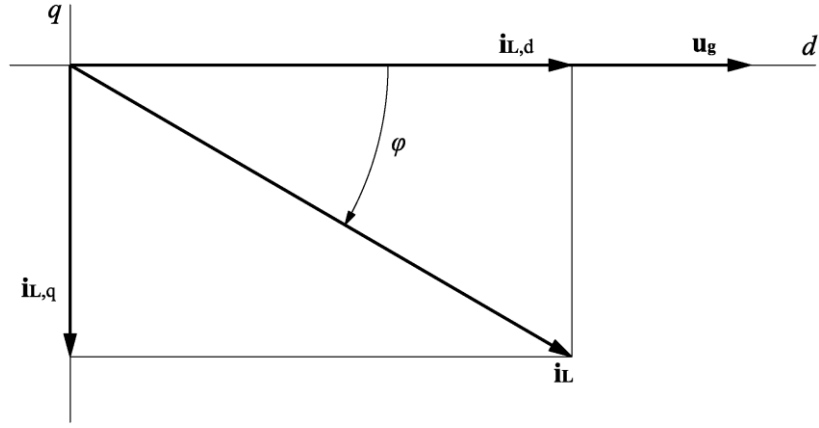


Fig. 3.8. Grid voltages and currents space vectors in the d-q frame synchronous with the constant electrical angular velocity ω of the grid voltages

Therefore the currents space vector \mathbf{i}_L into (3.46) can be defined as sum of two terms:

$$\mathbf{i}_L = i_{Ld} + j i_{Lq} \quad (3.47)$$

where $i_{Ld} = i_L \cos(\varphi(t))$ is called “instantaneous active current” and $i_{Lq} = j \cdot i_L \sin(\varphi(t))$ is called “instantaneous reactive current”, while the voltages space vector under balanced grid-utility conditions can be defined as follows:

$$\mathbf{u}_g = u_g = u_{g,d} \quad (3.48)$$

as it can be noted by Fig 3.8.

According to equations (3.47) and (3.48) the Park’s instantaneous complex power of the three-phase system is defined as follows:

$$\begin{aligned} S_p(t) &= \frac{3}{2} \mathbf{u}_g \bar{\mathbf{i}}_L = \frac{3}{2} u_g(t) i_L(t) e^{j\varphi(t)} = \\ &= \frac{3}{2} [u_{g,d}(t) i_{Ld}(t) + j \cdot u_{g,d}(t) i_{Lq}(t)] = P(t) + jQ(t) \end{aligned} \quad (3.49)$$

where $P(t)$ and $Q(t)$ are the instantaneous active and reactive power, respectively.

Therefore in the case of balanced grid utility condition, the d-q reference grid currents $i_{L,d}^*$ and $i_{L,q}^*$ are computed according to (3.49), in order to generate the desired instantaneous active P^* and reactive power Q^* values on the grid utility:

$$\begin{cases} P^* = \frac{3}{2} u_{g,d} i_{L,d}^* \\ Q^* = \frac{3}{2} u_{g,d} i_{L,q}^* \end{cases} \quad (3.50)$$

where $S_p = P^* + jQ^*$ is set equal to apparent power in output from PMSG.

Conversely in the case of unbalanced grid utility conditions, the d-q reference grid currents $i_{L,d}^*$ and $i_{L,q}^*$ are computed from the desired value of the grid currents vector; in this case the proposed soft-switched VSI can be used as a system of current harmonic rejection.

3.2.2.2 Super-Twisting Integral Sliding Mode Controller 2

Similar to control strategy of Stage 1, the main component of the current control loop of Stage 2 is Second-Order Super-Twisting Integral Sliding Mode Controller (ST-ISMC2) as shown in Fig. 3.1 in order to achieve the following two targets:

- 1) control of instantaneous active and reactive power values on the grid utility, in the case of balanced conditions of the grid utility;
- 2) current harmonic rejection, in the case of unbalanced conditions the grid utility.

The control strategy of Stage 2 is formulated in a rotating reference frame synchronous with the electrical angular velocity ω of the grid utility vector voltages by means of a suitable PLL.

According to two targets mentioned above the inputs reference of the control loop are computed as follows:

- for achieve the target (1) i_{Ld}^* and i_{Lq}^* are computed from the desired values of the instantaneous active and reactive power, respectively, according to the apparent power given by PMSG (in the balanced grid utility condition);
- for achieve the target (2) i_{Ld}^* and i_{Lq}^* are computed from the desired value of the grid currents vector (in the unbalanced grid utility condition).

On the basis of the electrical angle θ of grid utility voltages vector given in output by PLL, the Park's transformations block of the Stage 2 computes the d-q axis components i_{Ld} and i_{Lq} of grid utility phase currents which are compared with the respective reference values i_{Ld}^* and i_{Lq}^* in order to obtain the d-q axis components current errors $x_d = i_{Ld} - i_{Ld}^*$ and $x_q = i_{Lq} - i_{Lq}^*$. These current errors are treated by ST-ISMC2 in order to achieve the goals 1) or 2) depending on the balancing grid utility conditions.

Starting to dynamic model of the soft-switched VSI (3.32), this can be reformulated in terms of current errors as follows:

$$\begin{cases} \frac{dx_d}{dt} = -\frac{(R_L + R_s)}{L_f} x_d - \omega x_q + \frac{v_d}{L_f} - \frac{u_{g,d}}{L_f} \\ \frac{dx_q}{dt} = -\frac{(R_L + R_s)}{L_f} x_q + \omega x_d + \frac{v_q}{L_f} - \frac{u_{g,q}}{L_f} \end{cases} \quad (3.51)$$

that in matrix form becomes:

$$\dot{\mathbf{x}} = \mathbf{Ax} + \mathbf{Bv} + \mathbf{C} \quad (3.52)$$

with:

$$\mathbf{A} = \begin{bmatrix} -\frac{(R_L + R_s)}{L_f} & \omega \\ -\omega & -\frac{(R_L + R_s)}{L_f} \end{bmatrix}; \mathbf{B} = \begin{bmatrix} -\frac{1}{L_f} & 0 \\ 0 & -\frac{1}{L_f} \end{bmatrix};$$

$$\mathbf{C} = \begin{bmatrix} -\frac{u_{g,d}}{k_t L_f} - \frac{(R_L + R_s)}{L_f} i_{Ld}^* + \omega i_{Lq}^* & -\frac{u_{g,q}}{k_t L_f} - \omega i_{Ld}^* - \frac{(R_L + R_s)}{L_f} i_{Lq}^* \end{bmatrix}$$
(3.53)

where $\mathbf{v} = [v_d \ v_q]^T = v_0 [s_d \ s_q]^T$ is soft-switched VSI output voltages vector that is treated as control vector, $u_{g,d}$ and $u_{g,q}$ are the d-q axis components of the grid voltages.

The equivalent discrete-time representation of (3.52) is defined as follows:

$$\mathbf{x}_{k+1} = \mathbf{A}_d \mathbf{x}_k + \mathbf{B}_d \mathbf{v}_k + \mathbf{C}_d$$
(3.54)

with (Euler approximation):

$$\mathbf{A}_d = \mathbf{I} + \mathbf{A}T_s; \mathbf{B}_d = \mathbf{B}T_s; \mathbf{C}_d = \mathbf{C}T_s$$
(3.55)

where T_s is the sampling period and for generic vector \mathbf{a} is:

$$\mathbf{a}_k = \mathbf{a}(kT_s)$$
(3.56)

Similar to ST-ISMCI, the sliding surfaces of ST-ISMCI are defined as the sum of a proportional and an integral action on the current errors:

$$s_{2d,k} = \alpha_{2d} \cdot x_{d,k} + \beta_{2d} \sum_{\rho=0}^{k-1} x_{d,\rho}$$

$$s_{2q,k} = \alpha_{2q} \cdot x_{q,k} + \beta_{2q} \sum_{\rho=0}^{k-1} x_{q,\rho}$$
(3.57)

where $\mathbf{s}_2 = [s_{2d} \ s_{2q}]^T$ is the switching function of the ST-ISMCI, the α_{2d} , α_{2q} , β_{2d} , β_{2q} are positive gains of sliding surface.

According to Super-Twisting algorithm discussed in sub-section 2.6.1.2., the same reaching law of ST-SMC1 can be chosen:

$$\begin{cases} s_{2d,k+1} = -k_{11} \sum_{\rho=0}^{k-1} \text{sgn}(s_{2d,\rho}) - k_{12} |s_{2d,k}|^{0.5} \text{sgn}(s_{2d,k}) = v_{d,k}^* \\ s_{2q,k+1} = -k_{21} \sum_{\rho=0}^{k-1} \text{sgn}(s_{2q,\rho}) - k_{22} |s_{2q,k}|^{0.5} \text{sgn}(s_{2q,k}) = v_{q,k}^* \end{cases} \quad (3.58)$$

where $\text{sgn}(s_{2d,k})$ and $\text{sgn}(s_{2q,k})$ represent the sign function of $s_{2d,k}$ and $s_{2q,k}$ respectively, k_{11} , k_{12} , k_{21} , k_{22} represent control parameters determined by Lyapunov stability analysis for the convergence velocity and steady-state error as similar to it has been discussed for ST-ISMC1 and the control actions $v_{d,k}^*$ and $v_{q,k}^*$ become weaker and weaker as s_2 approach to 0 making the control enough smooth.

The corresponding continuous-time representation of (3.58):

$$\begin{cases} \frac{ds_{2d}}{dt} = -k_{11} \int \text{sgn}(s_{2d}) dt - k_{12} |s_{2d}|^{0.5} \text{sgn}(s_{2d}) \\ \frac{ds_{2q}}{dt} = -k_{21} \int \text{sgn}(s_{2q}) dt - k_{22} |s_{2q}|^{0.5} \text{sgn}(s_{2q}) \end{cases} \quad (3.59)$$

The same positive definite Lyapunov function of subsection 3.1.3.3. can be considered:

$$\mathbf{V} = \begin{cases} \frac{ds_{1d}}{dt} = 0.5 \left(k_{11} \int \text{sgn}(s_{1d}) dt \right)^2 + k_{12} \int_0^{s_{1d}} \text{sgn}(z) dz \\ \frac{ds_{1q}}{dt} = 0.5 \left(k_{21} \int \text{sgn}(s_{1q}) dt \right)^2 + k_{22} \int_0^{s_{1q}} \text{sgn}(z) dz \end{cases} \quad (3.60)$$

Thus the time-derivative of the Lyapunov function \mathbf{V} is definitely negative as follows:

$$\dot{\mathbf{V}} = \frac{d\mathbf{V}}{dt} = - \begin{bmatrix} k_{11} k_{12} |s_{1d}|^{0.5} \\ k_{21} k_{22} |s_{1q}|^{0.5} \end{bmatrix} \leq 0 \quad (3.61)$$

As a result the switching function s_2 and its first time-derivative \dot{s}_2 tend to zero according to that has been discussed in sub-section 2.1.1., so the control system is asymptotically stable as the case of ST-ISMC1.

3.3 Analysis and Design of Electrical Subsystem

The main innovative components of the considered electrical subsystem are the PMSG and Quasi Resonant branch. In the following the principal design equations and parameters for these components will be discussed.

3.3.1 Permanent Magnet Synchronous Generator design

The PMSG design is performed according to the following assumptions:

- the considered machine is three-phase;
- the iron saturation and the effect of the stator gaps in the air gap flux density calculation have been neglected.

Geometrical parameters of the machine

The Fig. 3.9 shows the main geometrical parameters of the generator.

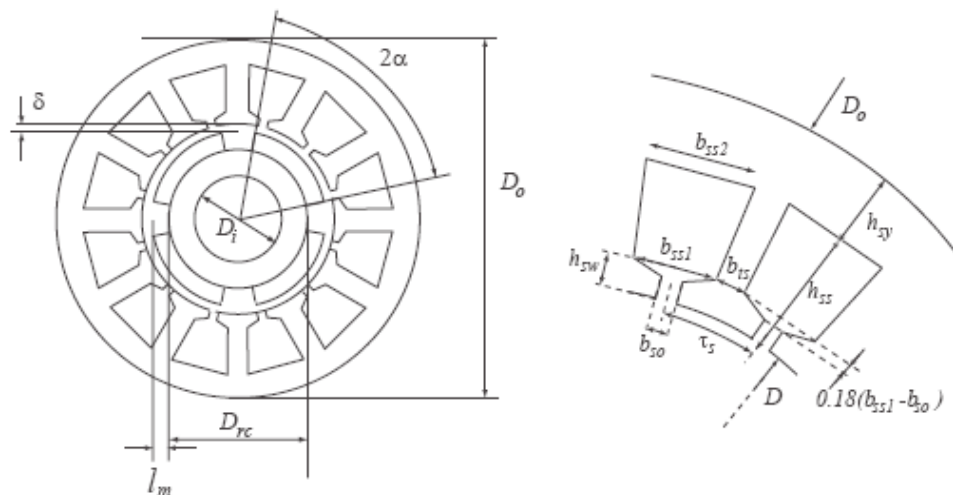


Fig. 3.9. Geometrical parameters of the generator.

The geometrical parametric equations of PMSG are given by:

$$D = D_{rc} + 2l_m + 2\delta \quad (3.62) \quad h_{sy} = \frac{1}{2}(D_o - D - 2h_{ss}) \quad (3.63)$$

$$\tau_s = \pi \frac{D}{Q_s} \quad (3.64) \quad b_{ss2} = \pi \frac{D + 2h_{ss}}{Q_s} - b_{ts} \quad (3.65)$$

$$b_{ss1} = \pi \frac{D + 2h_{sw}}{Q_s} - b_{ts} \quad (3.66) \quad k_{open} = b_{so} / b_{ss1} \quad (3.67)$$

where Q_s is the number of the stator slots, k_{open} is defined as ratio between the opening of stator slot b_{so} and the width of stator slot b_{ss1} under consideration that the width of stator tooth b_{ts} to be constant. Into equations (3.65) and (3.66) the arcs b_{ss1} , b_{ss2} and b_{ts} can be approximated by segments because the internal stator diameter D is much longer than the step of stator slot τ_s .

The area of a stator slot is defined by the next equation:

$$A_{sl} = \frac{1}{2}(b_{ss1} + b_{ss2})(h_{ss} - h_{sw}) \quad (3.68)$$

where the height of the stator tooth has been fixed to $h_{sw} = 0,18(b_{ss1} - b_{so})$.

Magnetic flux density in the air-gap under open circuit condition

According to models that are discussed into [33]-[34] the magnetic flux density can be estimated as follows.

The reference frame is chosen coincident with PM magnetic axis in order to compute the angular position of magnetic flux of the phase winding as shown in Fig. 3.10 in the case of the number of stator slot for pole and for phase is $q = 2$.

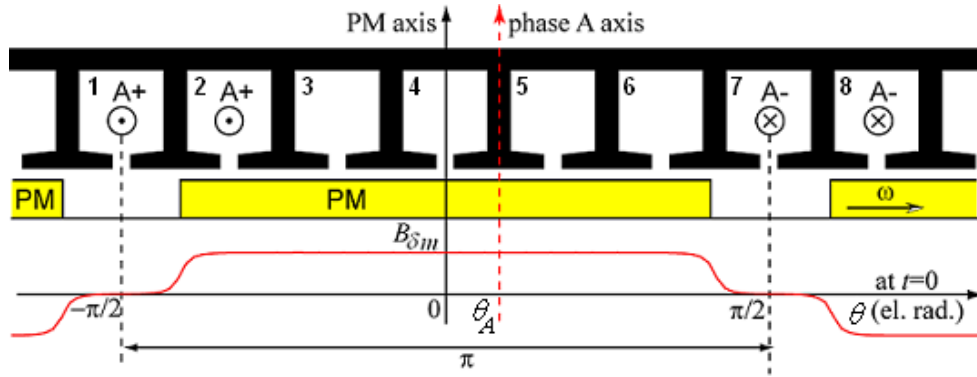


Fig. 3.10. Flux magnetic density in air-gap under open circuit condition of a PMSG with $q = 2$

Therefore the displacement phase between the axis of the magnetic flux of the phase winding A and the reference frame is θ_A at initial instant $t = 0$.

Thus the magnetic flux density in the air-gap under open circuit condition of PMSG is given by:

$$B_{\delta m}(\theta) = \sum_{h(1,3,5\dots)}^{\infty} B_{mh} \cos(h\theta - h\omega t) \quad (3.69)$$

where ω is the electrical angular velocity of the rotor, B_{mh} is the amplitude of the h -th harmonic component of the magnetic flux density $B_{\delta m}$ according to [33]-[34].

Winding factor

The winding factor is calculated according to [35] in order to estimate the distribution of winding in the stator slots. Assuming note the disposition of the coils in the slots a auxiliary vector \mathbf{S} is introduced for describe the scheme of the phase A. this vector consist of the slot numbers with sign +/- depending on the current flow is incoming or outgoing from the slot respectively. So the vector $\mathbf{S} = [1 \ 2 \ -7 \ -8]$ is corresponding to the scheme of the distributed phase winding A, as shown in Fig. 3.10.

For the i -th lateral coil of the phase A, the h -th harmonic component of the corresponding back-EMF is given by:

$$\vec{E}_{ih} = \text{sign}(\mathbf{S}(i)) e^{j \frac{h\pi p}{Q_s} |\mathbf{S}(i)-1|} \quad (3.70)$$

The amplitude of the h -th harmonic component of the winding factor is defined as follows:

$$k_{wh} = \frac{1}{n_l Q_s / 3} \left| \sum_{i=1}^{n_l Q_s / 3} \vec{E}_{ih} \right| \quad (3.71)$$

where n_l is the number of layers of the winding.

The angular phase of the h -th harmonic component of the winding factor is given by:

$$\alpha_{k_{wh}} = \arg \left(\sum_{i=1}^{n_l Q_s / 3} \vec{E}_{ih} \right) \quad (3.72)$$

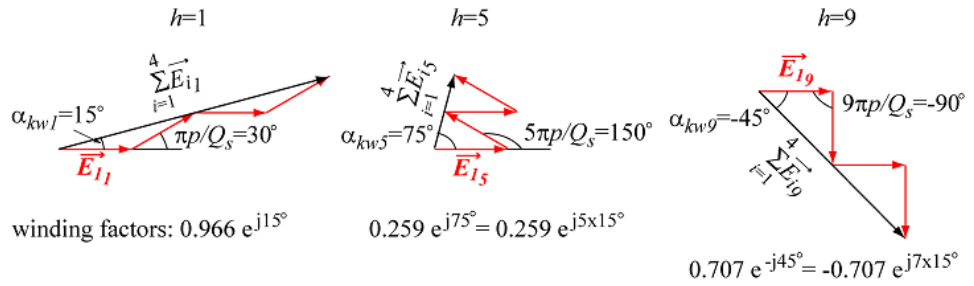


Fig. 3.11. Back-EMF phasors for the phase A winding

The winding factor values of Fig. 3.11 can be compared to those obtained via closed form expression. In this case the winding factor is coincident to the distribution factor that is given by:

$$k_{\text{dist}h} = \frac{\sin \frac{h\pi}{6}}{q \sin \frac{h\pi}{6q}} \quad (3.73)$$

For $h=1$, $k_{dist1} = 0,966$; for $h=5$, $k_{dist5} = 0,259$; for $h=9$, $k_{dist9} = -0,707$ in according with the winding factor values calculated by means of the above phasorial method (Fig. 3.11).

Machine inductances

Regarding the electrical parameters of PMSG, the self-inductance L_a is defined as sum of the leakage inductance of slot L_{leak} , the magnetization inductance L_{magn} and the end winding inductance L_{ew} .

The leakage inductance of slot L_{leak} is calculated according to [36].

In order to calculate the magnetizing inductance, it necessary to estimate the magnetic flux density of armature reaction due to the current i_a of the phase A that is given by [37]:

$$B_{wind.i_a} = \sum_{h=1}^{\infty} \frac{2q\mu_0}{\pi\delta} \frac{(-1)^h}{h} k_{wh} k_{soh} F_h \cos(hp_p \theta + \alpha_{k_{wh}}) \quad (3.74)$$

where k_{soh} is the slot opening factor defined by [37] and F_h is a function for the curvature effect defined by [37] that is calculated for a radius equal to half of the air gap. After calculating the linkage flux due to armature reaction, the magnetizing inductance is calculated starting from its value as follows:

$$L_{magn,n_s} = \sum_{h=1}^{\infty} \frac{4}{\pi} \frac{\mu_0 LRq^2}{\delta} \left(\frac{k_{wh}}{h} \right)^2 k_{soh} F_h \quad (3.75)$$

The end winding inductance L_{ew} is calculated according to [38].

Machine resistances

The machine resistance is defined as follows:

$$R_{n_s} = \rho_{cu} \frac{Q_s L + (D + h_{ss}) \pi k_{coil}}{3 f_s A_{sl}} \quad (3.76)$$

where L is the active length of the machine, ρ_{cu} is the resistivity of the copper depending on the operating temperature ($\rho_{cu} = 1,72e-8 \Omega m$ at $20^\circ C$, temperature coefficient $\alpha = 0.0039 K^{-1}$), f_s is the filling factor of the slot. The operating temperature for calculate the copper resistivity and the value of f_s are fixed as design input date. The introduction of the parameter k_{coil} is necessary to tacking in account the type of winding as shown the next table [39]:

	Distributed winding	Concentrated 1 layer	Concentrated 2 layers
k_{coil}	$1.6Q_s/p$	1.46	0.93

Load current

The fundamental harmonic component of the load current is defined as follows:

$$\hat{I}_1 = \frac{4T}{\pi (D - \delta)^2 L \hat{B}_{\delta m1} k_{w1} \sin \beta} \quad (3.77)$$

where T is the torque, $\hat{B}_{\delta m1}$ is the estimated value of the fundamental harmonic component of the magnetic flux density of PM in the air-gap, β is the angle between magnetic flux and the current that depends of the machine saliency (for isotropic machine is $\beta = \pi/2$).

Thus the total current for stator slot is defined:

$$I = n_s \hat{I}_1 \quad (3.78)$$

Starting from (3.78) the current density is given by:

$$J = \frac{n_s I}{A_{sl} f_s} \quad (3.79)$$

where n_s is the number of the conductors for slot.

The back-EMF

The back-EMF of the phase A is defined as:

$$E_{a,n_s} = \sum_{h=1,3,5,\dots}^{\infty} 2k_{kh} \omega B_{mh} R L n_s q \sin(h\omega t + \alpha_{k\omega h}) \quad (3.80)$$

The number of conductors for slot

The number of conductors for slot is defined by next expression:

$$n_s = \frac{V}{\sqrt{(E_{a,n_s} + R_{n_s} I)^2 + (L_{a,n_s} \omega I)^2}} \quad (3.81)$$

where the phase resistance, inductance and back-EMF due to the number of conductors n_s are given by:

$$L_a = n_s^2 L_{a,n_s} \quad R = n_s^2 R_{n_s} \quad E_a = n_s E_{a,n_s} \quad (3.82)$$

Torque calculation

The torque T_{calc} can be calculated starting from back-EMFs E_a , E_b , E_c defined by (3.80) and assuming that the currents i_a , i_b , i_c to be sinusoidal time function:

$$T_{calc} = p_p (E_a i_a + E_b i_b + E_c i_c) / \omega \quad (3.83)$$

Machine losses

The stator iron losses P_{iron} under open circuit condition are calculated according to model discussed into [36].

Machine weights

The weight of each part of the machine is calculated by multiplying the volumes for the value of the density of the material.

Results of design calculations

The main dimensional features of PMSG were calculated by Maxwell 3D environment with use of the finite element method as shown in Fig. 3.12.

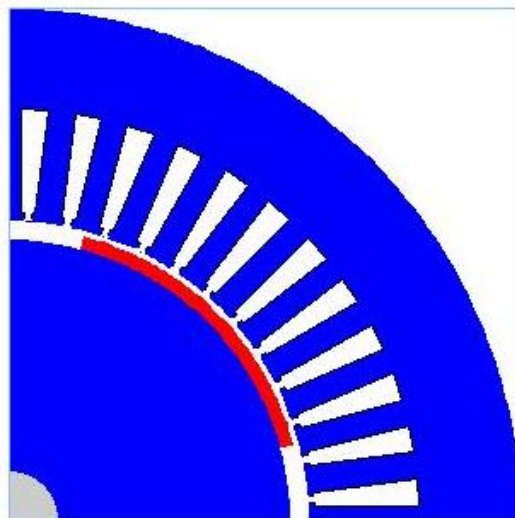


Fig. 3.12. A quarter PMSG section (symmetrical element)

Table 3.2 and Table 3.3 show main characteristics and design parameters of PMSG respectively.

TABLE 3.2: MAIN CHARACTERISTICS OF PMSG

MATERIALS	
STATOR: Iron	
Material density [kg/m ³]	7750
Stator iron stacking factor	1
Lamination thickness [mm]	0.65
Conductivity [(Ω m) ⁻¹]	3.33e6
ROTOR: Iron	
Material density [kg/m ³]	7750
Rotor iron stacking factor	1
Lamination thickness [mm]	0.65
Conductivity [(Ω m) ⁻¹]	3.33e6
PERMANENT MAGNETS: NdFeB	
Material density [kg/m ³]	7500
Remanence flux density [T]	1.06
Relative permeability	1.04
CONDUCTORS: COPPER	
Material density [kg/m ³]	8920
WINDINGS	
Number of poles:	4
Number of stator slots/pole/phase:	4
Fractional slot pitch number:	1
Copper temperature [°C]:	25
Stator slot fill factor [p.u.]	0.5

TABLE 3.3: DESIGN PARAMETERS

PMSG SPECIFICATIONS	
Rated speed [rpm]	4500
Rated torque [Nm]	22
GEOMETRICAL INPUT PARAMETERS	
Shaft diameter [mm]	18
Rotor core diameter [mm]	103
Airgap length [mm]	0.9
Magnet thickness [mm]	2.45
Magnets angle [electrical degrees]	120
Outer motor diameter [mm]	188
Machine length [mm]	165
Stator tooth width [mm]	4.8
Stator slot height [mm]	20.5
Stator slot opening / slot width [p.u.]	0.55
Slot wedge height [mm]	1.4

THE DESIGN RESULTS

FLUX DENSITIES

bdelta=0.8189056256401; % Fundamental open-circuit airgap flux density [T]
fluxts=1.1006515621202; % Max. no-load flux density in stator teeth [T]
fluxrs=1.1422978374437; % Max. no-load flux density in stator yoke [T]
fluxrr=0.49548675246677; % Max. no-load flux density in rotor yoke [T]

BACK-EMF

emf=313.98459379115; % Fundamental phase EMF (peak) [V]

TORQUE

ripple=8.3561642622461; % Torque ripple [%]

CURRENT

ia=22.010740777482; % Phase current [A]
jcurrent=2.5512172199999; % Current density [A/mm²]
s1=18.343600734636; % Stator current loading [A/mm]
nsi=132.06444466489; % Total stator current per slot [A]
f=150; % Electrical frequency [Hz]

WINDINGS

ns=6; % Number of conductors per slot
kw1=0.94946926409064; % Fundamental winding factor
conddiam=2.7870269684142; % Conductors diameter [mm]
r=0.12377315295465; % Phase resistance [Ohms]

INDUCTANCES

Ltot=0.0049411074799258; % Self-inductance [H]
Miabtot=0.00049386492812212; % Mutual inductance [H]
Lmagn=0.0043557481730636; % Magnetizing inductance [H]
Lleak=0.00055457924860947; % Slot leakage inductance [H]
Lew=3.0780058252717E-05; % End-windings inductance [H]
Ld=0.0044472425518036; % d-axis inductance [H]
Lq=0.0044472425518036; % q-axis inductance [H]

WEIGHTS

m_tot=35.070330247305; % Total active weight [kg]
m_cu=5.1560101472974; % Conductor mass [kg]
m_magnet=0.67150659397548; % PM mass [kg]
m_iron=29.242813506032; % Iron mass [kg]
m_stator=24.007153333153; % Stator's active mass [kg]
m_rotor=11.063176914152; % Rotor's active mass [kg]

LOSSES

eff=95.032893654282; % Efficiency [%]
prated=10367.255756846; % Rated power P [W]
cosphi=0.96009529734739; % Power factor cos(phi)
p_copper=89.947072176597; % Copper losses [W]
p_iron=451.92069462892; % Stator iron losses [W]

The following figures report the air gap flux density, the phase back-EMF and the torque of PMSG.

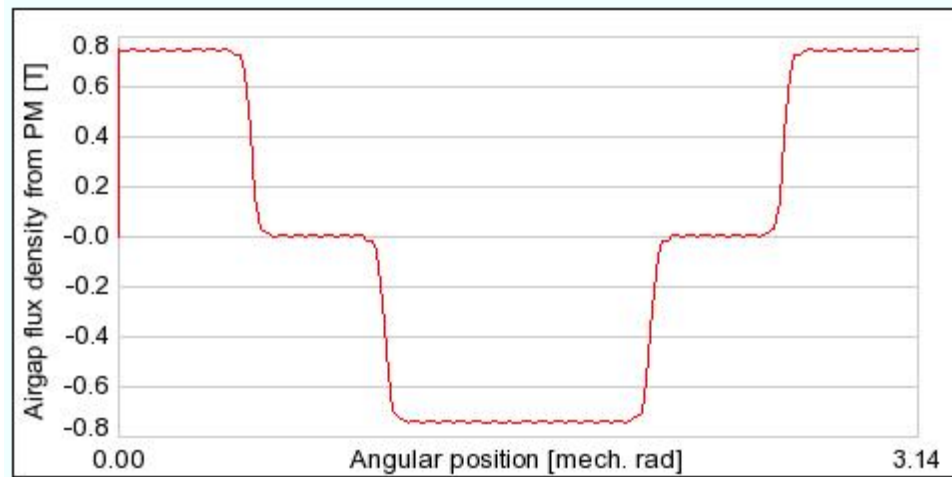


Fig. 3.13. Air-gap flux density as rotor angular position function

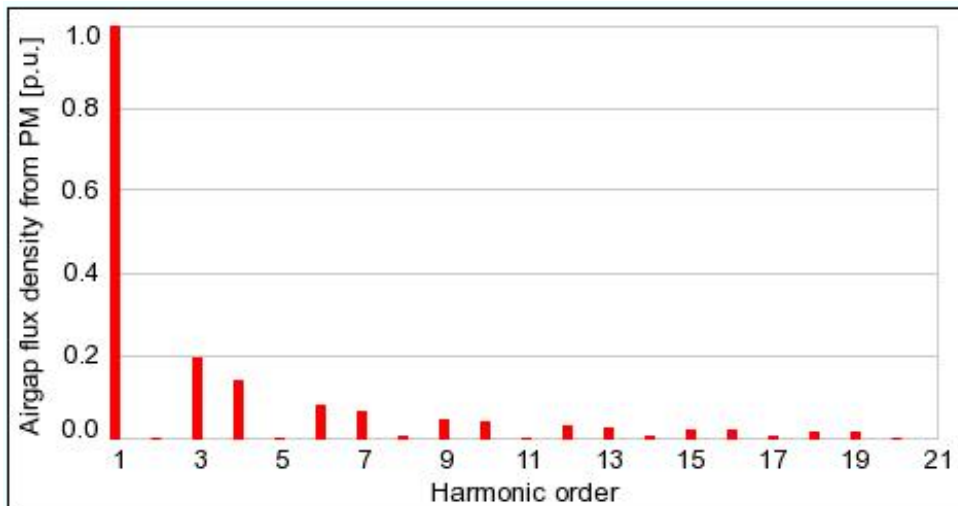


Fig. 3.14. Air-gap flux density spectrum

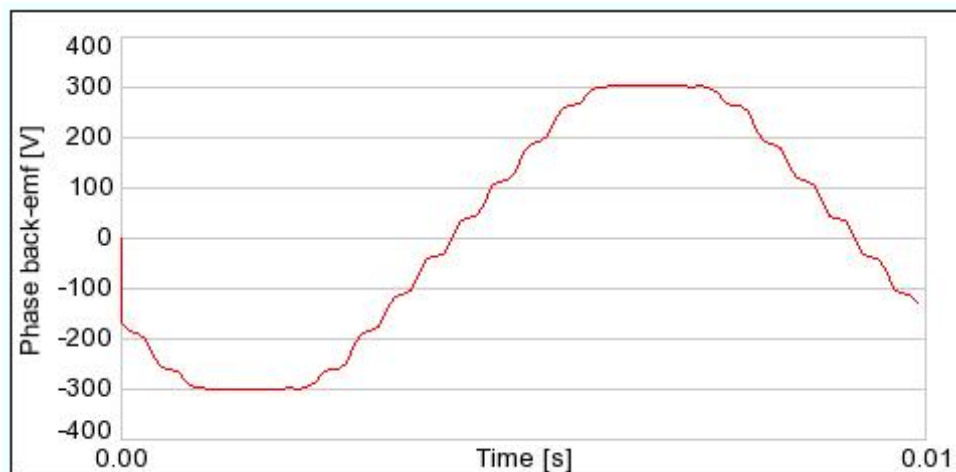


Fig. 3.15. Phase back-EMF

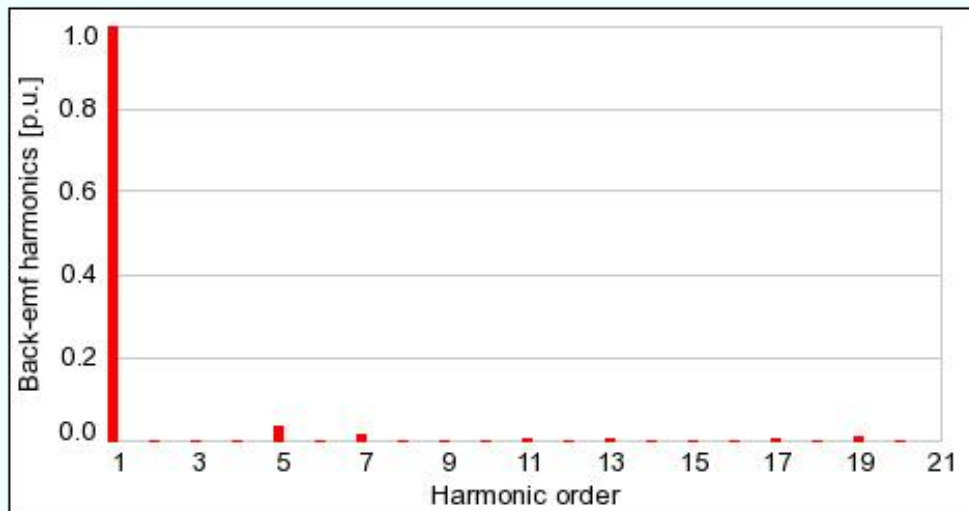


Fig. 3.16. Phase back-EMF spectrum

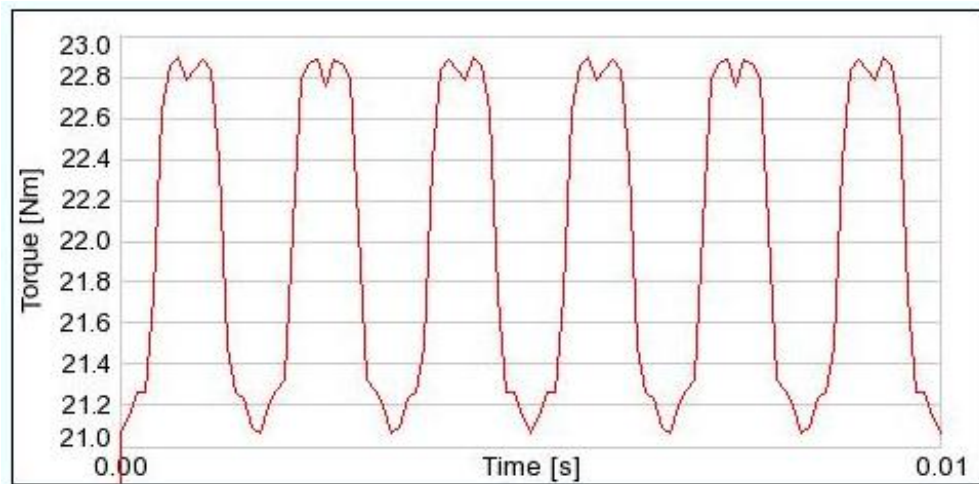


Fig. 3.17. Torque of PMSG

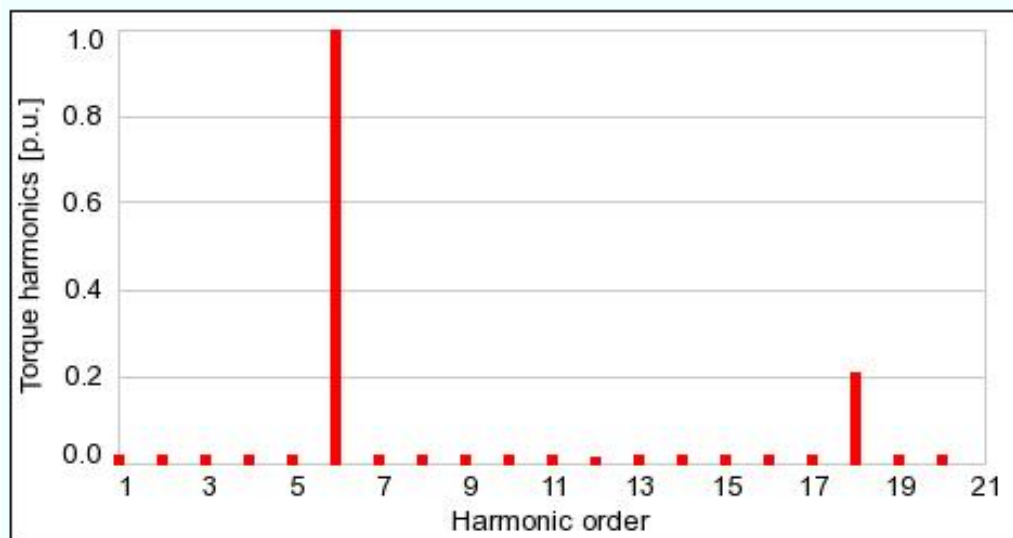


Fig. 3.18. Torque spectrum

3.3.2 Quasi-Resonant branch design

From equation of DC-link current (3.37), the design condition for the Quasi-Resonant branch corresponding to satisfying inequality (3.38) so that the current of DC-link becomes negative after the time interval $t_1 + t_2$.

For the design of components of quasi-resonant branch the following design condition has been imposed:

$$Z_0 I_0 = 0.8 \cdot V_{dc} \quad (3.84)$$

where the values of quantities I_0 and V_{dc} are known.

Therefore fixing the resonant pulsation ω_0 such that the SVPVM period to be is integer multiple of resonant period, the values of quantities L_r and C_r can be calculated by the expression of ω_0 and the equation (3.84).

Table 3.4 shows the parameters of the quasi-resonant branch for a fixed resonant frequency $f_r = 80\text{kHz}$.

TABLE 3.4: DESIGN PARAMETERS OF THE QUASI-RESONANT BRANCH

QUASI-RESONANT BRANCH SPECIFICATIONS	
Switch component	IGBT
IGBT's ESR [Ω]	0.01
Resonant inductance [μH]	14
Resonant capacitor [nF]	284
Resonant frequency [kHz]	80

3.3.3 Discrete-time Space Vector PWM

A discrete-time Space Vector PWM was adopted for generating the pulse switch signals of the VSI's switches; each time interval of the VSI's switches is an integer multiples number of the resonant period T_r , so to drive the inverter as a ZVS converter (soft-switched VSI).

In the following, the flow chart of the proposed space vector PWM is presented when the voltage vectors $\mathbf{v}_1, \mathbf{v}_2$ and \mathbf{v}_0 are applied for the time intervals T_1, T_2 and T_0 respectively.

```
*****
file svpwm.m
*****
Inputs:  kt      ratio between sampling period and resonant period
         ucc     maximum amplitude of the VSI output voltage vector
         voltdes amplitude of the input voltage vector "vdes"
         fasevd  phase of the input voltage vector "vdes"
*****
Outputs: v1      first voltage vector component of vdes
         t1      integer number of resonant periods of application of v1
         v2      second voltage vector component of vdes
         t2      integer number of resonant periods of application of v2
         t0      integer number of resonant periods of application of v0
         tp      vector tp=[t1,t2,t0]
*****
```

Fig. 3.19. Inputs and outputs of the proposed discrete-time Space Vector PWM

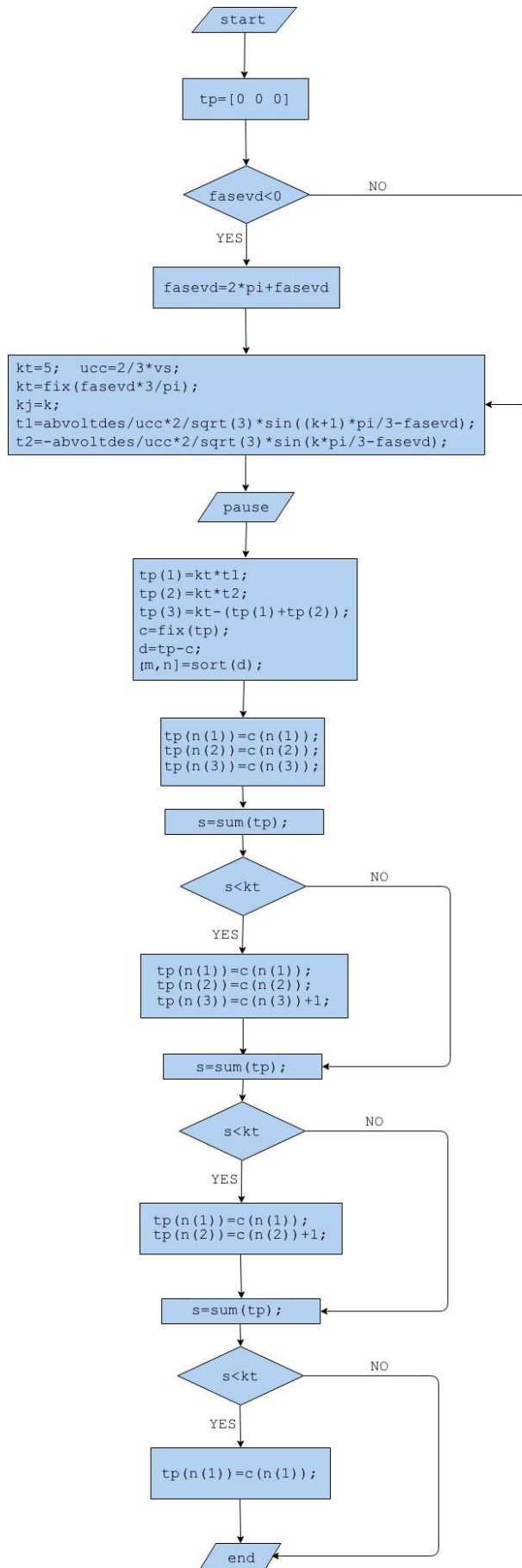


Fig. 3.20. Flow chart of proposed discrete-time Space Vector PWM

Chapter 4

NUMERICAL AND EXPERIMENTAL RESULTS

Simulations of the proposed electrical sub-system were carried out under Simulink and Matlab environment in order to prove its high efficiency and high performance.

The behavior of the controlled system during the steady state and transient is highlighted by the proposed simulations.

As mentioned in the Chapter 3, the targets of the control strategy of the Double Stage AC-AC Power Converter (DSACPC) are defined as follows:

for the Stage 1

- 1.a) keeping the DC-link voltage at a desired value;
- 1.b) tracking of the maximum power point draw from the thermodynamic sub-system.

for the Stage 2

- 2.a) generation of desired values of instantaneous active and reactive power on the grid utility, in the case of balanced conditions of the grid utility;
- 2.b) current harmonic rejection, in the case of unbalanced conditions of the grid utility.

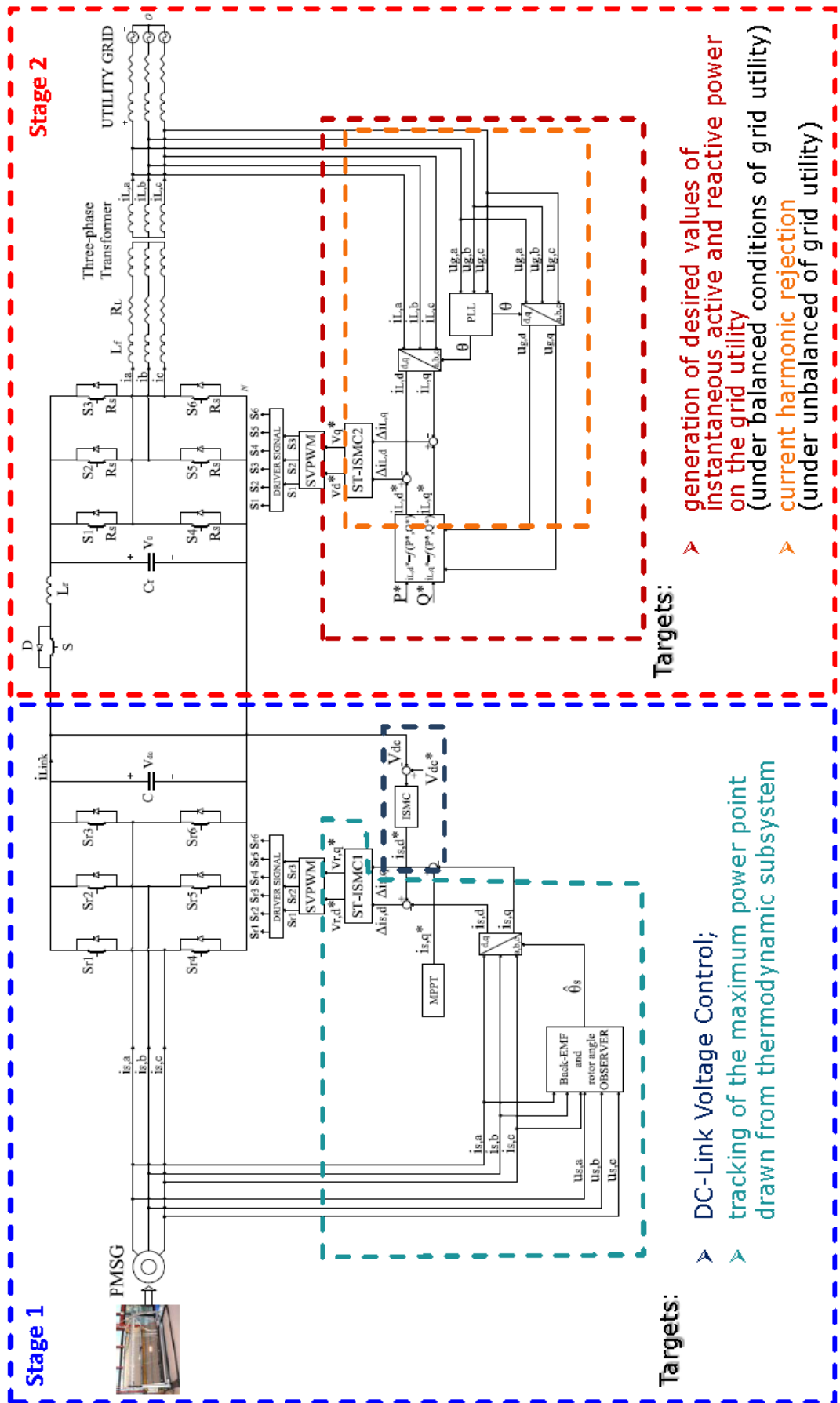


Fig. 4.1. Targets of the proposed Full Sliding Mode control of DSACPC.

Discrete models were used with a simulation step time of $1\mu s$.

The parameters of simulated system are given in Table 4.1.

TABLE 4.1: PARAMETERS OF THE SIMULATED SYSTEM

	Parameters	Values
PMSG	Rated speed	4500 rpm
	Phase stator resistance R	0.124Ω
	Phase stator inductance L_s	5 mH
	Maximum mechanical Power	10 kW
	Components	Mosfet
PWM Rectifier	Mosfet's ESR	0.01Ω
	Switching frequency	20 kHz
	DC Capacitor bank	$1100 \mu F$
Quasi-resonant branch	Components	IGBT
	IGBT's ESR	0.01Ω
	Resonant inductance L_r	$14 \mu H$
	Resonant capacitor C_r	284 nF
	Resonant frequency	80 kHz
Voltage Source Inverter	Components	IGBT
	IGBT's ESR	0.01Ω
	Filter inductance L_f	0.4 mH
	Filter resistance R_L	0.01Ω
	Switching frequency	16 kHz

The behavior of the controlled system during the steady-state and transient is highlighted by the proposed simulations:

under balanced conditions of the grid-utility:

- ❖ Simulation 1: $P^* = 6\text{kW}$; $Q^* = 0\text{kVAr}$ ($v_{dc}^* = 600\text{V}$);
- ❖ Simulation 2: $P^* = 6 \div 3\text{kW}$; $Q^* = 0\text{kVAr}$ ($v_{dc}^* = 600\text{V}$);
- ❖ Simulation 3: $P^* = 3\text{kW}$; $Q^* = 0 \div 3\text{kVAr}$ ($v_{dc}^* = 600\text{V}$);

under unbalanced conditions of the grid-utility:

- ❖ Simulation 4: $i_{L,d}^* = 6.15\text{A}$; $i_{L,q}^* = 0\text{A}$ ($v_{dc}^* = 600 \div 500\text{V}$);

In the following the simulations results are depicted and an experimental prototype is tested in order to validate the performance of the proposed control strategy.

4.1. Numerical Results

4.1.1. Simulation 1: $P^* = 6\text{kW}$; $Q^* = 0\text{kVAr}$ ($v_{dc}^* = 600\text{V}$)

For the first simulation let us assume balanced condition of the grid utility and the reference values of the DSACPC control strategy are given in Table 4.2:

TABLE 4.2: REFERENCE VALUES OF SIMULATION 1

DSACPC Stage	Parameters	Values
<i>Stage 1</i>	Rated speed	4500 rpm
	DC-link voltage v_{dc}^*	600 V
<i>Stage 2</i>	Instantaneous active power P^*	6 kW
	Instantaneous reactive power Q^*	0 VAr

STAGE 1

The Fig. 4.2 shows the observed electrical rotor angle of PMSG with respect to its actual value:

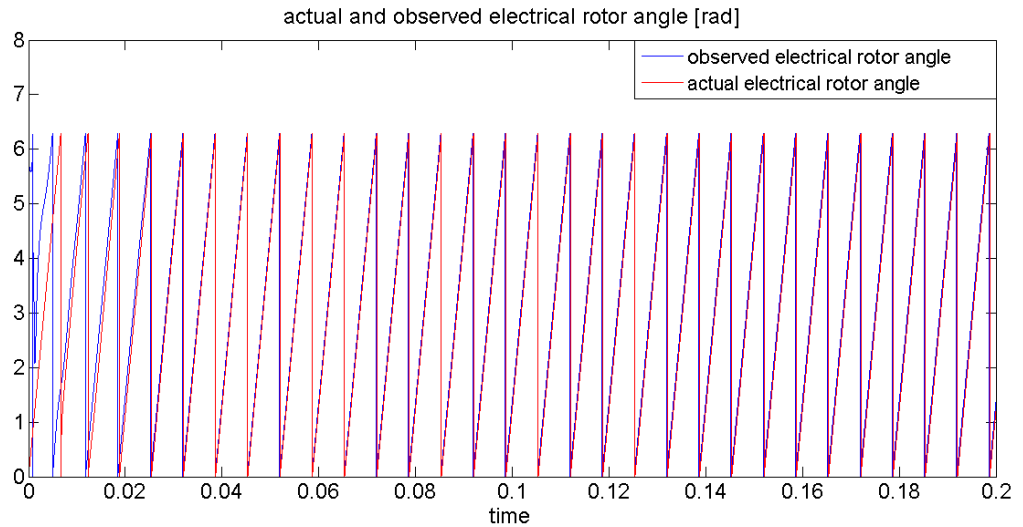


Fig. 4.2. Actual and estimated electrical rotor angle of PMSG at 4500 rpm.

In the Fig. 4.3 the observed back-EMFs of PMSG are shown and then the back-EMF phase is compared with its actual value in Fig. 4.4 in order to prove the performance of the proposed sliding mode observer.

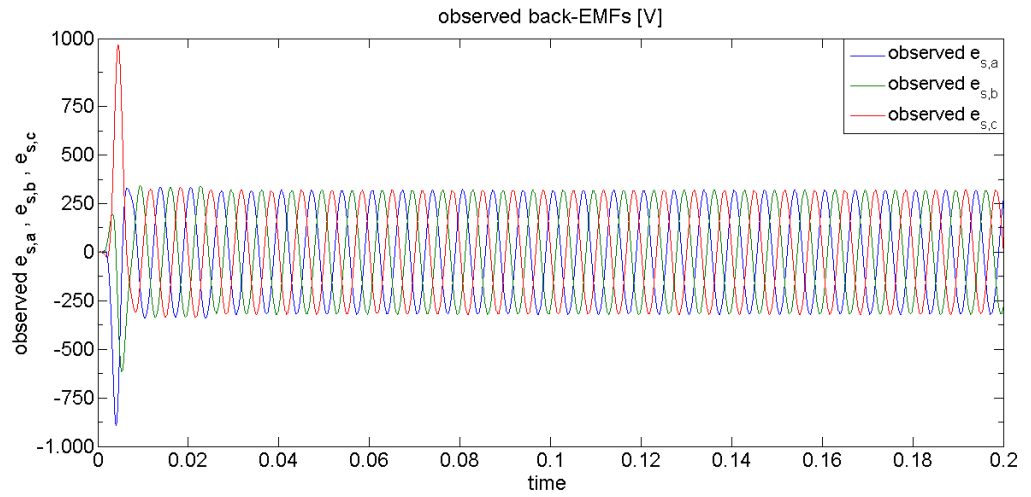


Fig. 4.3. (a)

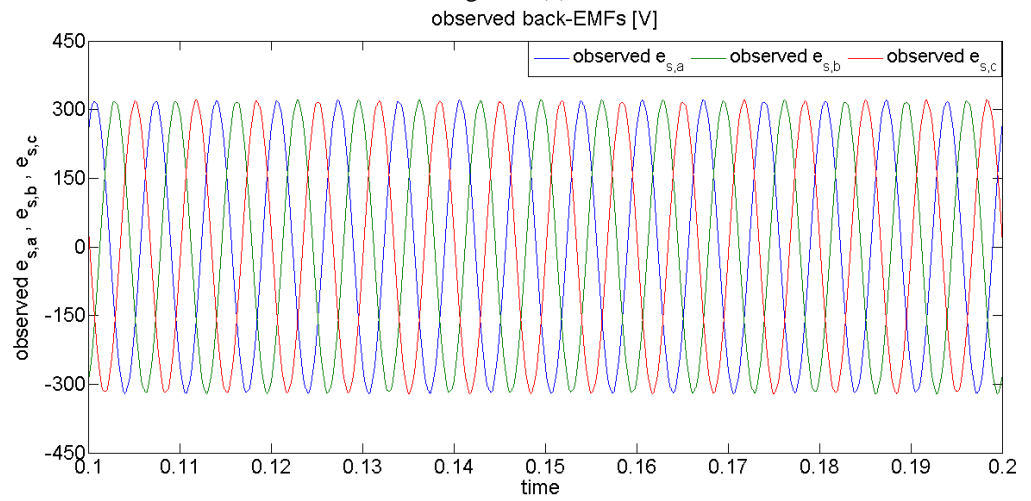


Fig. 4.3. (b)

Fig. 4.3. (a) Observed back-EMFs of PMSG; (b) details of the time interval 0.1÷0.2 s.

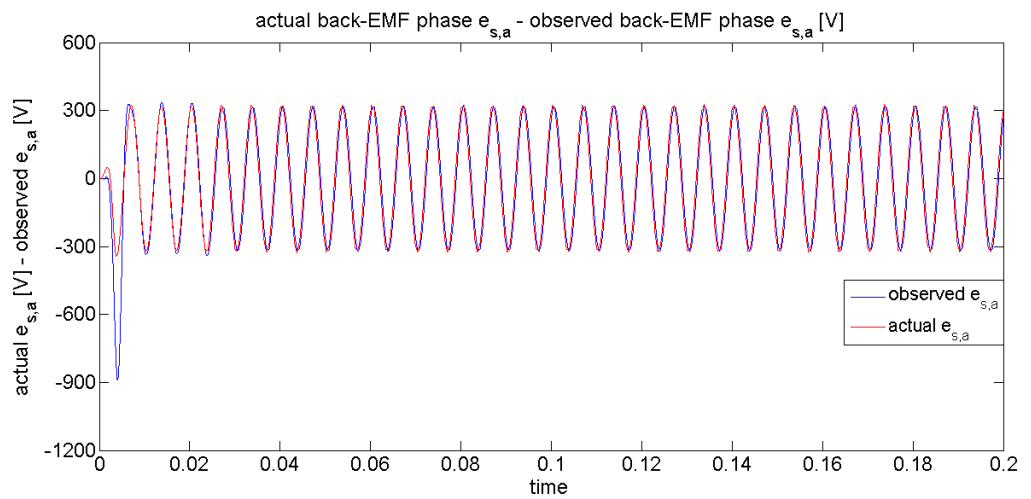


Fig. 4.4. (a)

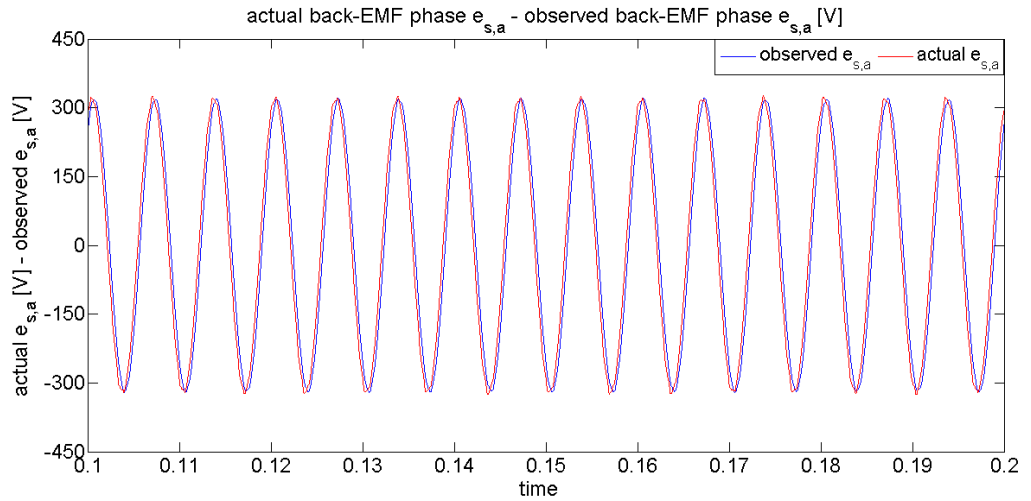


Fig. 4.4. (b)

Fig. 4.4. (a) Actual and observed back-EMF phase of PMSG; (b) details of the time interval 0.1÷0.2 s.

Fig. 4.5 shows the errors of d-q axis components of PMSG stator currents in order to test the response of the control of the Stage 1.

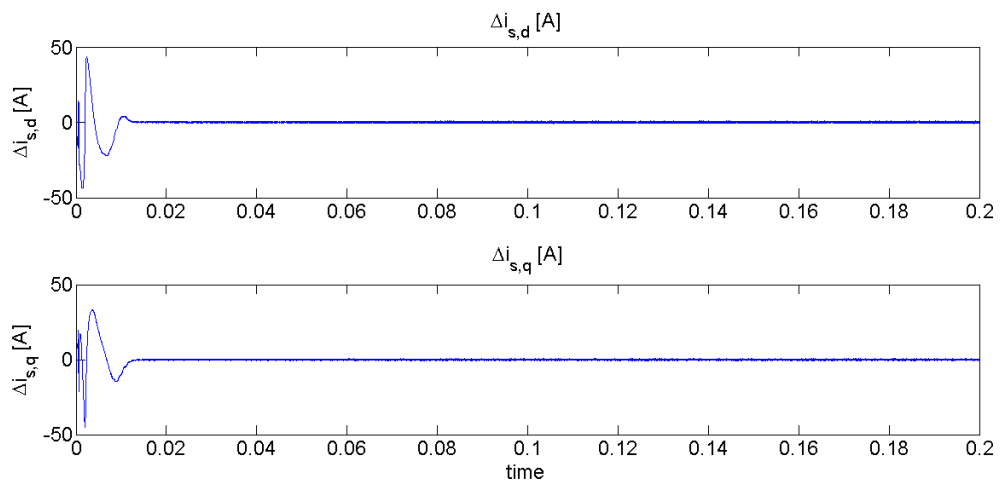


Fig. 4.5. (a)

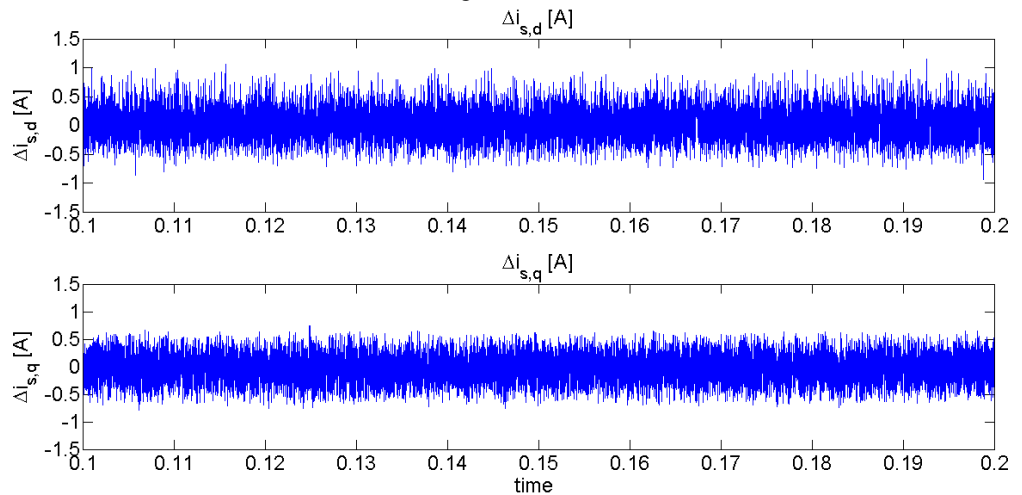


Fig. 4.5. (b)

Fig. 4.5. (a) the errors of d-q axis components of PMSG stator currents; (b) details of the time interval 0.1÷0.2 s.

The actual DC-link voltage follows its reference values as shown in the next figure.

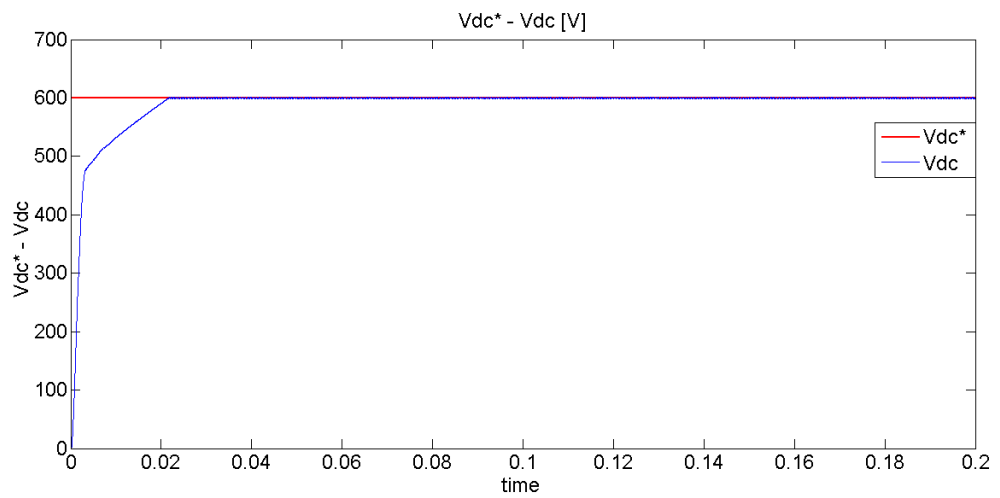


Fig. 4.6. (a)

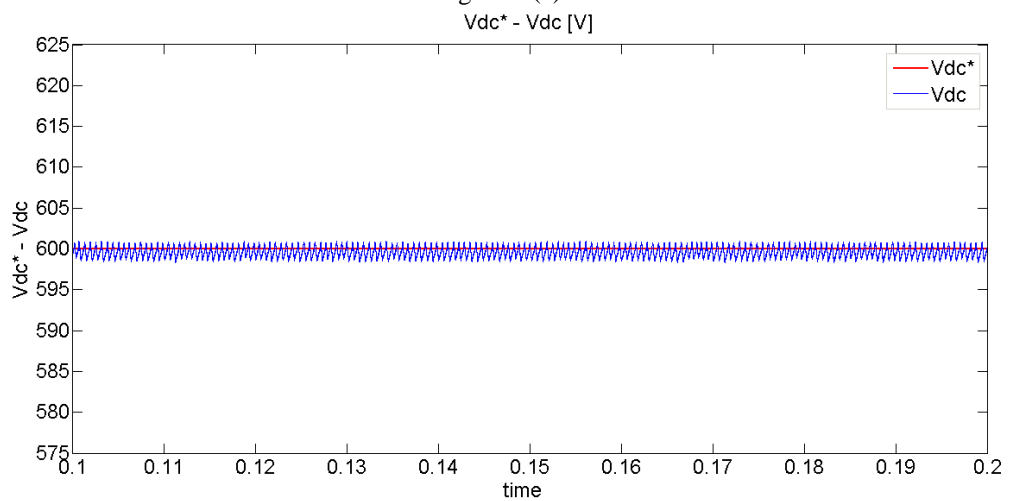


Fig . 4.6. (b)

Fig. 4.6. (a) The actual and reference value of the DC-link voltage;
(b) details of the time interval 0.1÷0.2 s.

STAGE 2

Fig. 4.7 shows the grid-utility voltages under balanced condition of the grid.

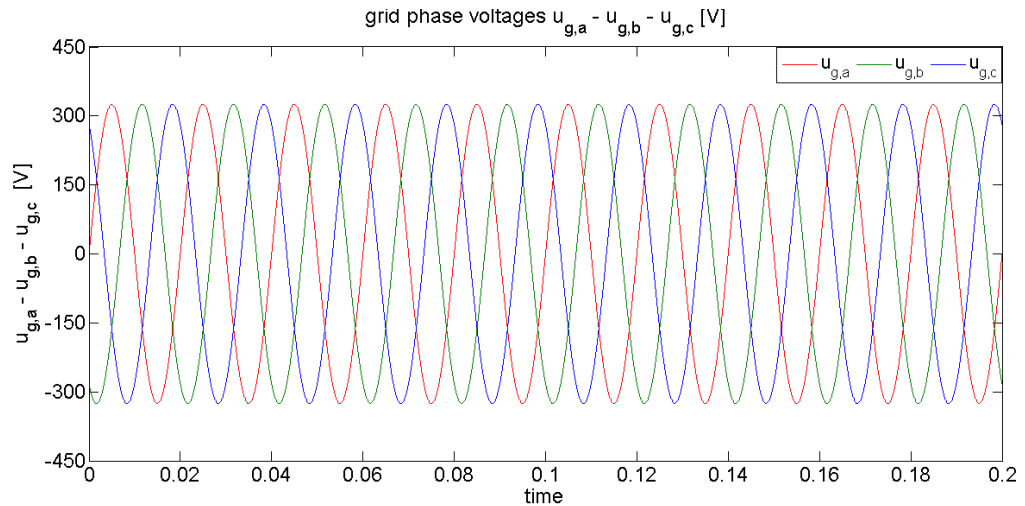


Fig. 4.7. The grid-utility voltages.

The grid-side inverter currents are shown in Fig. 4.8; the actual d-q axis components of the grid-utility currents and the errors of d-q axis components of the grid currents are shown in Fig. 4.9 and 4.10 respectively, in order to prove the performance of the adopted control strategy for the Stage 2.

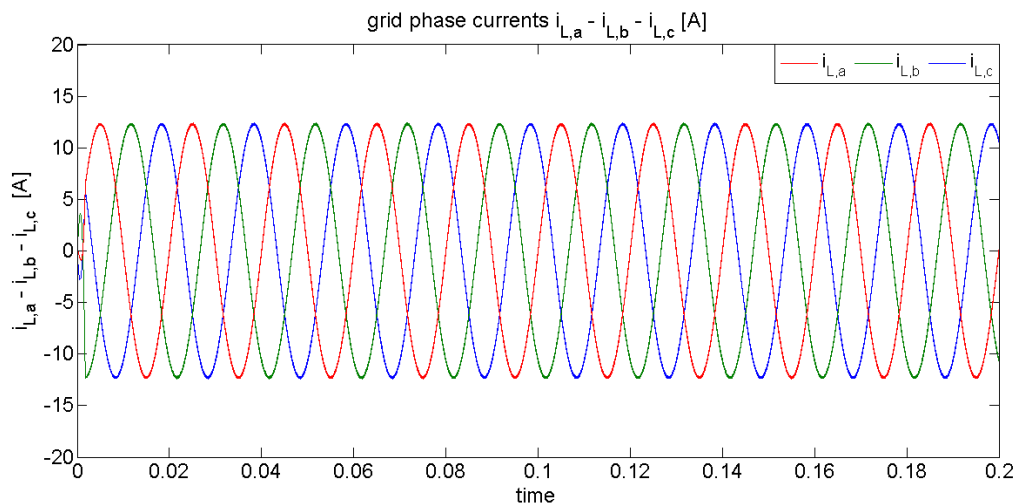


Fig. 4.8. The grid-side inverter currents.

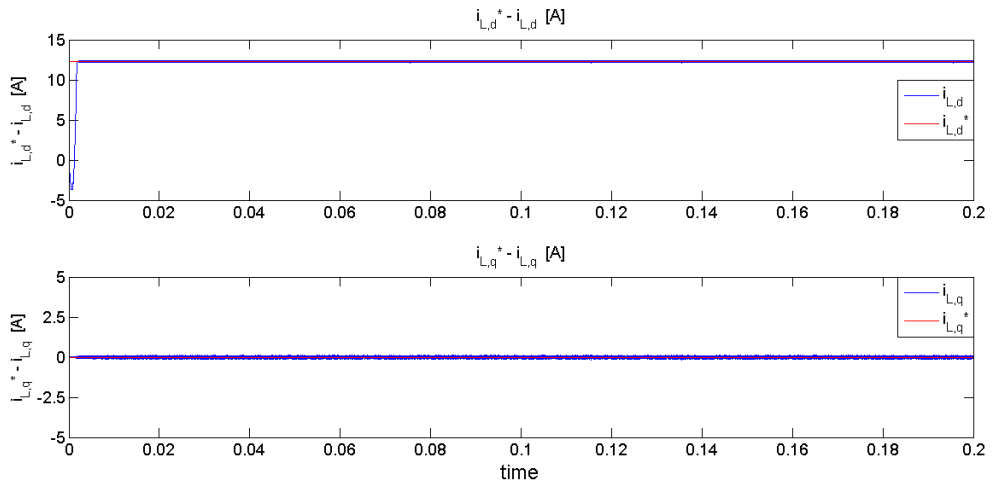


Fig. 4.9. (a)

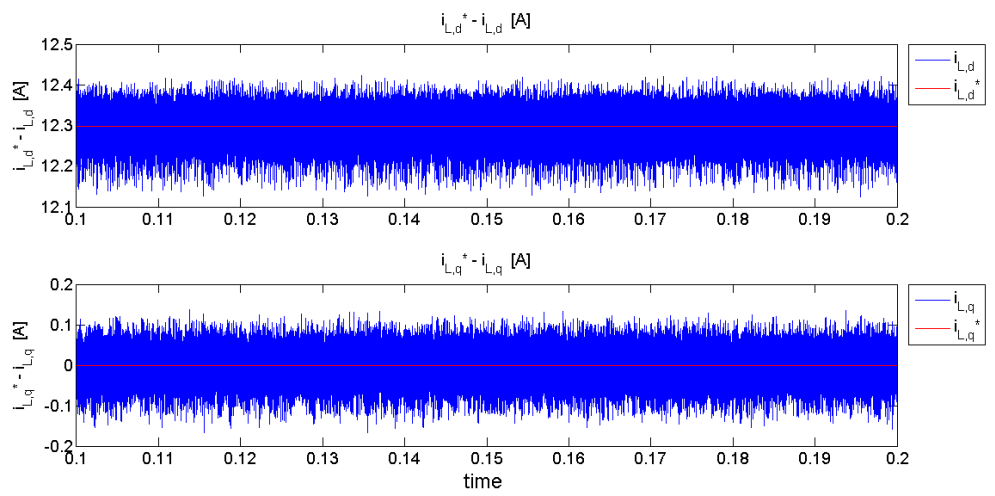


Fig. 4.9. (b)

Fig. 4.9. (a) The actual and reference values of d-q axis components of grid-utility currents; (b) details of the time interval 0.1÷0.2 s.

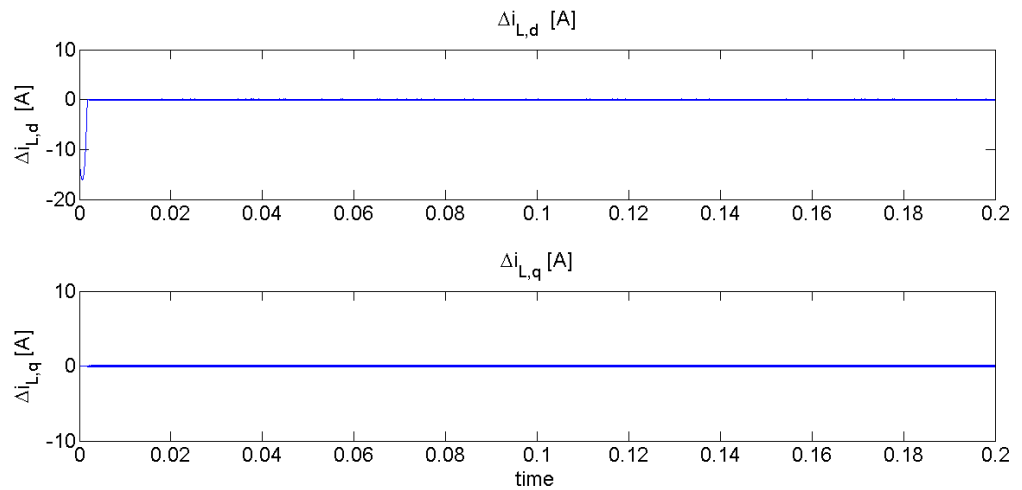


Fig. 4.10. (a)

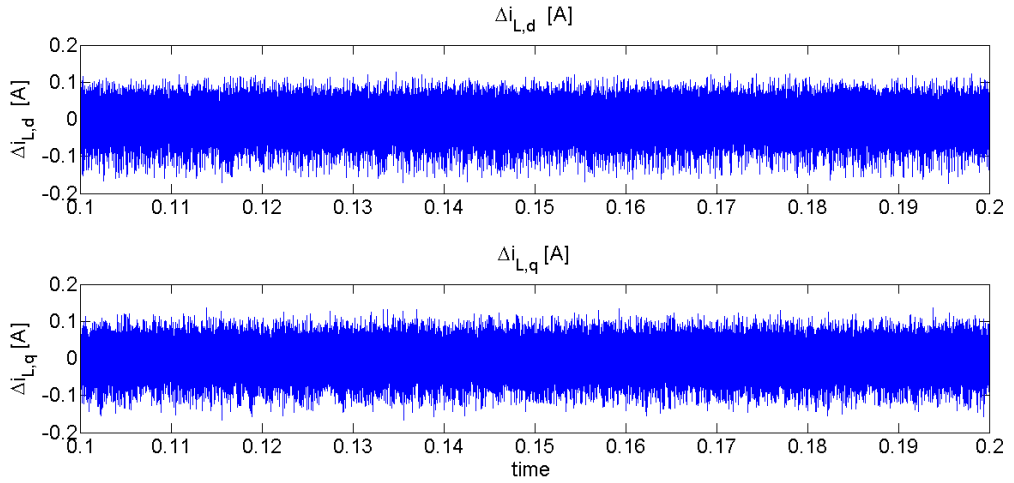


Fig. 4.10 (b)
 Fig. 4.10. (a) The errors of d-q axis components of grid-utility currents;
 (b) details of the time interval 0.1÷0.2 s.

The proposed control strategy of the Stage 2 is able to follows the reference value of instantaneous active and reactive power as shown in Fig. 4.11.

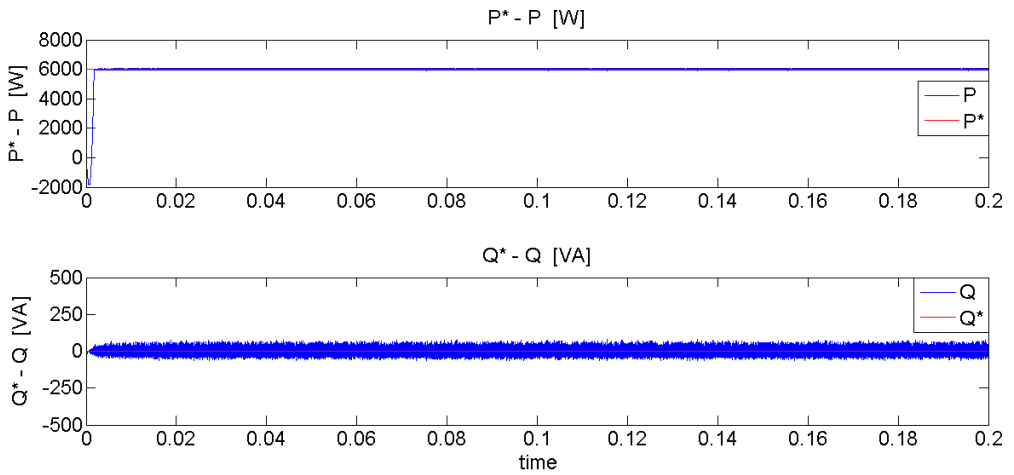


Fig. 4.11. (a)

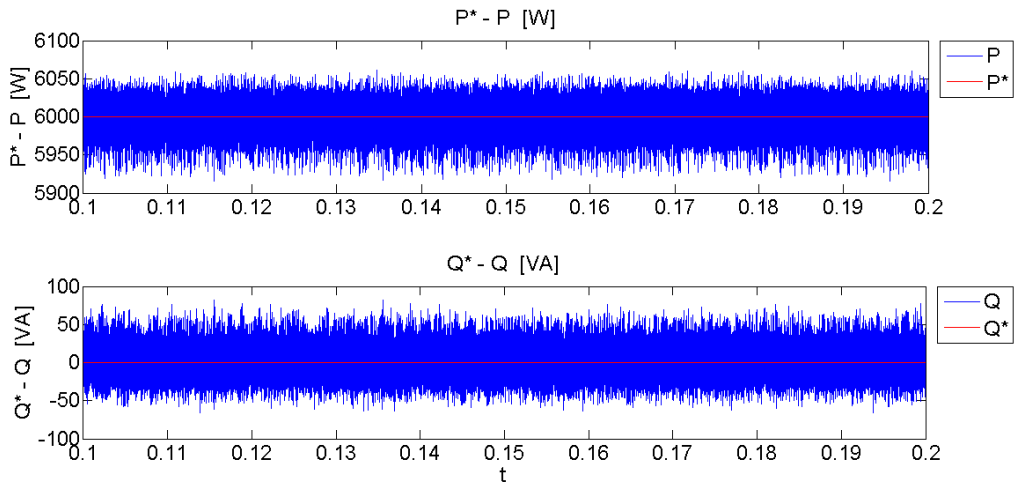


Fig. 4.11. (b)

Fig. 4.11.: (a) The actual and reference values of the active and reactive power;
 (b) details of the time interval 0.1÷0.2 s.

Since the active power reference is set to zero, the phase displacement between the phase voltages and currents on the grid-utility is always equal to zero as shown in Fig. 4.12., where the zero of the d-q axis components of the grid currents has been translated to the value of -20 A on the ordinate axis to represent these on the same figure.

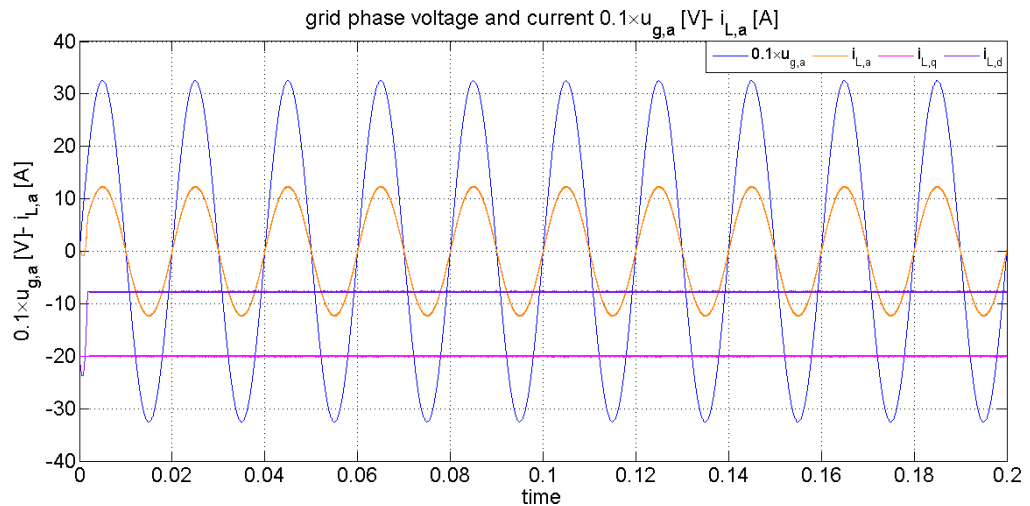


Fig. 4.12. (a)

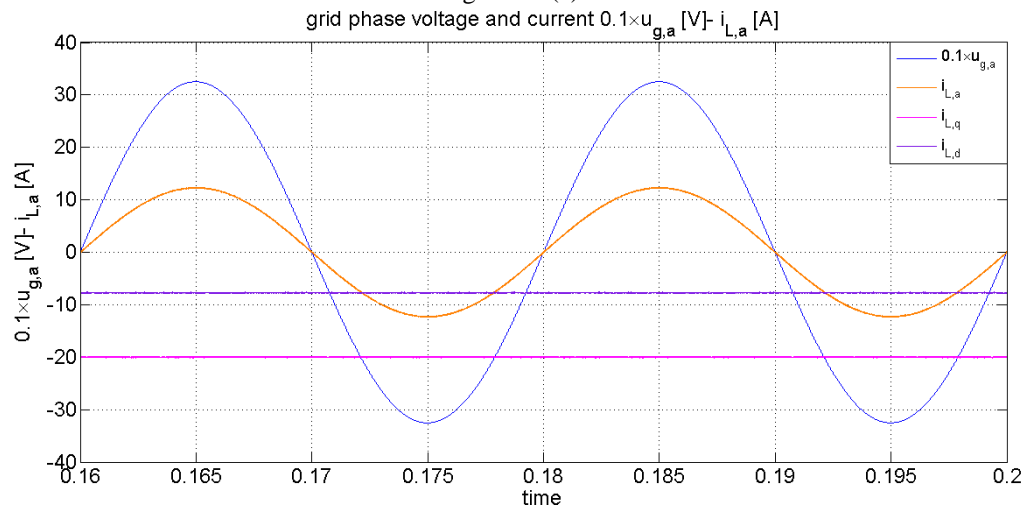


Fig. 4.12. (b)

Fig. 4.12. (a) The phase voltage and current of the grid, actual d-q axis components of the grid currents; (b) details of the time interval 0.16÷0.2 s.

The presence of the quasi-resonant branch allow to achieve a ZVS if the switching frequency of the VSI's switches is an integer multiple of the resonant frequency.

The resonant frequency has been fixed equal to 80 kHz as the next figure proves.

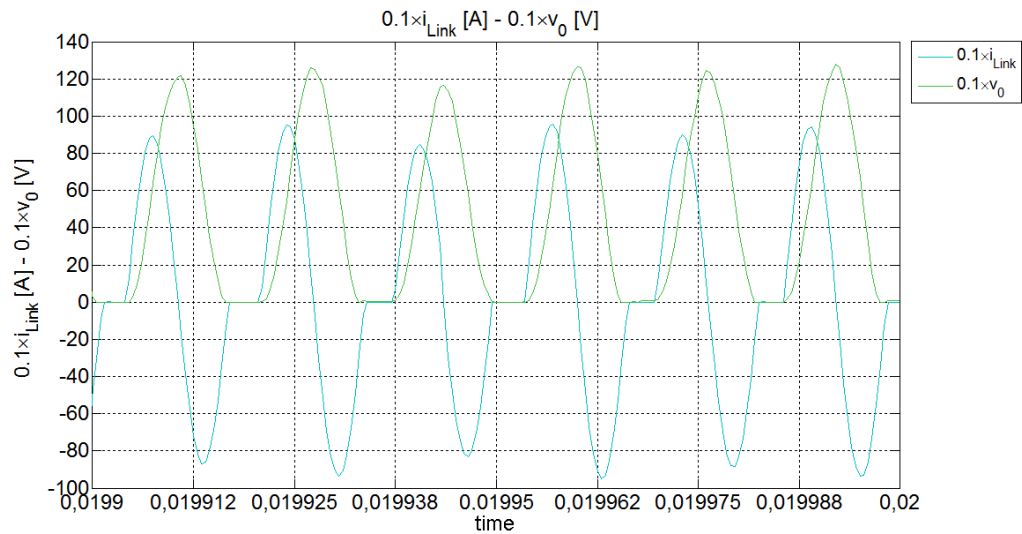


Fig. 4.13. The DC-link current and the resonant capacitor voltage as time functions.

The errors of the d-q axis components of the grid-utility currents can be treated as output of the ST-ISMC of the Stage 2 and the latter tend to sliding manifold with a reducer chattering as shown in Fig. 4.14.

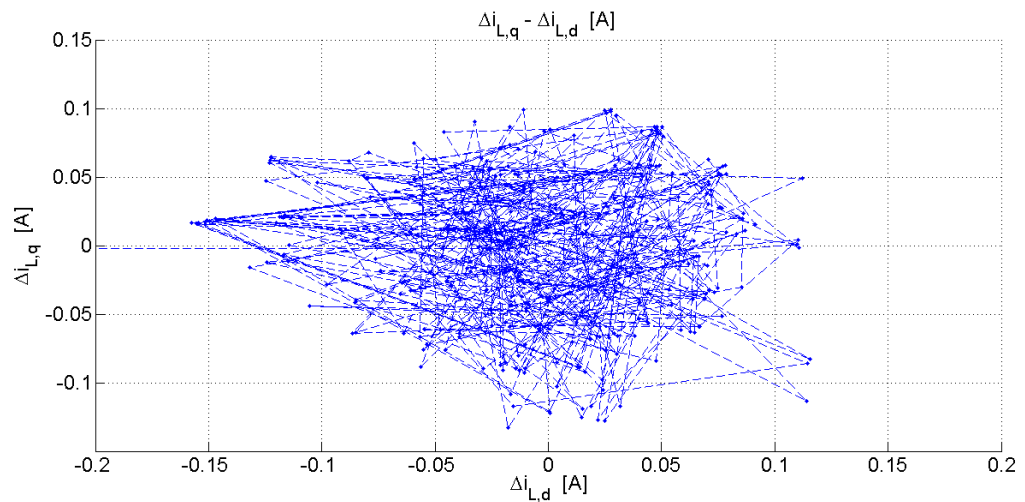


Fig. 4.14. The errors of d-q axis components of the grid currents in the phase space.

In particular, the mean values of the errors of the d-q axis components of the grid-utility currents are:

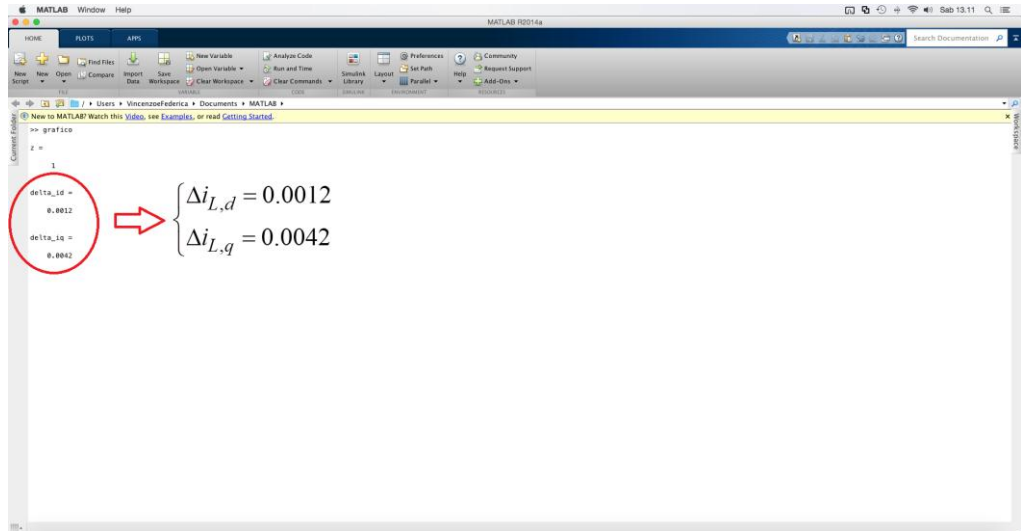


Fig. 4.15. The mean values of the errors of d-q axis components of the grid currents.

4.1.2. Simulation 2: $P^* = 6 \div 3 \text{ kW}$; $Q^* = 0 \text{ kVAr}$ ($v_{dc}^* = 600 \text{ V}$)

The second simulation is carried out in order to test the dynamic response of the control strategy of the DSACPC under balanced condition of the grid-utility. The reference values of the control strategy are given in Table 4.3:

TABLE 4.3: REFERENCE VALUES OF SIMULATION 2

DSACPC Stage	Parameters	Values
<i>Stage 1</i>	Rated speed	4500 rpm
	DC-link voltage v_{dc}^*	600 V
<i>Stage 2</i>	Instantaneous active power P^*	$6 \div 3 \text{ kW}$
	Instantaneous reactive power Q^*	0 VAr

The reference active power P^* is step-changed at 0.02 s from 6 kW (corresponding to a reference d-axis current component $i_{L,d}^*$ of 12.3 A) to 3 kW (corresponding to a reference d-axis current component $i_{L,d}^*$ of 6.15 A) during a time of 300 μs and then backed to 6 kW at 0.06 s during the same time of 300 μs , while the reference reactive power is contextually fixed to zero (corresponding to a reference q-axis current component $i_{L,q}^*$ of 0 A).

STAGE 1

The observed electrical rotor angle of PMSG follows its actual value as shown in Fig. 4.15.

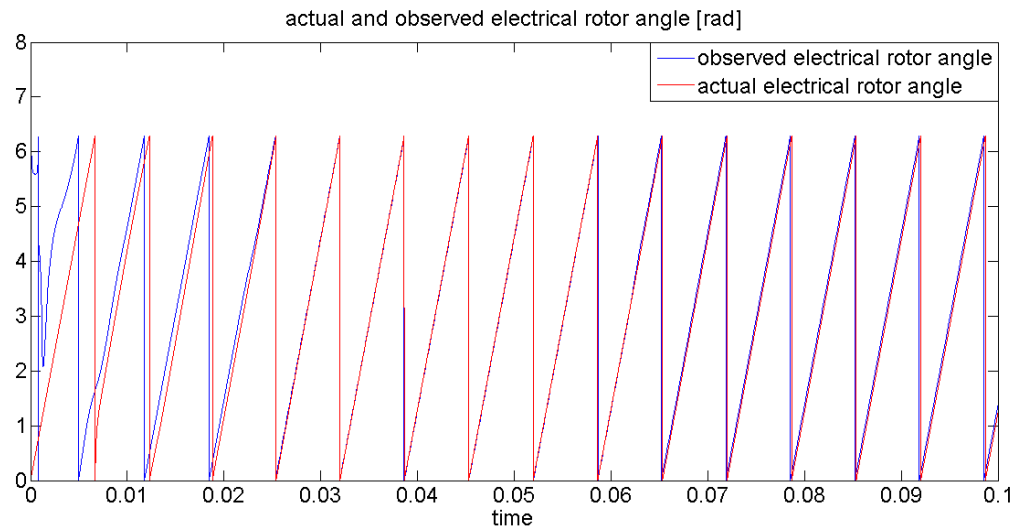


Fig. 4.15. Actual and estimated electrical rotor angle of PMSG at 4500 rpm.

The following two figure show the observed back-EMFs of PMSG and the back-EMF phase with respect to its actual value:

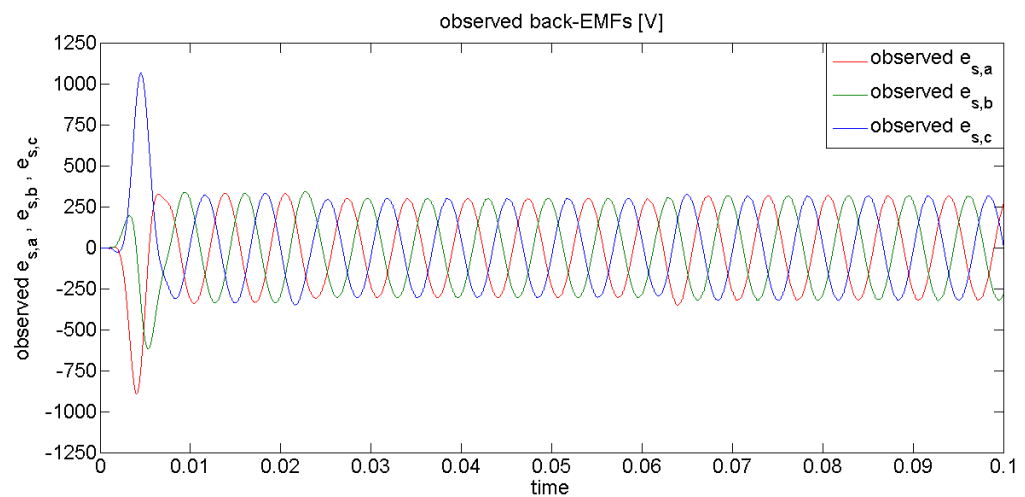


Fig. 4.16. (a)

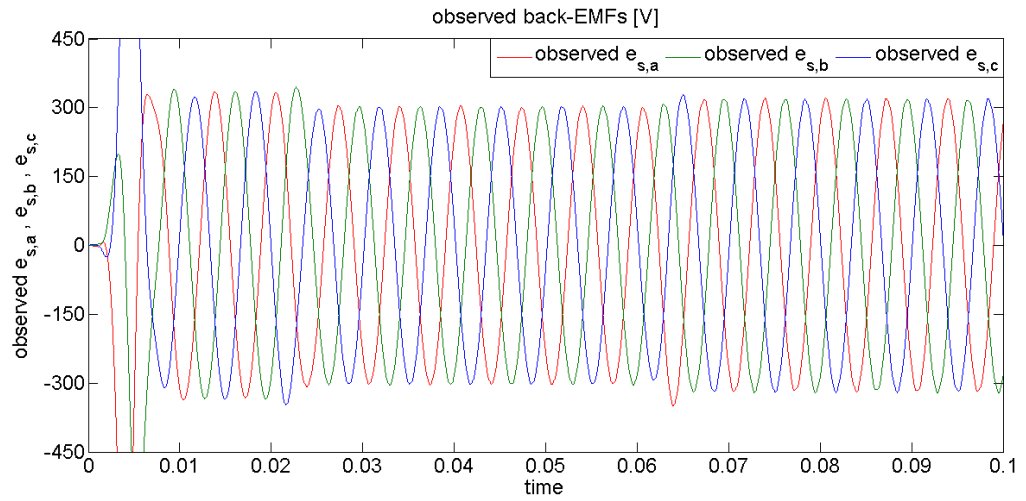


Fig. 4.16. (b)

Fig. 4.16. (a) Observed back-EMFs of PMSG; (b) details of the steady-state.

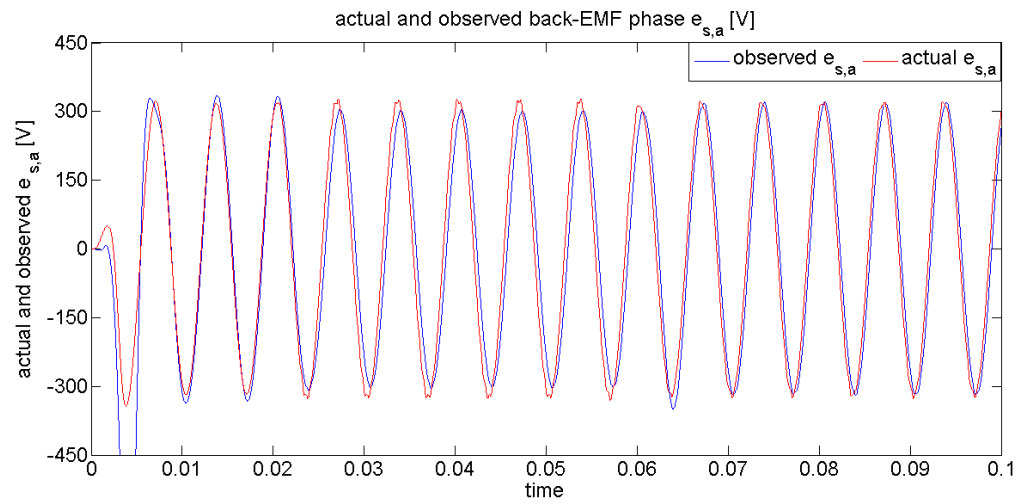


Fig. 4.17. (a)

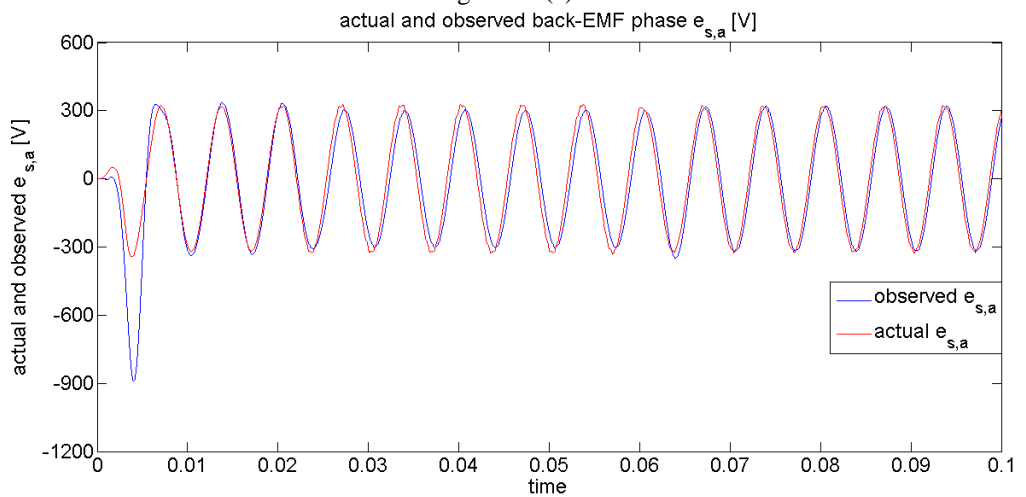


Fig. 4.17. (b)

Fig. 4.17. (a) Actual and observed PMSG back-EMF phase; (b) zoom around the actual value.

The control of Stage 1 is able to guarantee small values of errors of d-q axis components of PMSG stator currents and to keep the reference value of the DC-link voltage as depicted in Fig. 4.18 and Fig. 4.19.

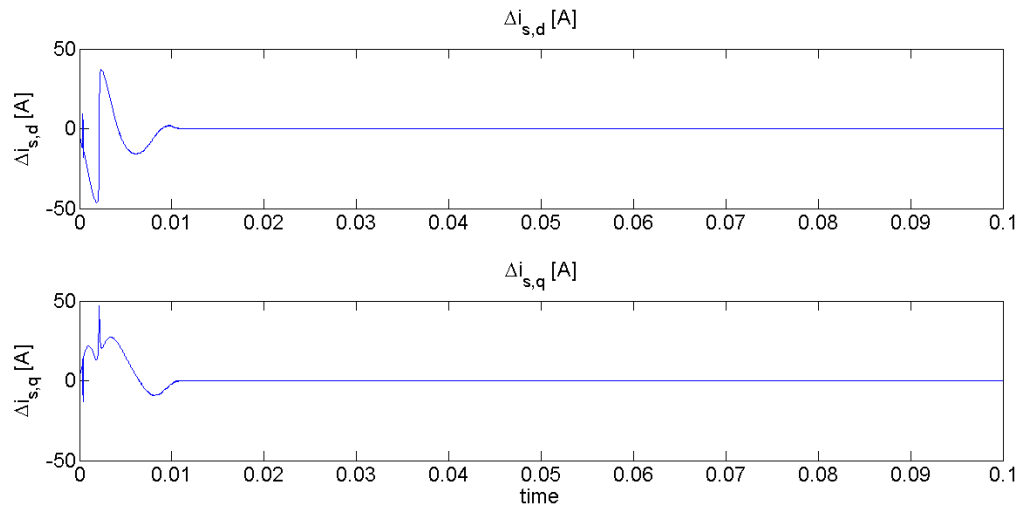


Fig. 4.18. (a)

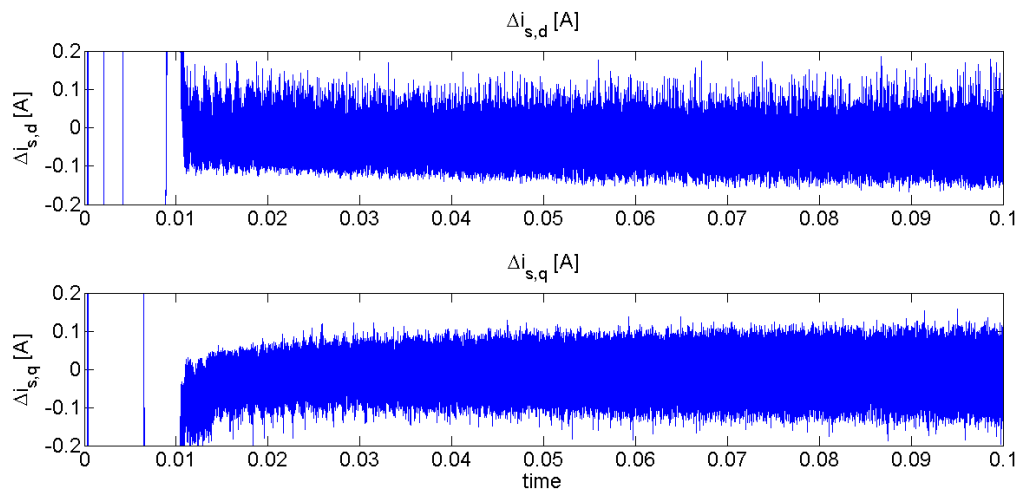


Fig. 4.18. (b)

Fig. 4.18.: (a) The errors of d-q axis components of PMSG stator currents; (b) details of the steady-state.

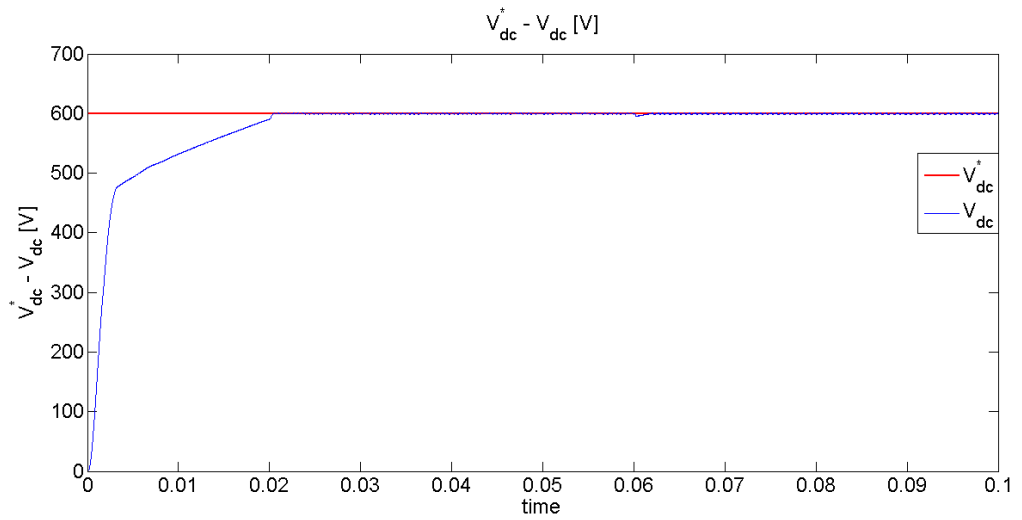


Fig. 4.19. (a)

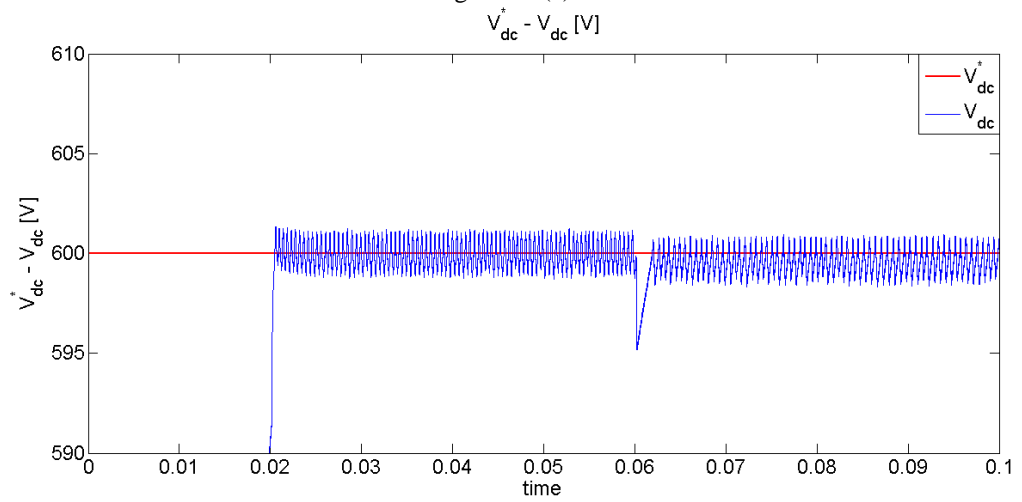


Fig. 4.19. (b)

Fig. 4.19.: (a) The actual and reference value of the DC-link voltage;
(b) zoom around the reference value

STAGE 2

The grid-utility voltages are supposed balanced as show Fig. 4.20.

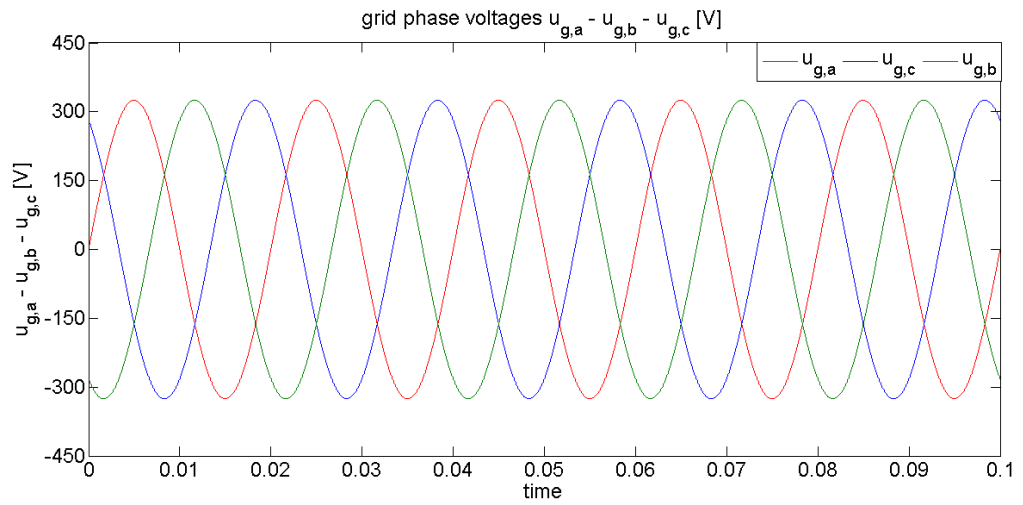


Fig. 4.20. The grid-utility voltages.

Fig. 4.21. shows the grid currents, while Fig. 4.22. and Fig. 4.23. show the actual d-q axis components of the grid-utility currents and the errors of d-q axis components of the grid currents respectively, in order to prove the goodness of the adopted control strategy for the Stage 2.

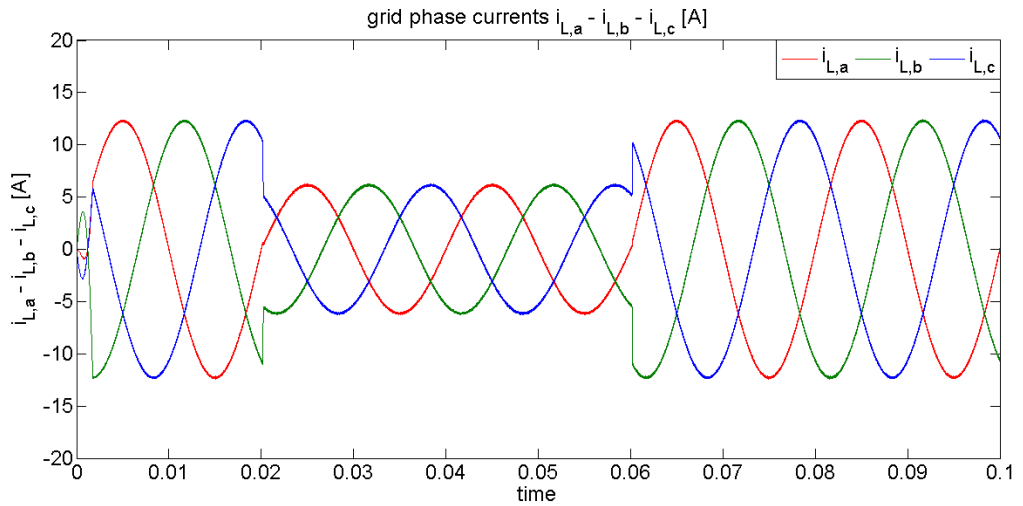


Fig. 4.21. The grid-side inverter currents.

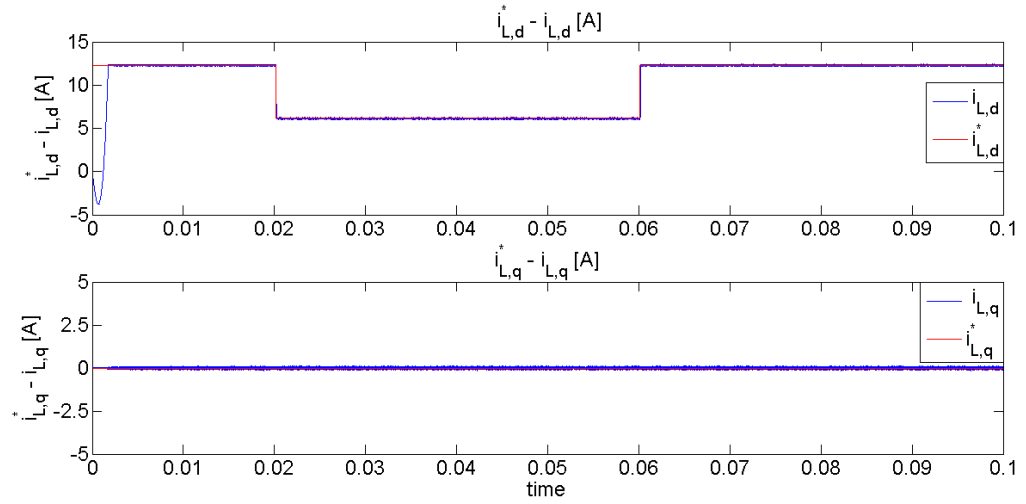


Fig. 4.22. (a)

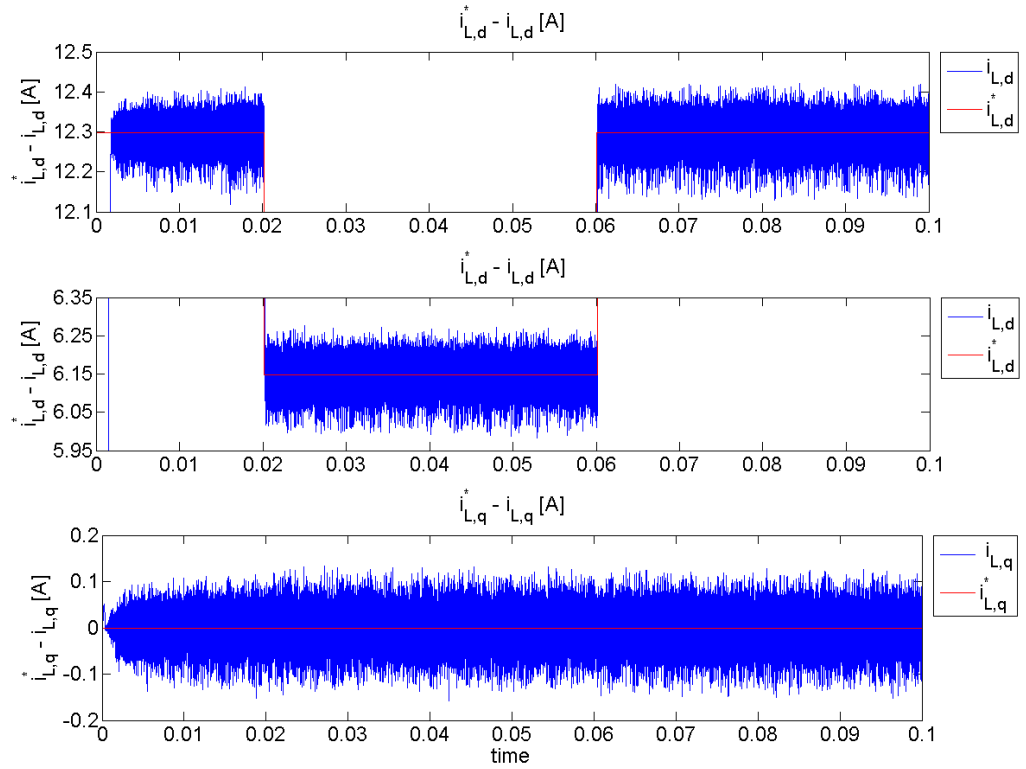


Fig. 4.22. (b)

Fig. 4.22. (a) The actual and reference values of d-q axis components of grid-utility currents; (b) zoom around the reference value

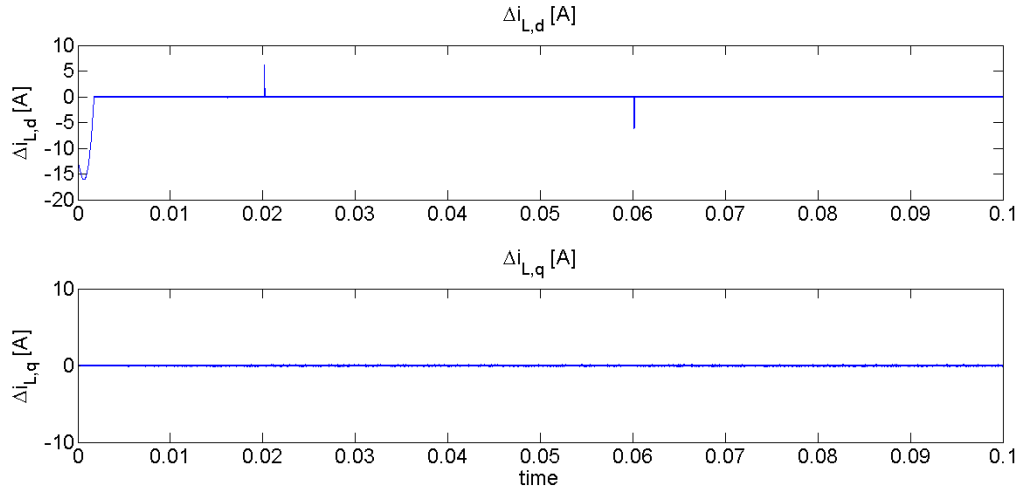


Fig. 4.23. (a)

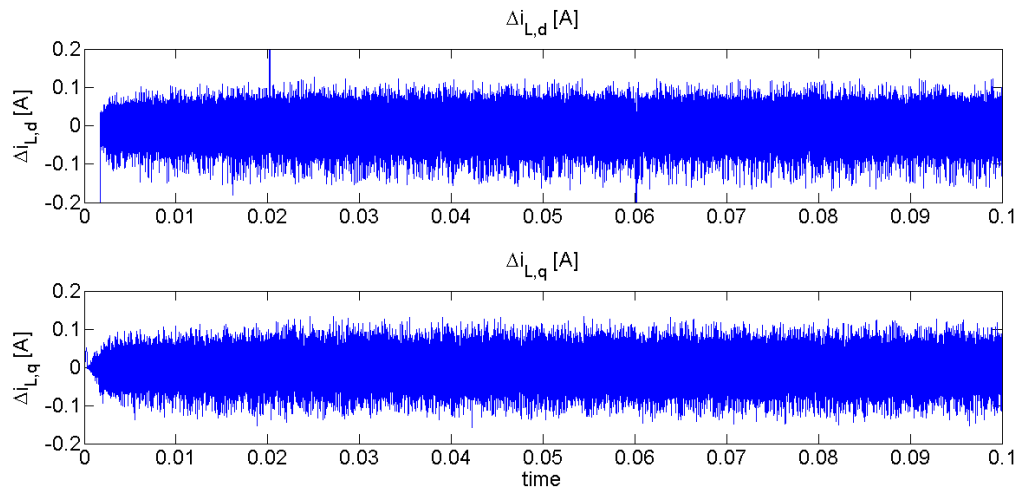


Fig. 4.23. (b)

Fig. 4.23. (a) The errors of d-q axis components of grid-utility currents;
(b) details of the steady-state

The proposed control strategy of the Stage 2 is able to follow the step-change of the reference instantaneous active value providing the reference reactive power at same time as depicted in Fig. 4.24.

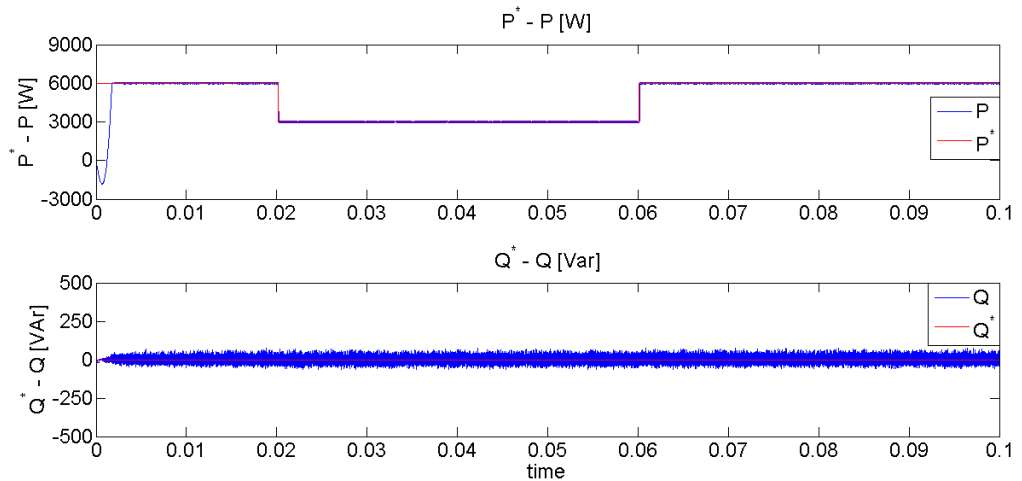


Fig. 4.24. (a)

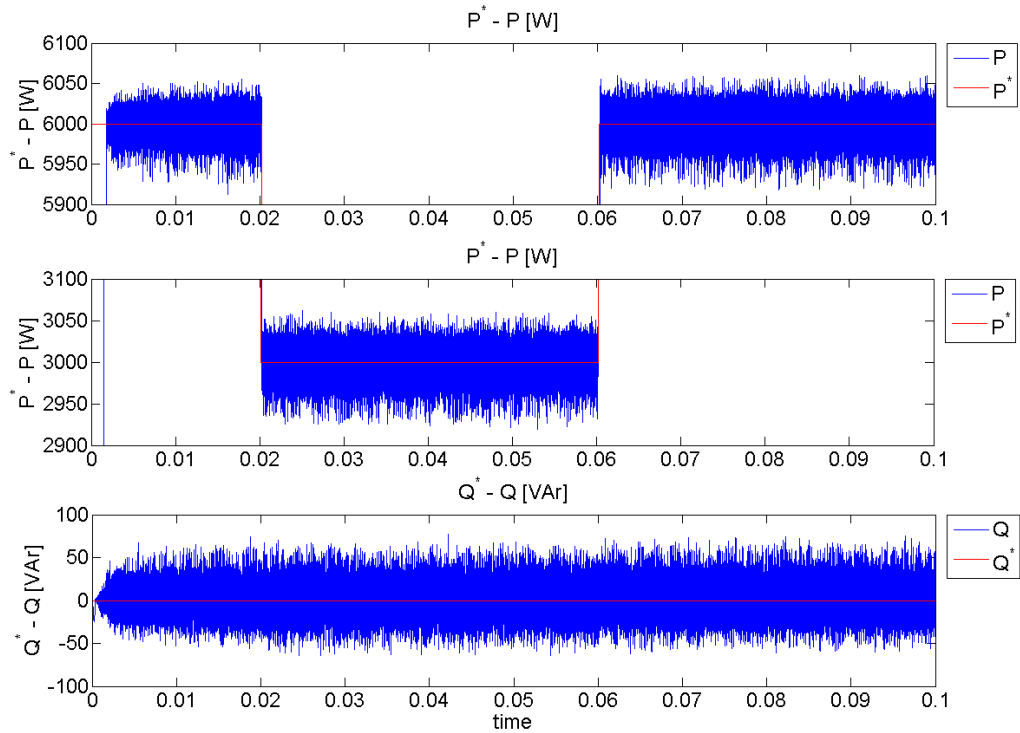


Fig. 4.24. (a) The actual and reference values of the active and reactive power; (b) zoom around the reference values

Since the reactive power reference is set to zero, the phase displacement between the phase voltages and currents on the grid-utility is always equal to zero as shown in Fig. 4.25., where the zero of the d-q axis components of the grid currents has been translated to the value of -20 A on the ordinate axis to represent these on the same figure.

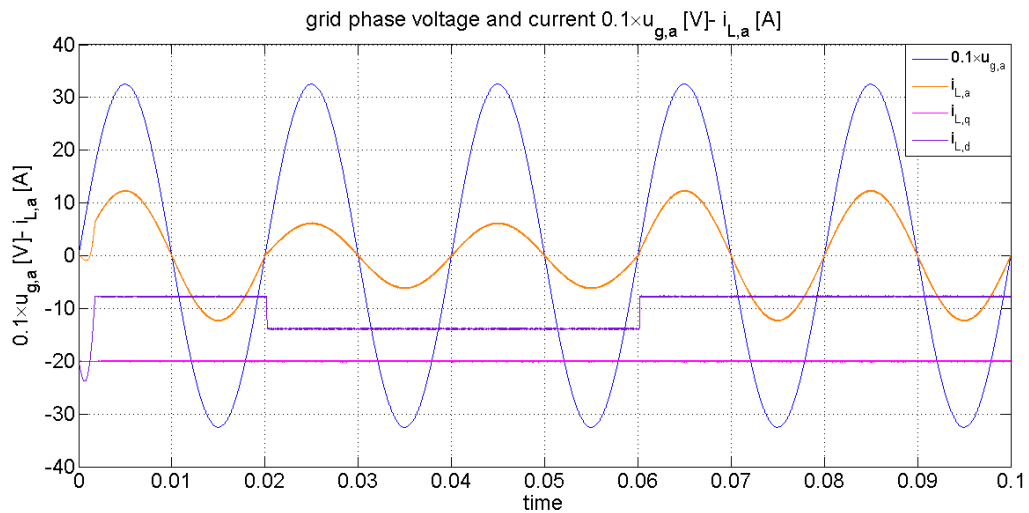


Fig. 4.25. The phase voltage and current of the grid.

The resonant frequency of quasi-resonant branch has been fixed equal to 80 kHz as shown in Fig. 4.26.

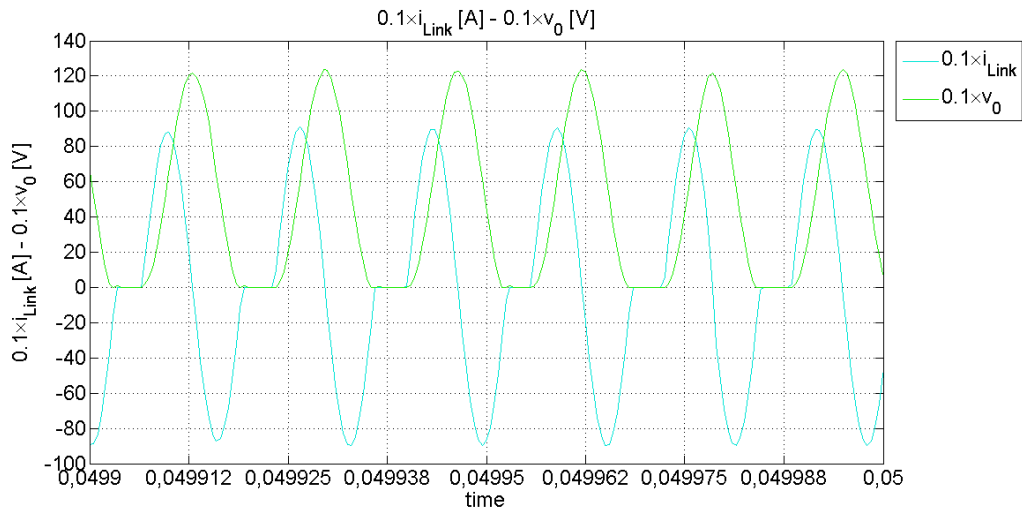


Fig. 4.26. The Dc-link current and the resonant capacitor voltage as time functions.

Fig. 4.27 proves that the errors of the d-q axis components of the grid-utility currents tend to sliding manifold with a small mean values that is shown in Fig. 4.28.

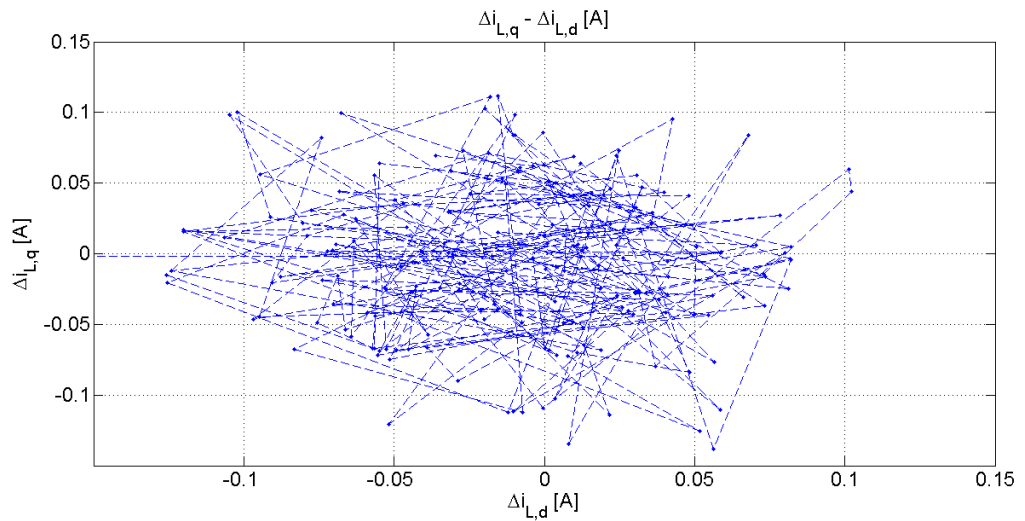


Fig. 4.27. The errors of d-q axis components of the grid currents in the phase space.

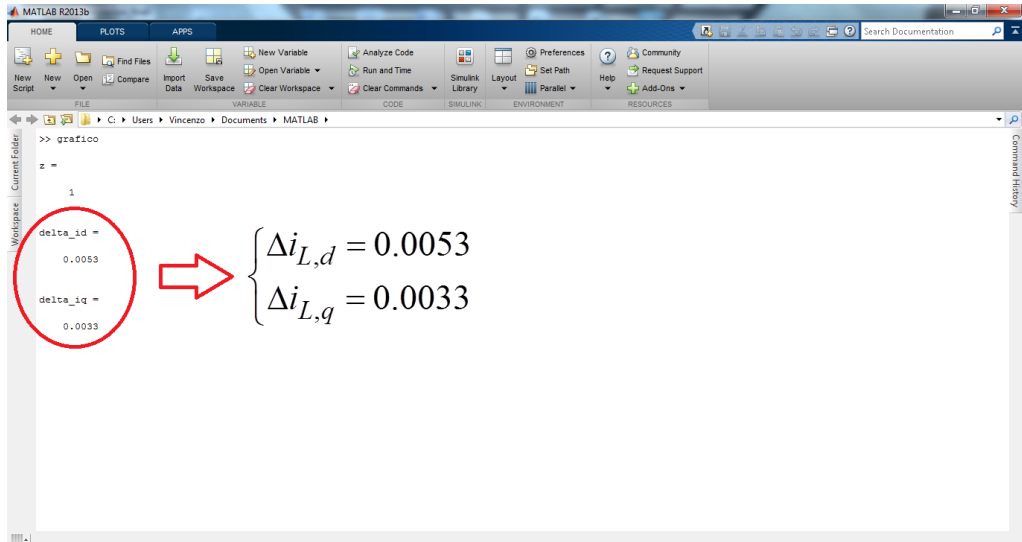


Fig. 4.28. The mean values of the errors of d-q axis components of the grid currents.

4.1.3. Simulation 3: $P^* = 3\text{kW}$; $Q^* = 0 \div 3\text{kVAr}$ ($v_{dc}^* = 600\text{V}$)

Under balanced condition of the grid utility may be possible to generate a desired instantaneous reactive power in order to provide ancillary services to grid operator. For this reason a simulation with variable reference value of reactive power was carried out.

So the reference reactive power Q^* is step-changed at 0.02 s from 0 kVAr to 3 kVAr (corresponding to a reference q-axis current component $i_{L,q}^*$ of -6.15 A) during a time of 300 μs and then backed to 0 kVAr (corresponding to a reference q-axis current component $i_{L,q}^*$ of 0 A) at 0.06 s during the same time of 300 μs , while the reference active power is contextually fixed to 3 kW (corresponding to a reference d-axis current component $i_{L,d}^*$ of 6.15 A).

The reference values of the DSACPC control strategy are given in Table 4.4:

TABLE 4.4: REFERENCE VALUES OF SIMULATION 3

DSACPC Stage	Parameters	Values
<i>Stage 1</i>	Rated speed	4500 rpm
	DC-link voltage v_{dc}^*	600 V
<i>Stage 2</i>	Instantaneous active power P^*	3 kW
	Instantaneous reactive power Q^*	0÷3 VAr

STAGE 1

The actual and observed electrical rotor angle of PMSG with respect to its actual value as show in Fig. 4.29.

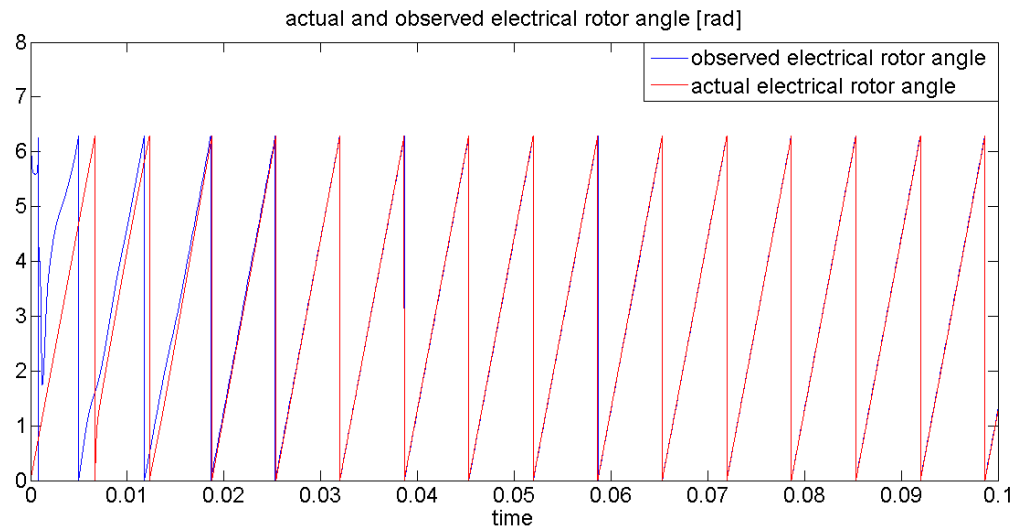


Fig. 4.29. Actual and estimated electrical rotor angle of PMSG at 4500 rpm.

The observed back-EMFs of PMSG are shown in the Fig. 4.30, while the back-EMF phase is compared with its actual value in the Fig. 4.31.

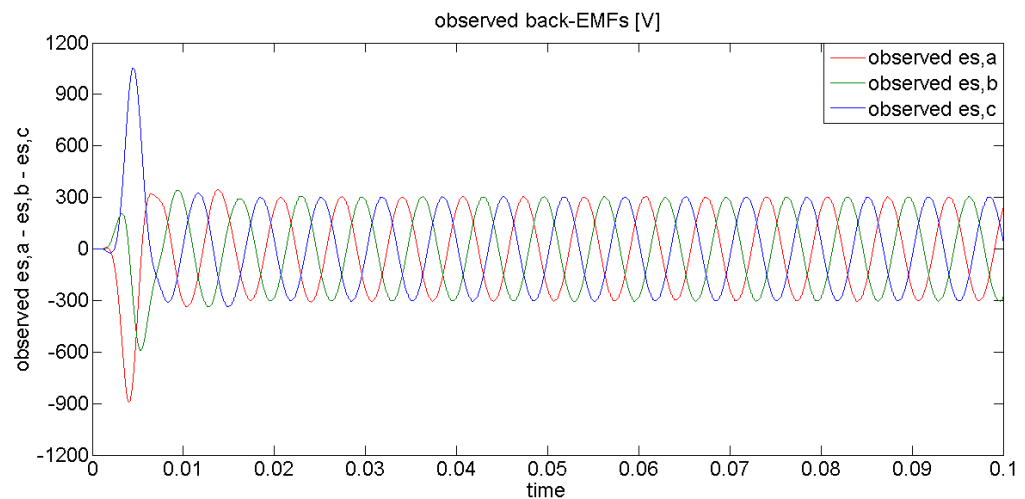


Fig. 4.30. (a)

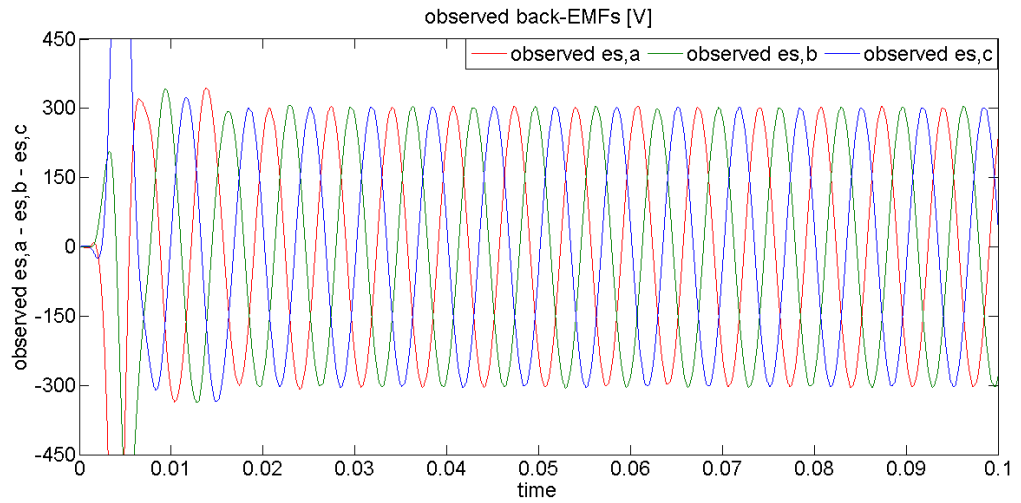


Fig. 4.30. (a) Observed back-EMFs of PMSG; (b) details of the steady-state.

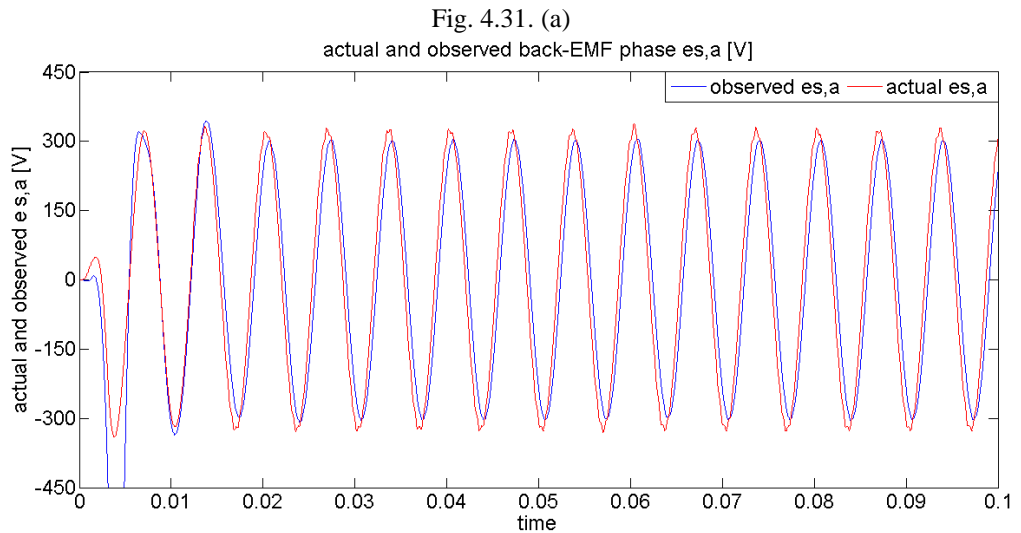
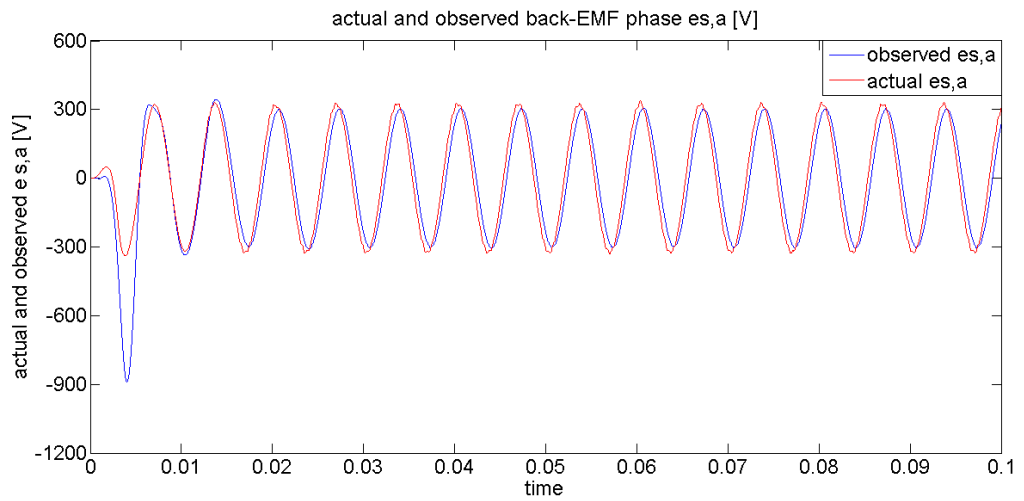


Fig. 4.31. (a) Actual and observed back-EMF phase of PMSG; (b) zoom around the actual value.

Fig. 4.32 and 4.33 show the errors of d-q axis components of PMSG stator currents and the actual and reference value of the DC-link voltage in order to prove the performance of the control of the Stage 1.

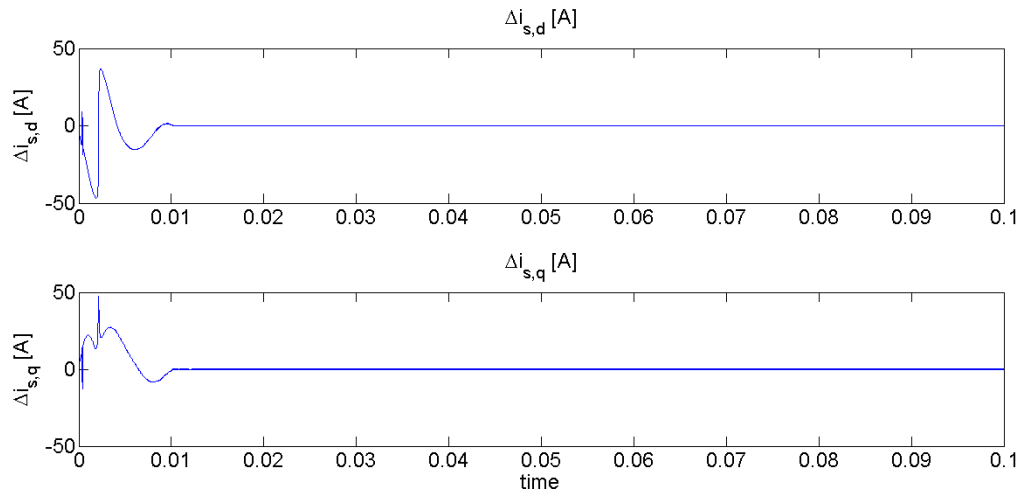


Fig. 4.32. (a)

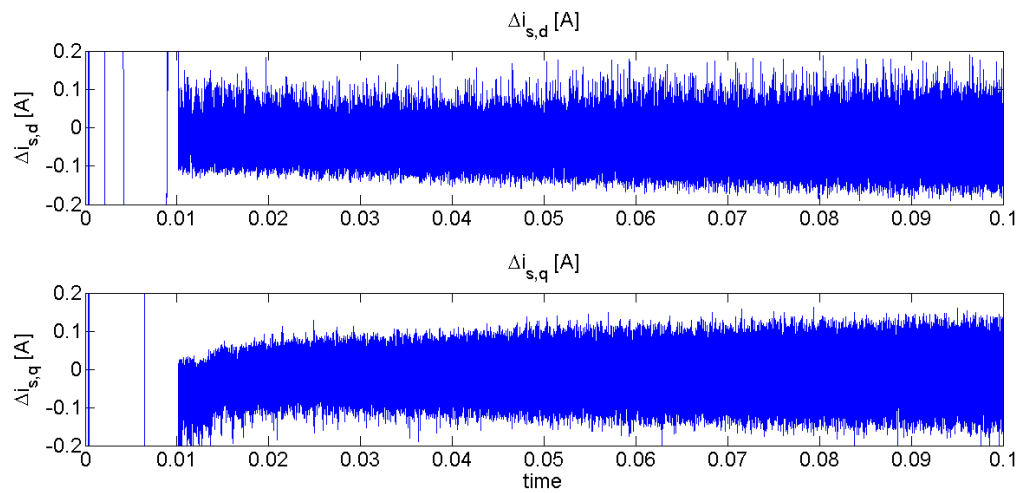


Fig. 4.32. (b)

Fig. 4.32. (a) the errors of d-q axis components of PMSG stator currents;
(b) details of the steady-ste.

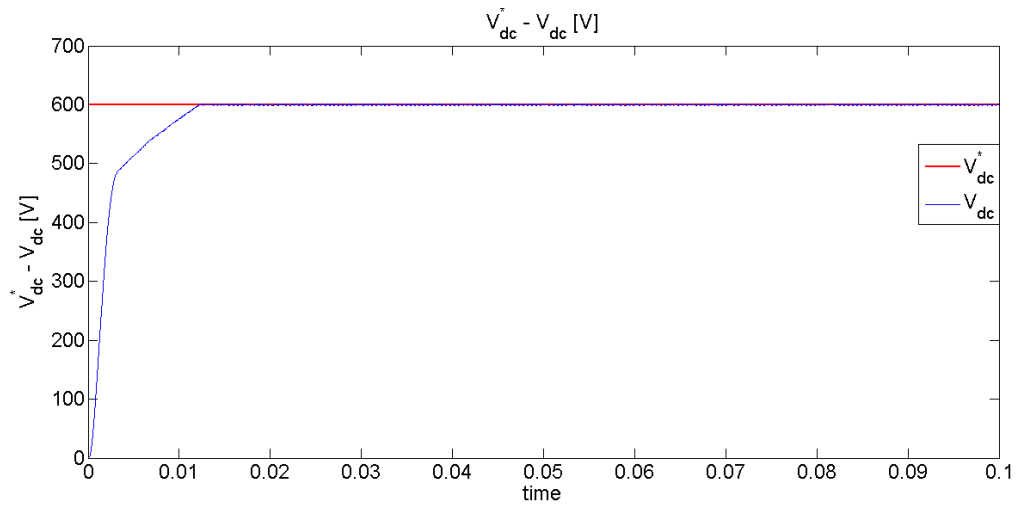


Fig. 4.33. (a)

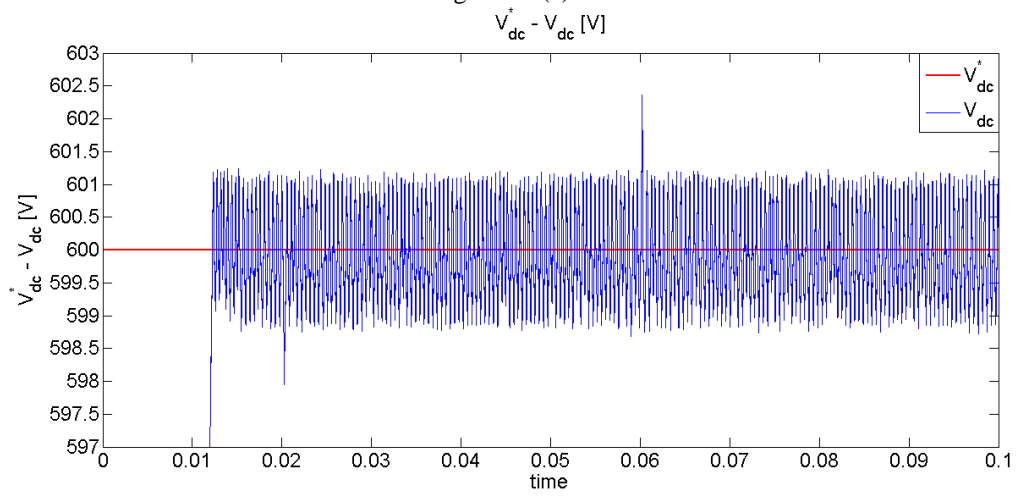


Fig. 4.33. (b)

Fig. 4.33. (a) The actual and reference value of the DC-link voltage;
(b) zoom around the reference value.

STAGE 2

The grid-utility voltages are shown in Fig. 4.34 under balanced condition of the grid.

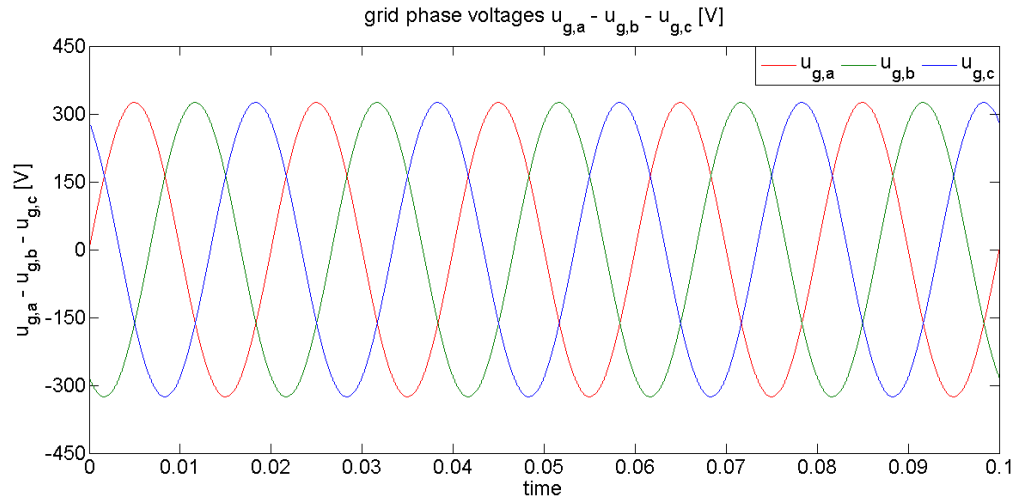


Fig. 4.34. The grid-utility voltages.

The grid-side inverter currents are shown in Fig. 4.35 when the actual d-q axis components of the grid-utility currents follows their reference value with small errors as shown in Fig. 4.36 and 4.37 respectively.

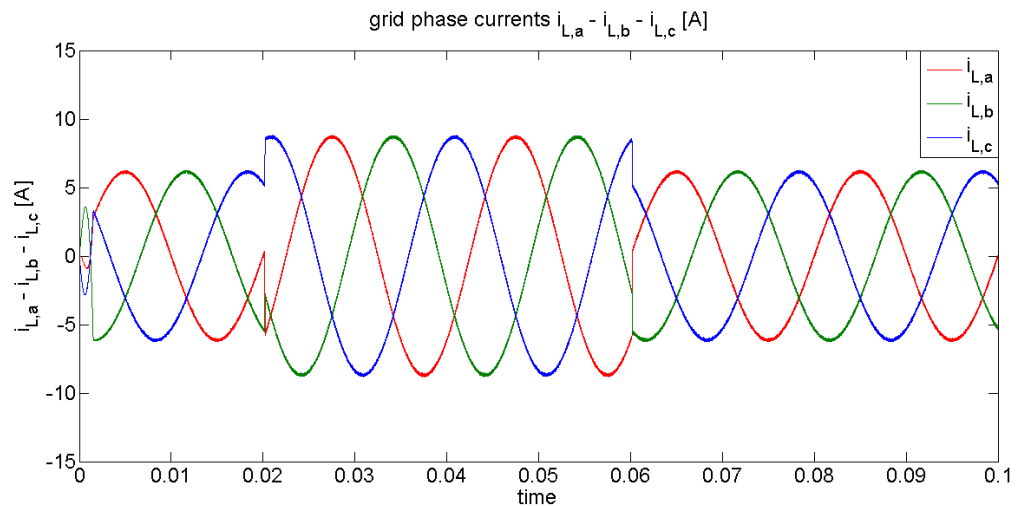


Fig. 4.35. The grid-side inverter currents.

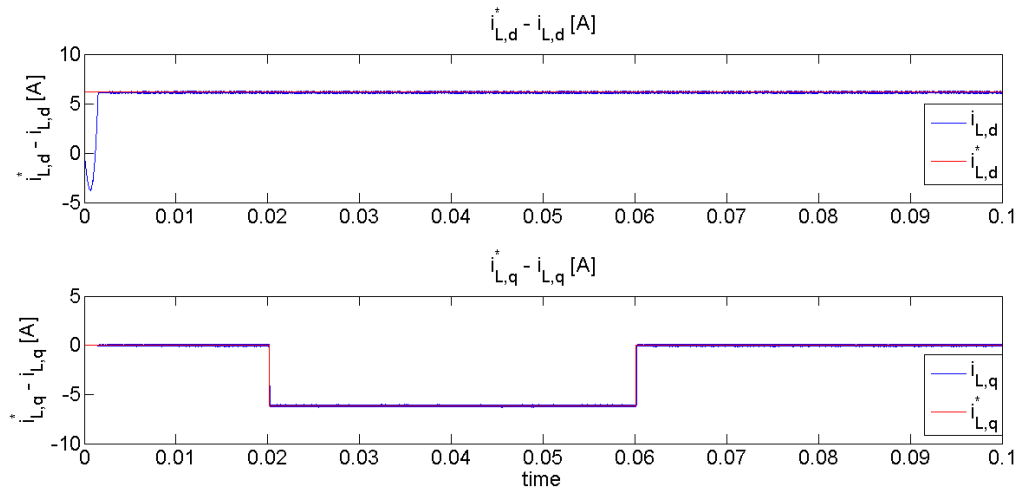


Fig. 4.36. (a)

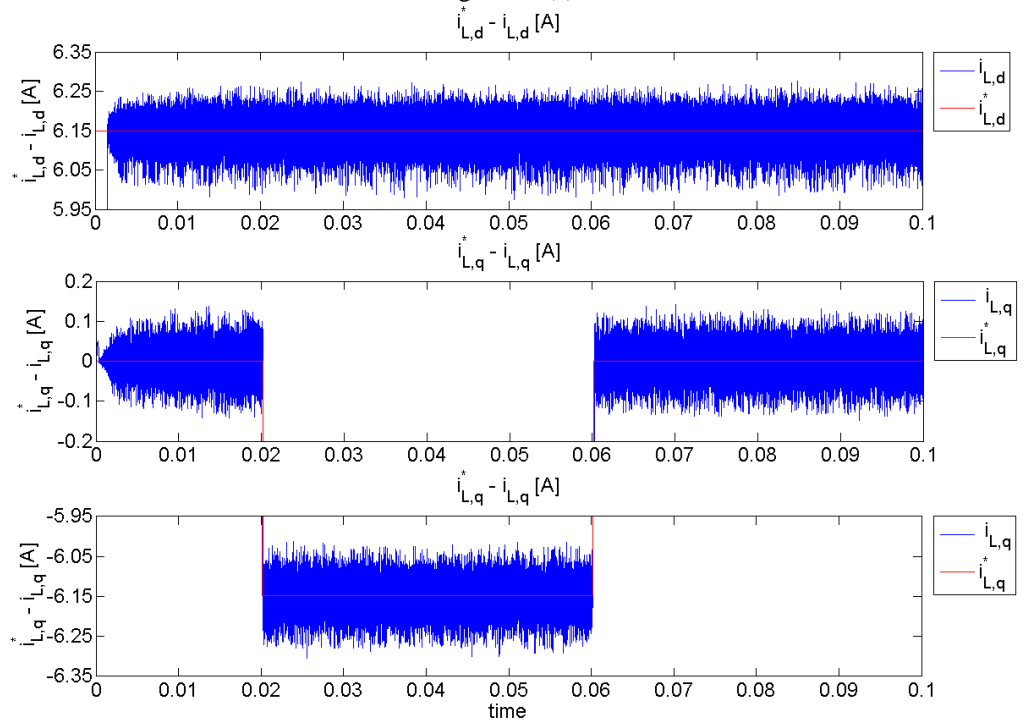


Fig. 4.36. (b)

Fig. 4.36. (a) The actual and reference values of d-q axis components of grid-utility currents; (b) zoom around the reference values.

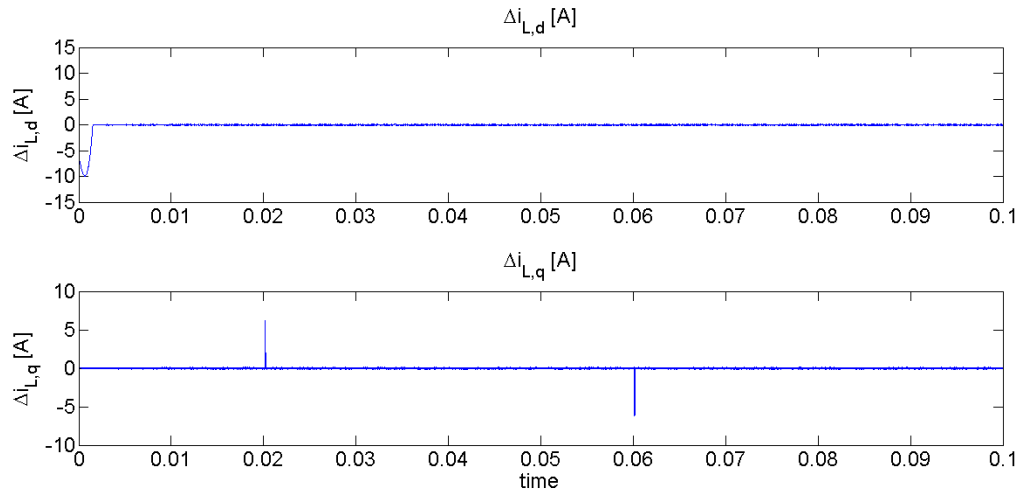


Fig. 4.37. (a)

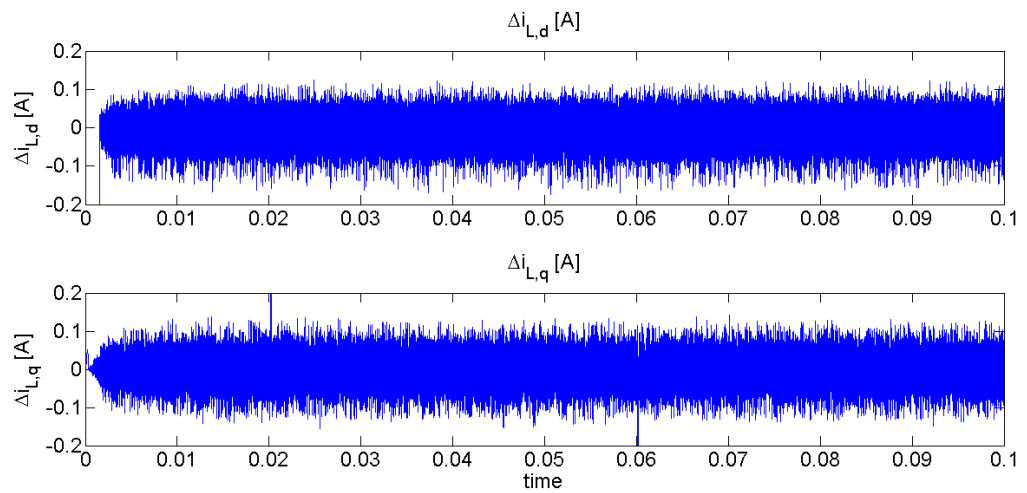


Fig. 4.37. (b)

Fig. 4.37. (a) The errors of d-q axis components of grid-utility currents;
(b) details of the steady-state.

The proposed control strategy of the Stage 2 is able to guarantee the reaching of the fixed reference reactive power value without to influence the active power generation also during the time interval of its variation as depicted in Fig. 4.38.

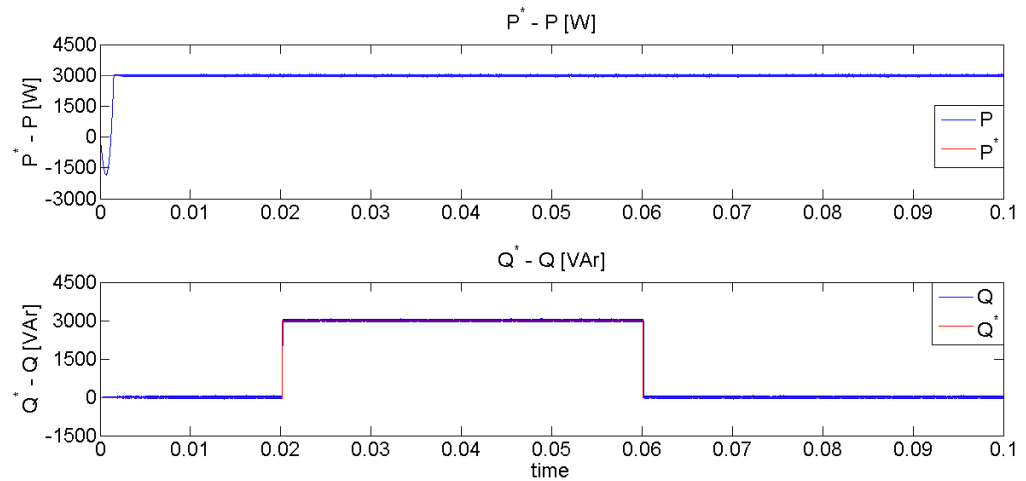


Fig. 4.38. (a)

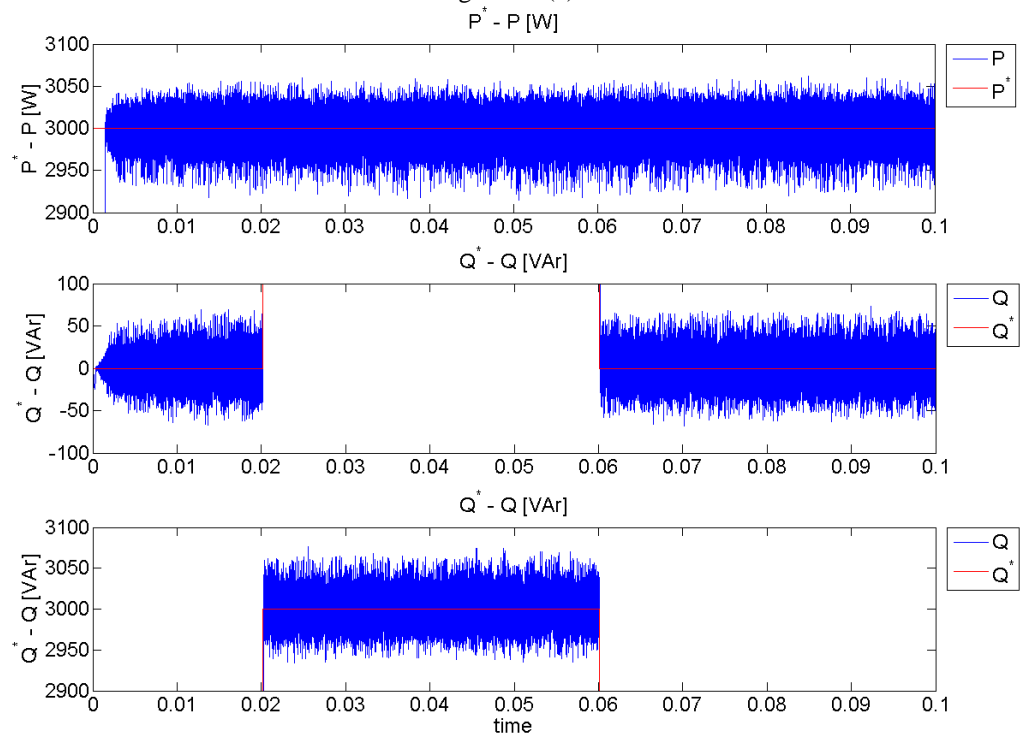


Fig. 4.38. (b)

Fig. 4.38. (a) The actual and reference values of the active and reactive power;
(b) zoom around the references values.

The phase displacement between the phase voltages and currents on the grid-utility is not equal to zero during the reactive power generation as shown in Fig. 4.39., where the zero of the d-q axis components of the grid currents has been translated to the value of -20 A on the ordinate axis to represent these on the same figure.

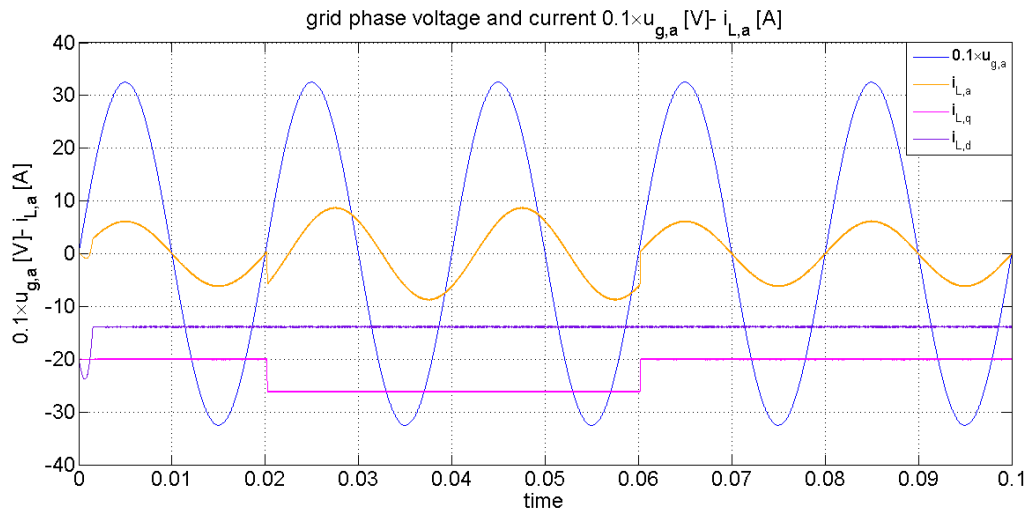


Fig. 4.39. The phase voltage and current of the grid.

The next figure shows the DC-link current and the resonant capacitor voltage for a fixed resonant frequency of 80 kHz.

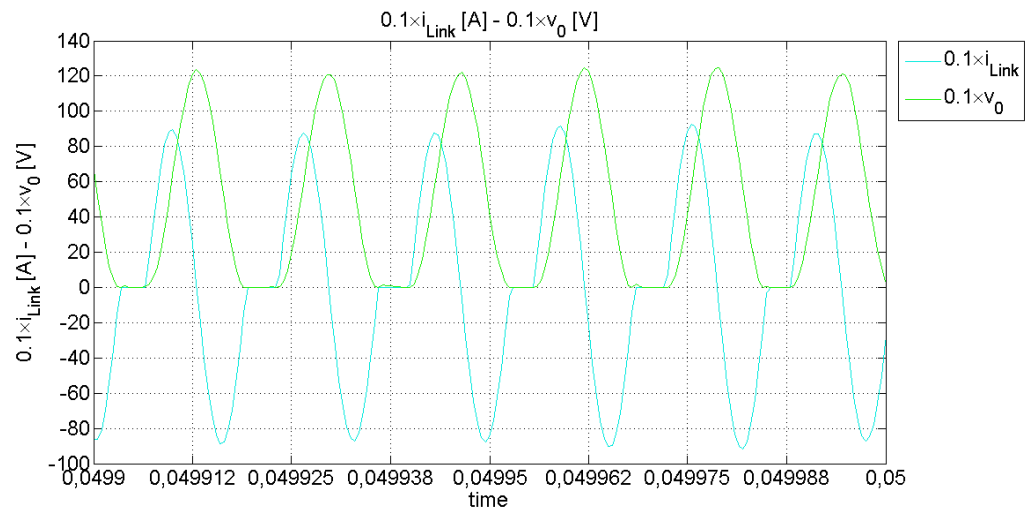


Fig. 4.40. The Dc-link current and the resonant capacitor voltage as time functions.

The reaching of the sliding manifold is guaranteed with reduced mean values of the errors of the d-q axis components of the grid-utility currents as shown in Fig. 4.41 and Fig.4.42.

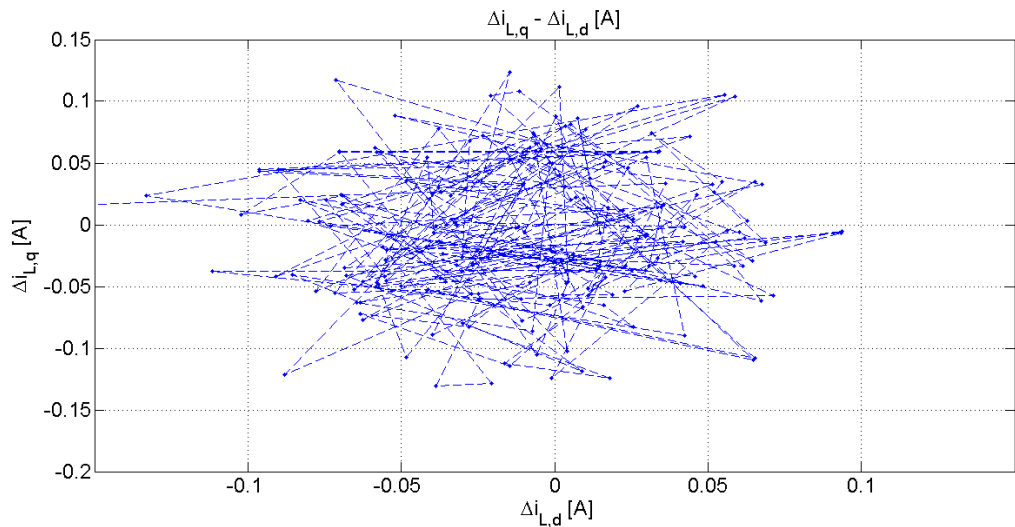


Fig. 4.41. The errors of d-q axis components of the grid currents in the phase space.

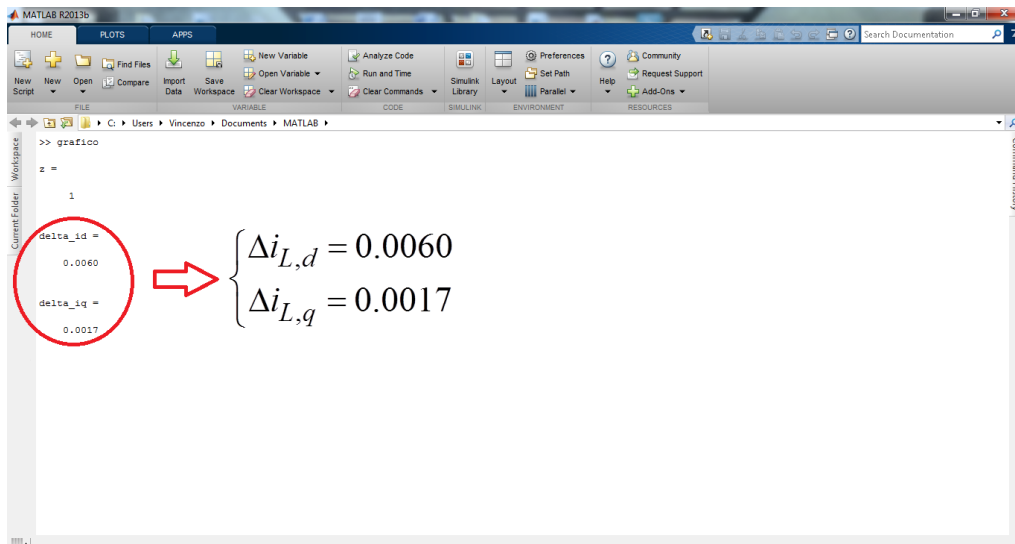


Fig. 4.42. The mean values of the errors of d-q axis components of the grid currents.

4.1.4. Simulation 4: $i_{L,d}^* = 6.15 \text{ A}$; $i_{L,q}^* = 0 \text{ A}$ ($v_{dc}^* = 600 \div 500 \text{ V}$)

The last simulation was carried out in order to prove the robustness of the proposed control strategy under unbalanced grid-utility conditions. So a 5-th and 7-th harmonic voltages have been added to the three-phase sinusoidal grid-voltage and the reference values of d-q axis current component of Stage 2 have been fixed to 6.15 A and 0 A respectively; moreover the reference value of the DC-Link voltage is step-changed at 0.02 s from 600 V to 500 V during an

interval time of 300 μ s and then backed to 600 V at 0.06 s during the same interval time of 300 μ s.

The reference values of the DSACPC control strategy are given in Table 4.5:

TABLE 4.5: REFERENCE VALUES OF SIMULATION 4

DSACPC Stage	Parameters	Values
<i>Stage 1</i>	Rated speed	4500 rpm
	DC-link voltage v_{dc}^*	600÷500 V
<i>Stage 2</i>	reference d-axis current component $i_{L,d}^*$	6.15 A
	reference q-axis current component $i_{L,q}^*$	0 A

STAGE 1

The observed electrical rotor angle of PMSG follows its actual values as shown in Fig. 4.43.

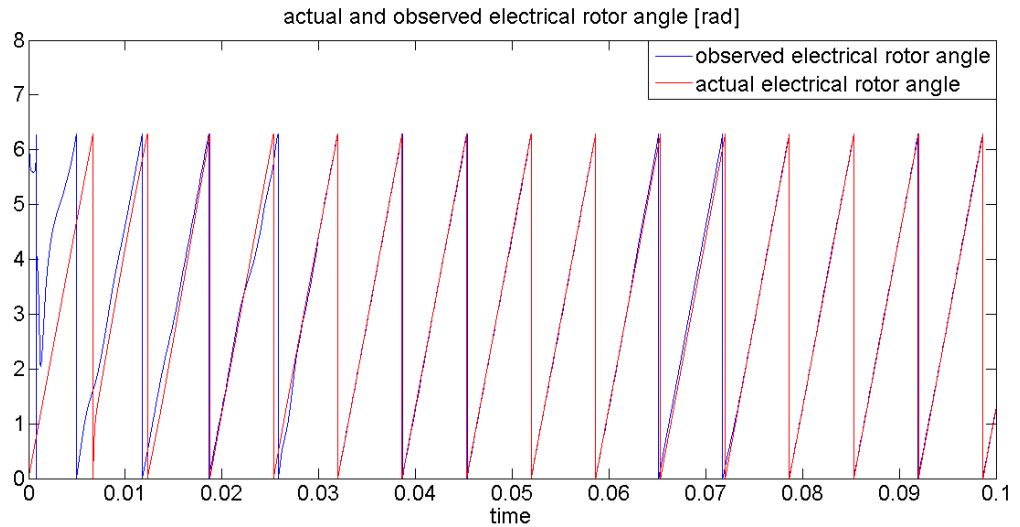


Fig. 4.43. Actual and estimated electrical rotor angle of PMSG at 4500 rpm.

The same tracking occurs for the observed back-EMFs of PMSG with respect to their actual values are shown in the Fig. 4.44 and Fig. 4.45.

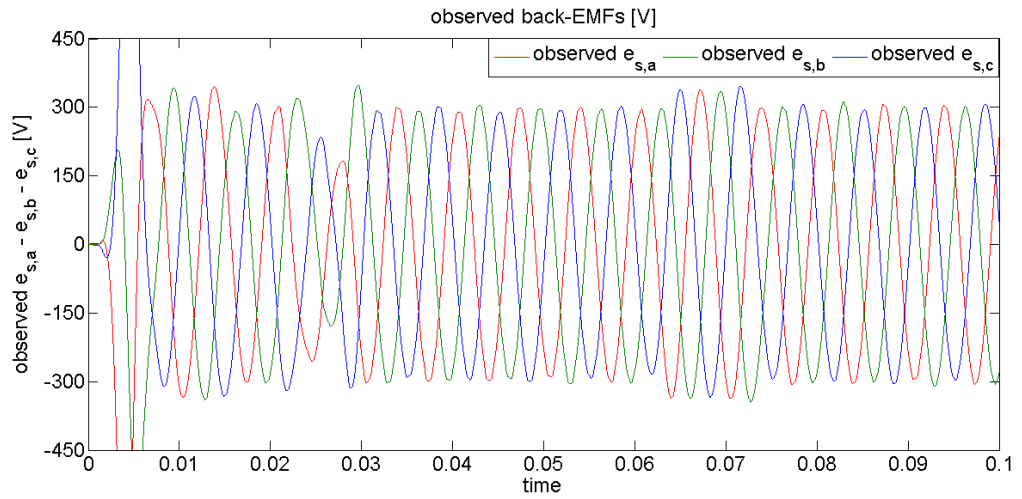


Fig. 4.44. (a)

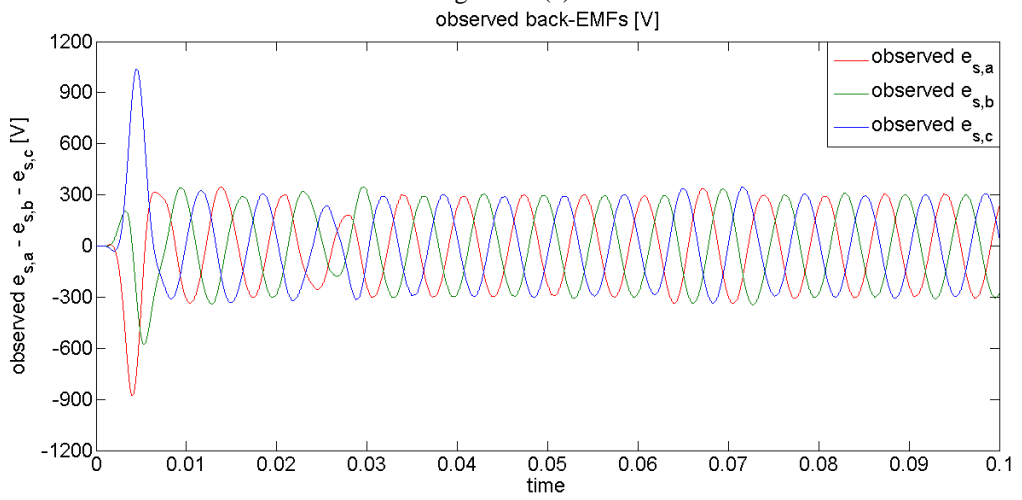


Fig. 4.44. (b)

Fig. 4.44. (a) Observed back-EMFs of PMSG; (b) details of the steady-state.

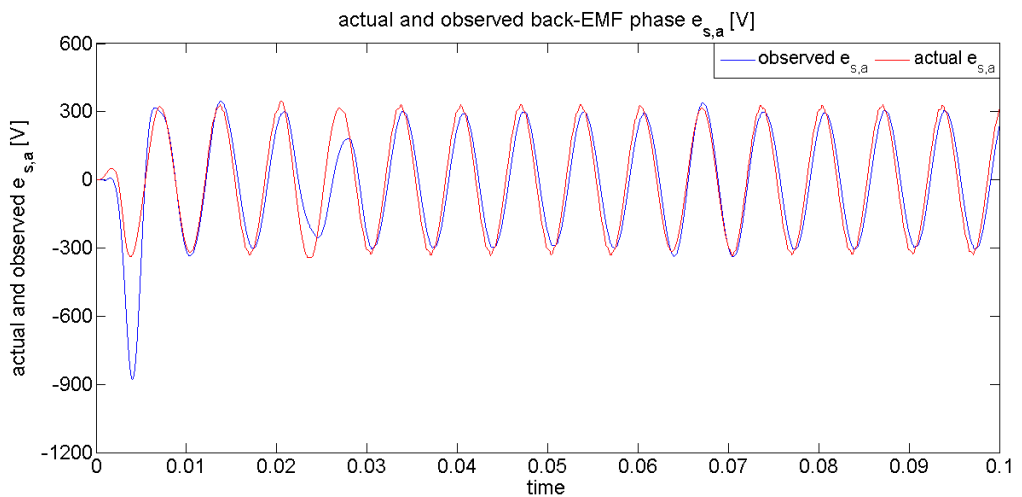


Fig. 4.45. (a)

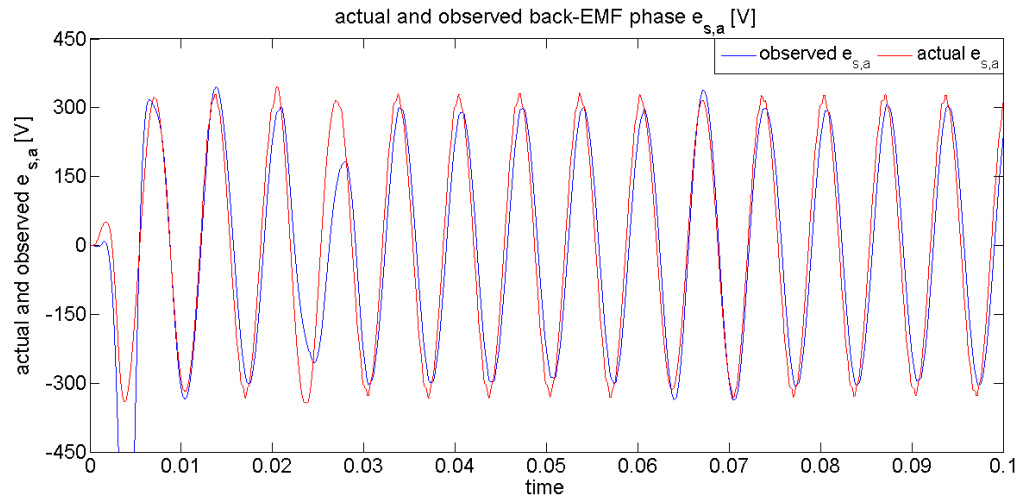


Fig. 4.45. (b)

Fig. 4.45. (a) Actual and observed back-EMF phase of PMSG;
(b) zoom around the actual value.

The proposed control strategy of Stage 1 is able to guarantee small errors of d-q axis components of PMSG stator currents and the reaching of the reference value of the DC-link voltage also under unbalanced condition of the grid-utility as shown in Fig. 4.46. and Fig. 4.47.

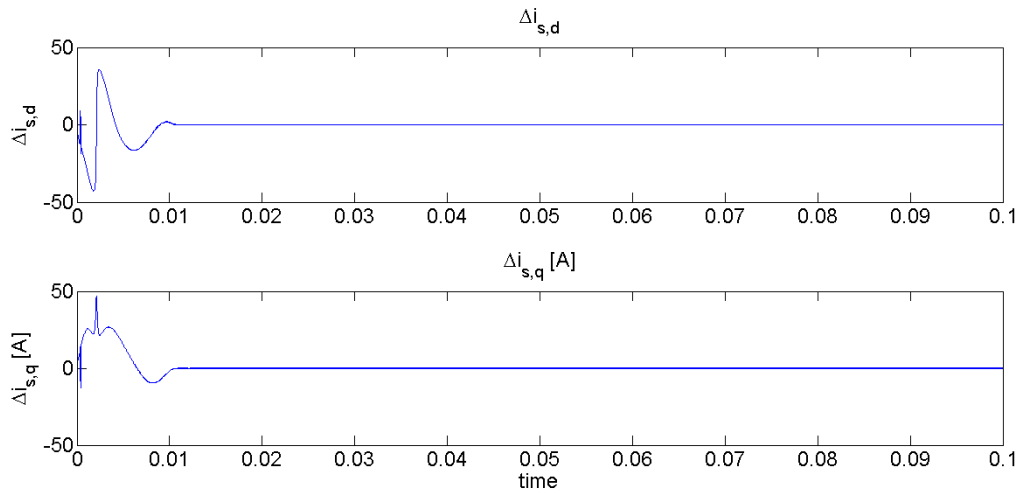


Fig. 4.46. (a)

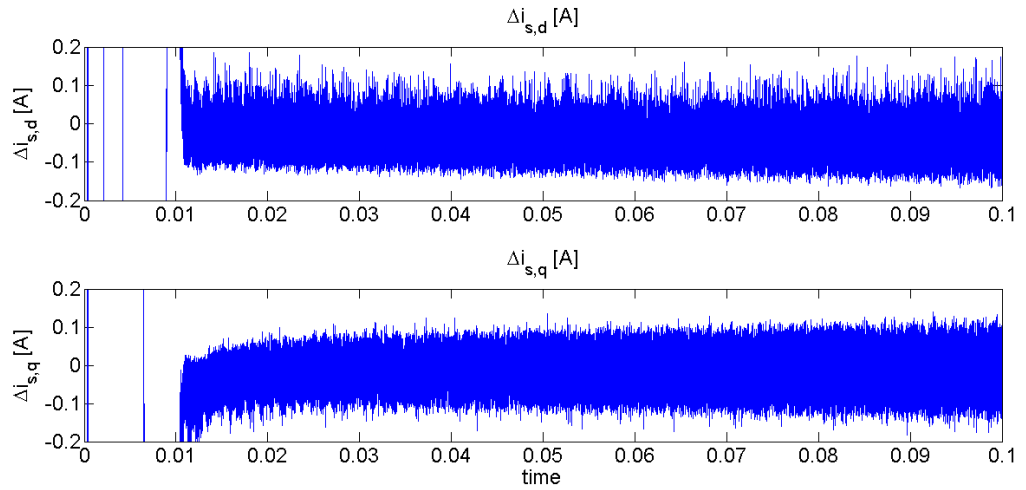


Fig. 4.46. (a) The errors of d-q axis components of PMSG stator currents;
(b) details of the steady-state.

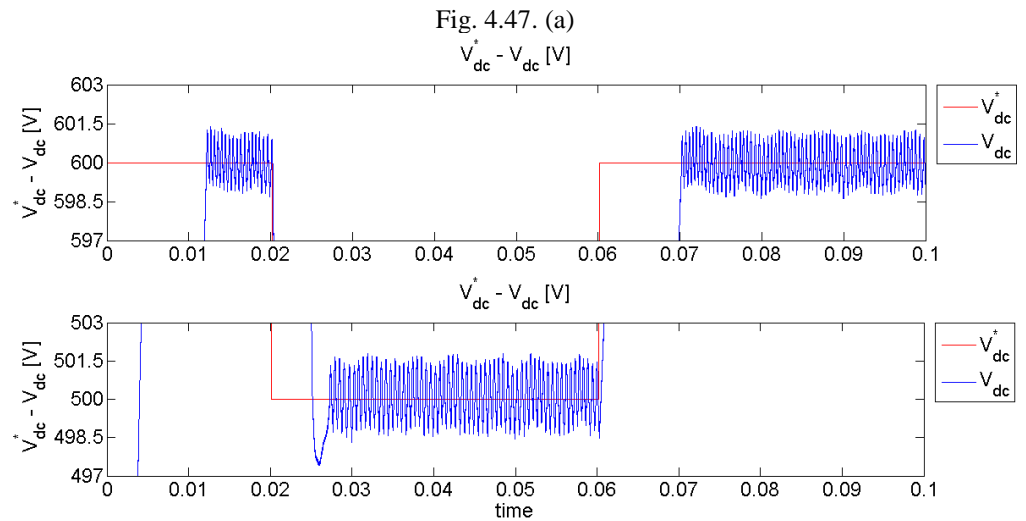
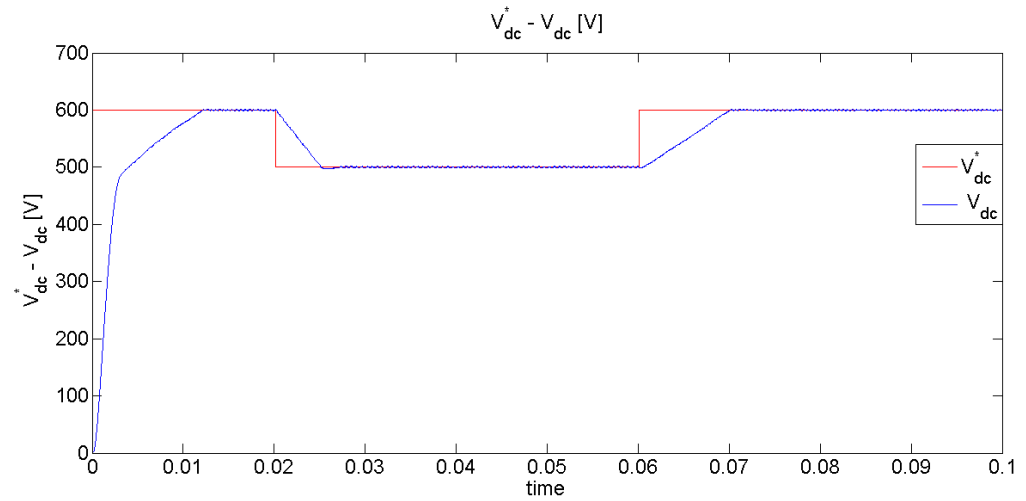


Fig. 4.47. (a) The actual and reference value of the DC-link voltage;
(b) zoom around the reference value.

STAGE 2

The grid-utility voltages under unbalanced conditions are shown in Fig. 4.48.

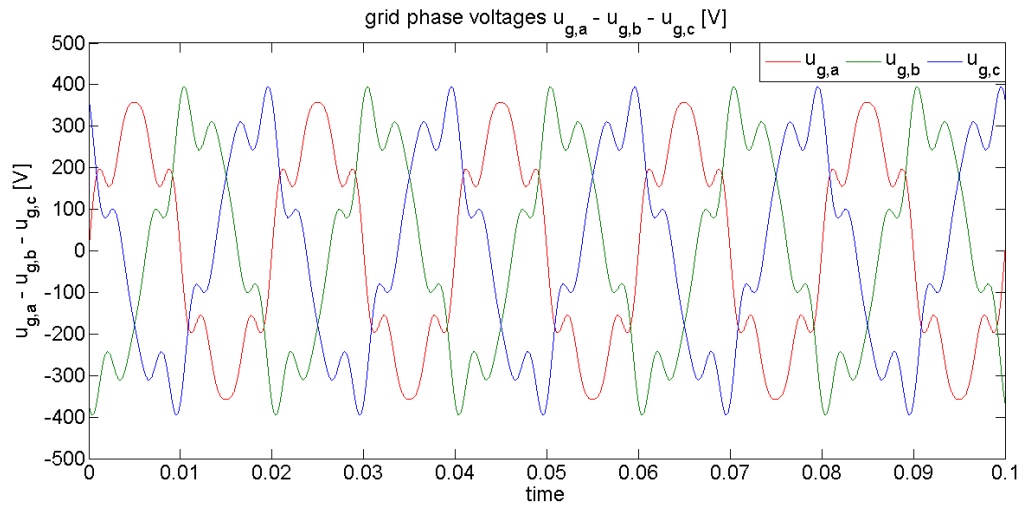


Fig. 4.48. The grid-utility voltages.

In this case the proposed control strategy of Stage 2 is able to achieve a current harmonic rejection of the grid phase currents as depicted in Fig. 4.49.

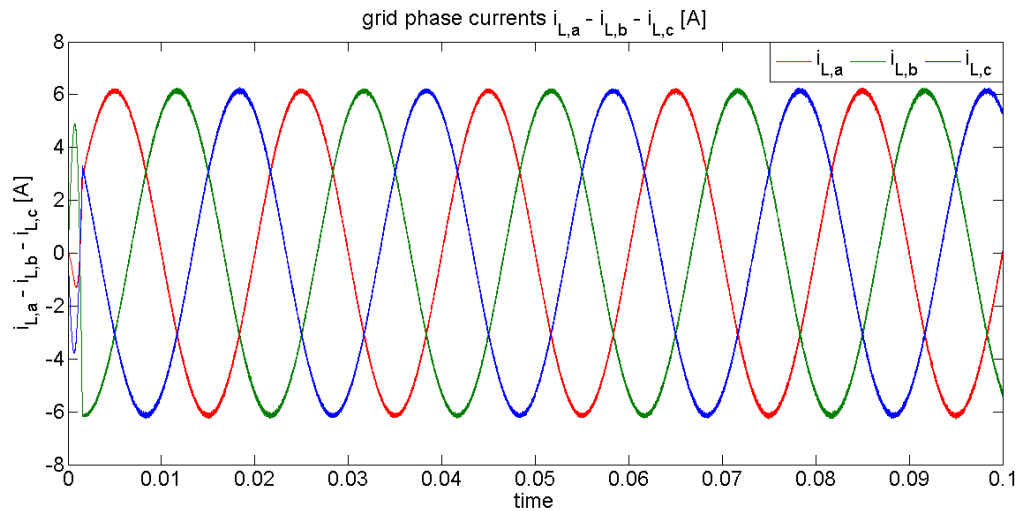


Fig. 4.49. The grid-side inverter currents.

The actual d-q axis components of the grid-utility currents follows their reference values as shown in Fig. 4.50 and small steady-state errors as shown in Fig. 4.51.

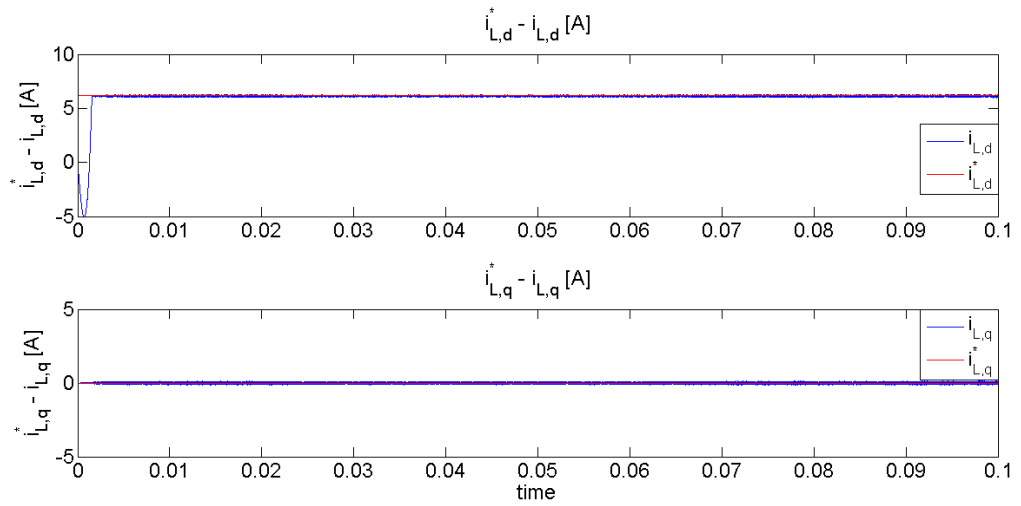


Fig. 4.50. (a)

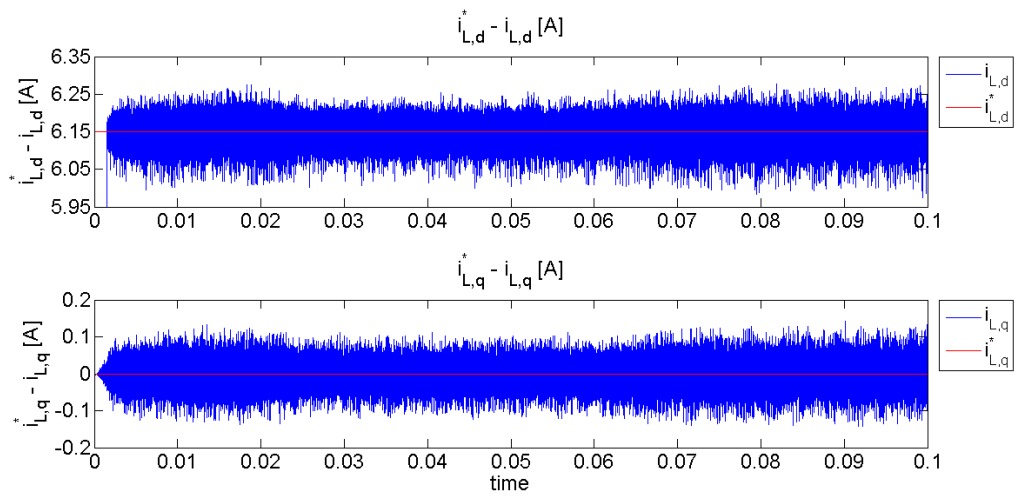


Fig. 4.50. (b)

Fig. 4.50. (a) The actual and reference values of d-q axis components of grid-utility currents; (b) zoom around the reference values.

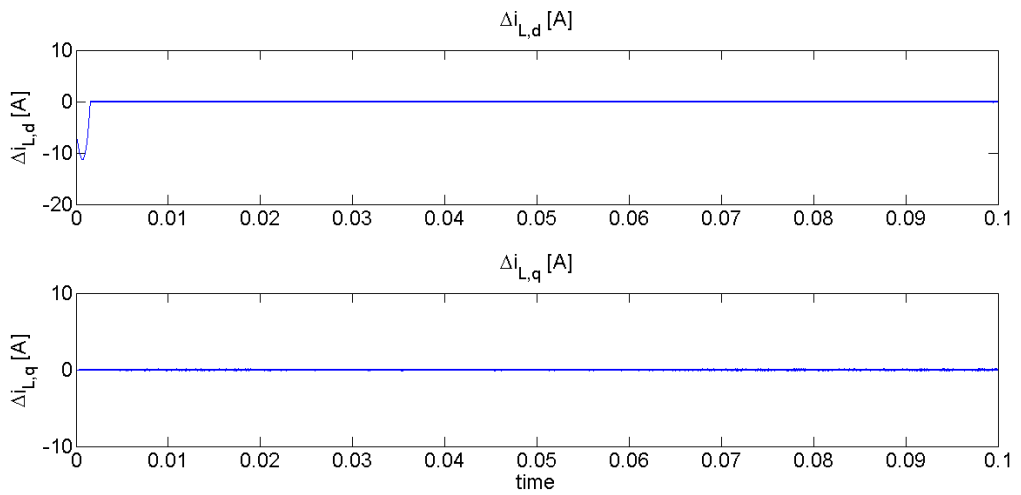


Fig. 4.51. (a)

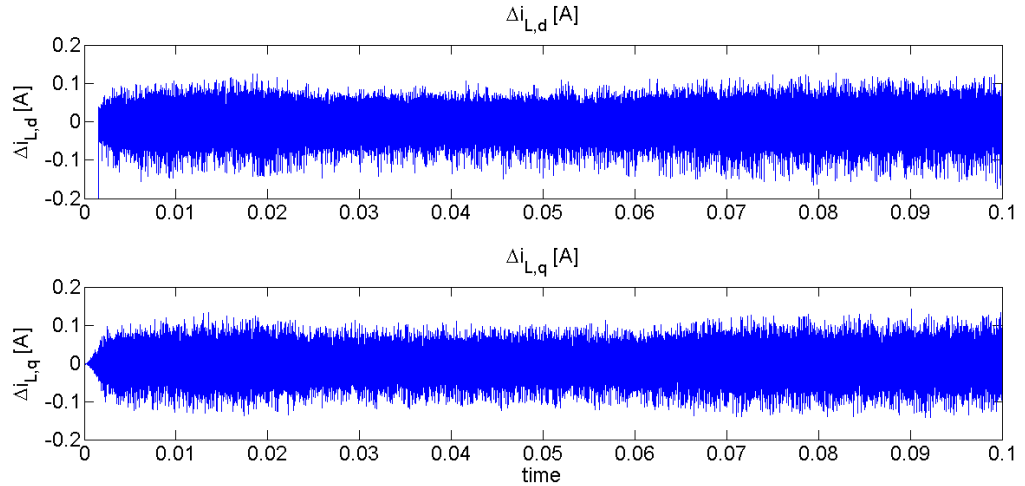


Fig. 4.51. (a) The errors of d-q axis components of grid-utility currents;
(b) details of the steady-state.

Under unbalanced conditions of the grid utility, the power is deformed as demonstrated in the next figure.

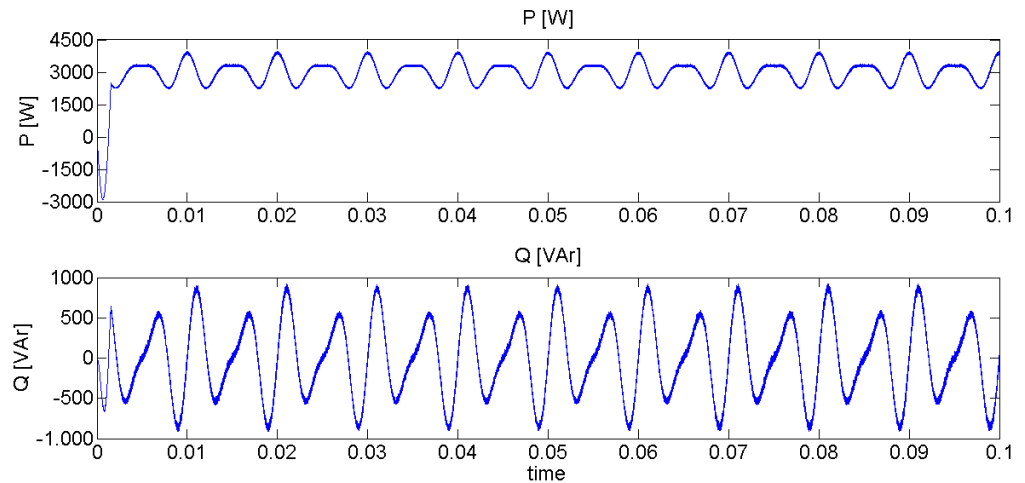


Fig. 4.52. The actual values of the instantaneous active and reactive power.

Since the reference value of the d-axis current component is fixed to zero ($i_{L,d}^* = 0\text{ A}$), the phase displacement between the phase voltages and currents on the grid-utility is always equal to zero as shown in Fig. 4.53., where the zero of the d-q axis components of the grid currents has been translated to the value of -20 A on the ordinate axis to represent these on the same figure.

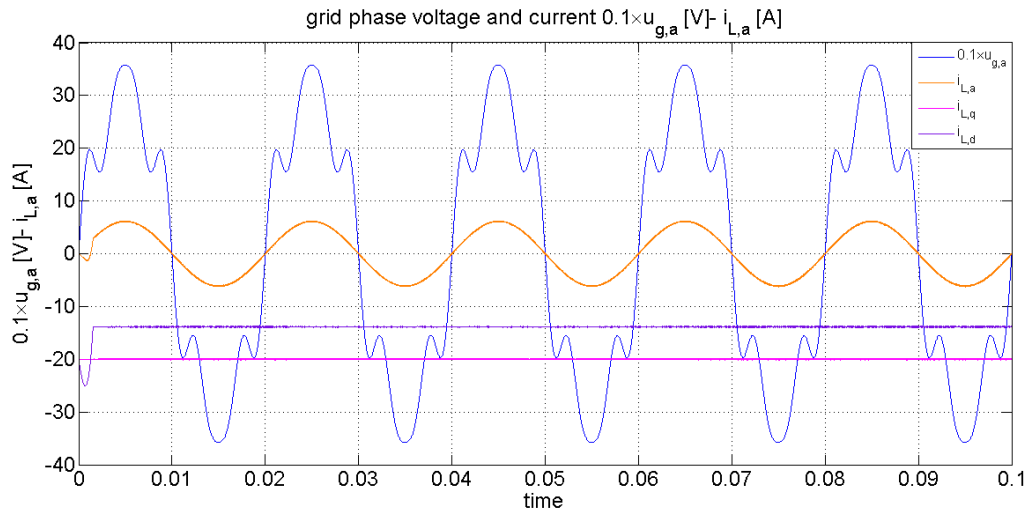


Fig. 4.53. The phase voltage and current of the grid.

The resonant frequency has been fixed equal to 80 kHz and the trend of the DC-link current and the resonant capacitor voltage are insensible with respect to unbalanced conditions of grid-utility as shown in Fig. 4.54.

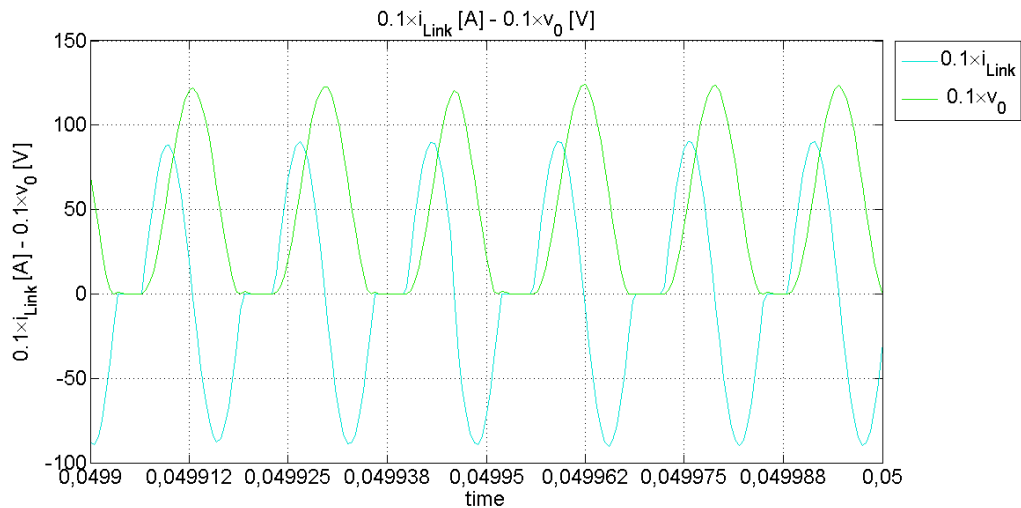


Fig. 4.54. The Dc-link current and the resonant capacitor voltage as time functions.

Also under unbalanced conditions of the grid-utility the sliding mode occurs with small mean values of the errors of the d-q axis components of the grid-utility currents as shown in Fig. 4.55 and Fig.4.56.

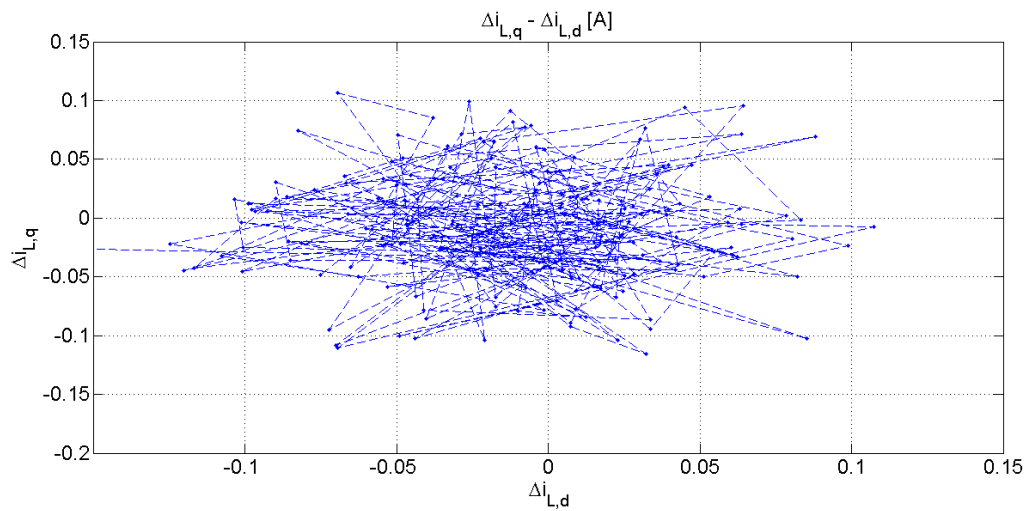


Fig. 4.55. The errors of d-q axis components of the grid currents in the phase space.

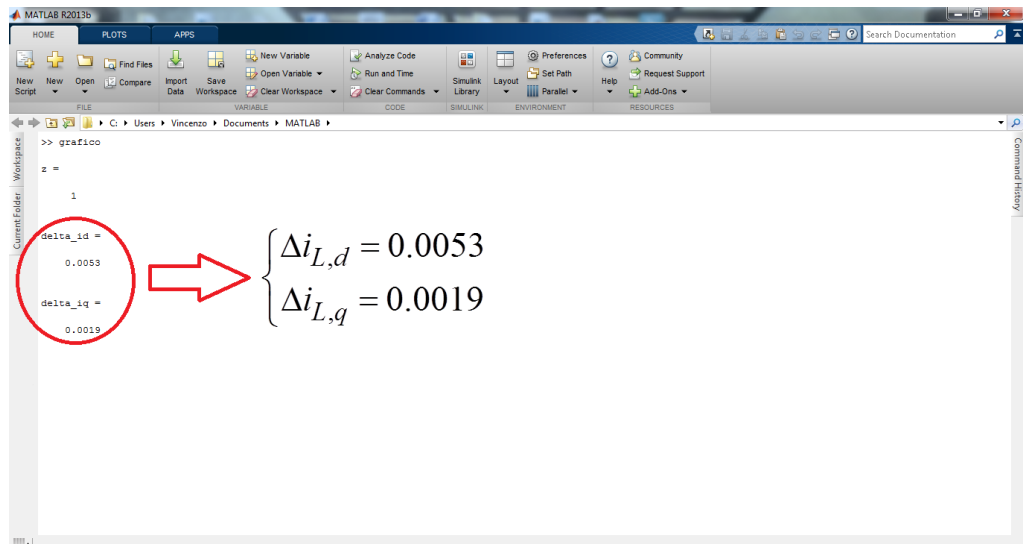


Fig. 4.56. The mean values of the errors of d-q axis components of the grid currents.

Discussion of numerical results

The simulation results prove the goodness of the proposed control strategy since the control strategy guarantees a fast response of the proposed electrical subsystem and the actual values of controlled variables have the ability of tracking their references with small errors. So the starting targets of the control strategy of both Stage 1 and Stage 2 of DSACPC are achieved under balanced and unbalanced conditions of the grid-utility.

4.2. Experimental Results

An experimental prototype has been arranged in order to validate the simulations results and thus the performance of the proposed control strategy. This prototype consists of a Permanent Magnet Synchronous Generator (PMSG) coupled with the grid-connected Double-Stage AC-AC Power Converter (DSACPC) that is composed by three-phase PWM rectifier, a DC-link capacitor filter, a three-phase soft-switched Voltage Source Inverter (VSI) and a three-phase step-up transformer connected to grid utility.

Fig. 4.57. shows the experimental prototype:

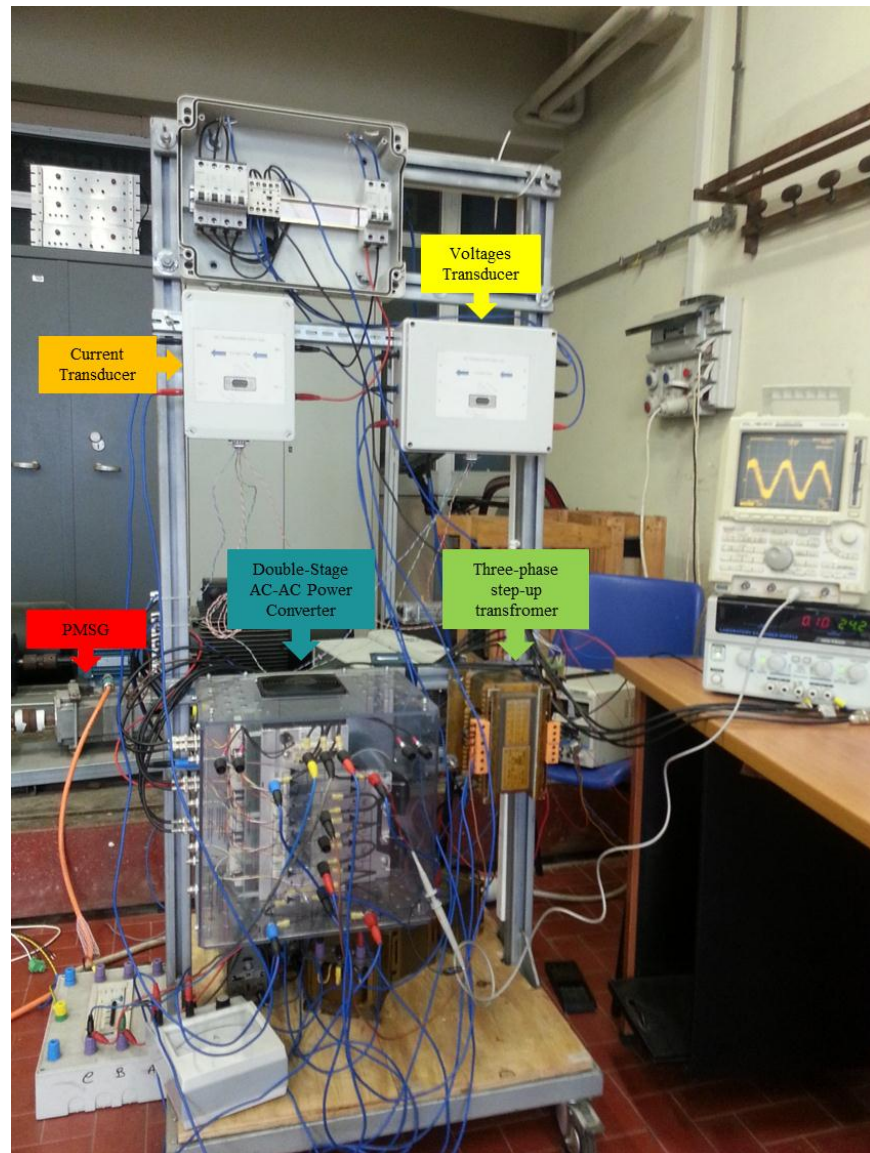


Fig. 4.57. Experimental prototype

The control strategy has been developed in Matlab/Simulink and implemented on DSP dSpace1103 Motorola PowerPC 60K 333 MHz.

The main specifications of the experimental prototype are listed in Table 4.6.

TABLE 4.6: SPECIFICATIONS OF THE EXPERIMENTAL PROTOTYPE

PMSG	Siemens 3-phase 1FT6-084-8SH7	
	Rated speed	4500 rpm
	Rated torque	20 Nm
	Rated power	9.42 kW
	Rated current	24.5 A
PWM Rectifier	HIPERFET Power Mosfet Q-Class IXYS IXFB50N80Q2	800 V – 50 A (25°C)
DC-link	DC Capacitor bank Electrolytic 2x2200mF/400V in series	1100mF/800V
Quasi-resonant branch	Components	IGBT
	IGBT's ESR	0.01 Ω
	Resonant inductance L_r	14 μ H
	Resonant capacitor C_r	284 nF
	Resonant frequency	80 kHz
Voltage Source Inverter	SEMIKRON 3xSKM 50 GB 123D	1200 V – 50 A (25°C)
Grid Power Transformer	Rated Power	10kVA
	Rated voltage	80V/400V

The same operative conditions of the simulations 1, 2, 3 and 4 have been fixed for the experimental prototype and the experimental response of the controlled system is shown in Figs 4.58, 4.59., 4.60 and 4.61. respectively, where the zero of the d-q axis components of the grid currents has been translated to the value of -20 A on the ordinate axis to represent these on the same figures.

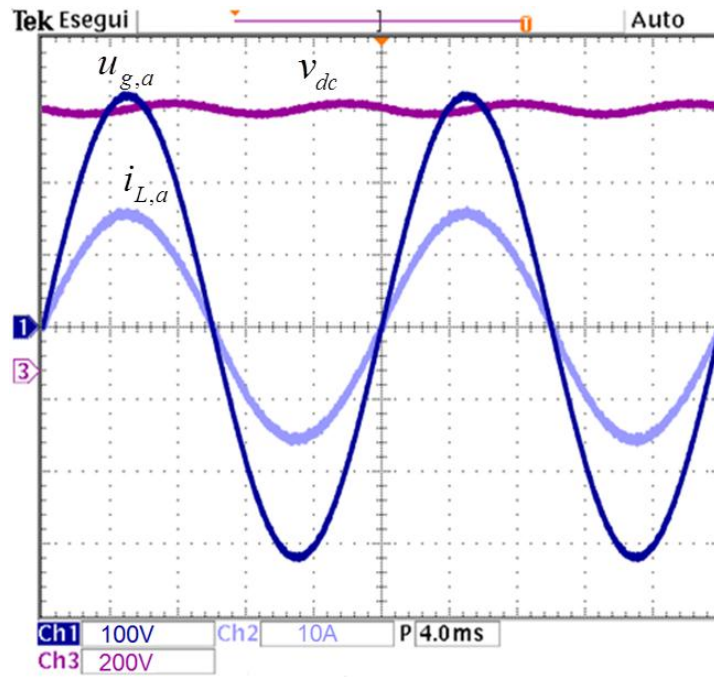


Fig. 4.58. The phase grid voltage and current and the DC-link voltage under the same operative conditions of Simulation 1.

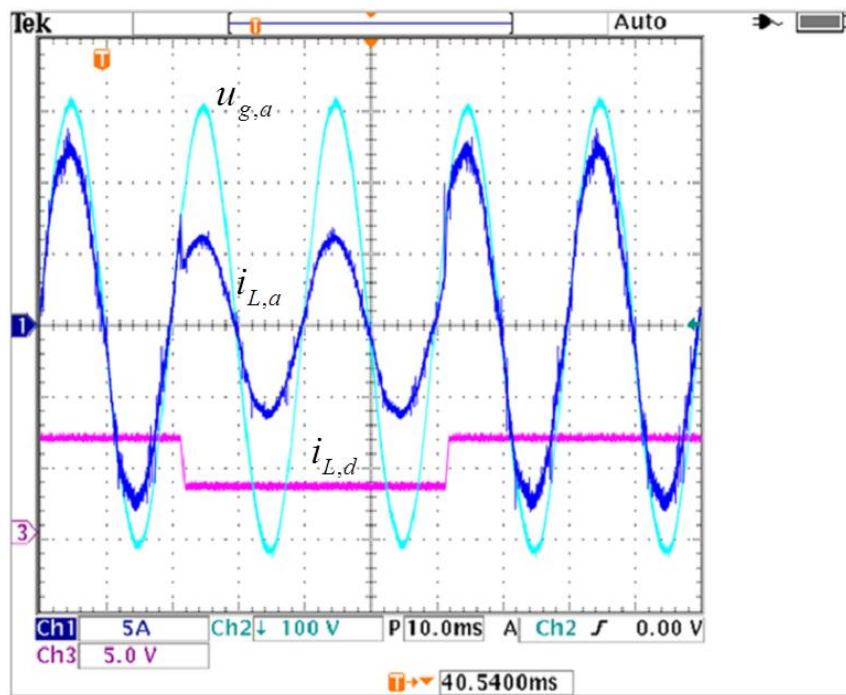


Fig. 4.59. Grid-voltage and grid-current, actual d-axis component $i_{L,d}$ of the grid current for a step change of $i_{L,d}^*$ (the same operative conditions of Simulation 2).

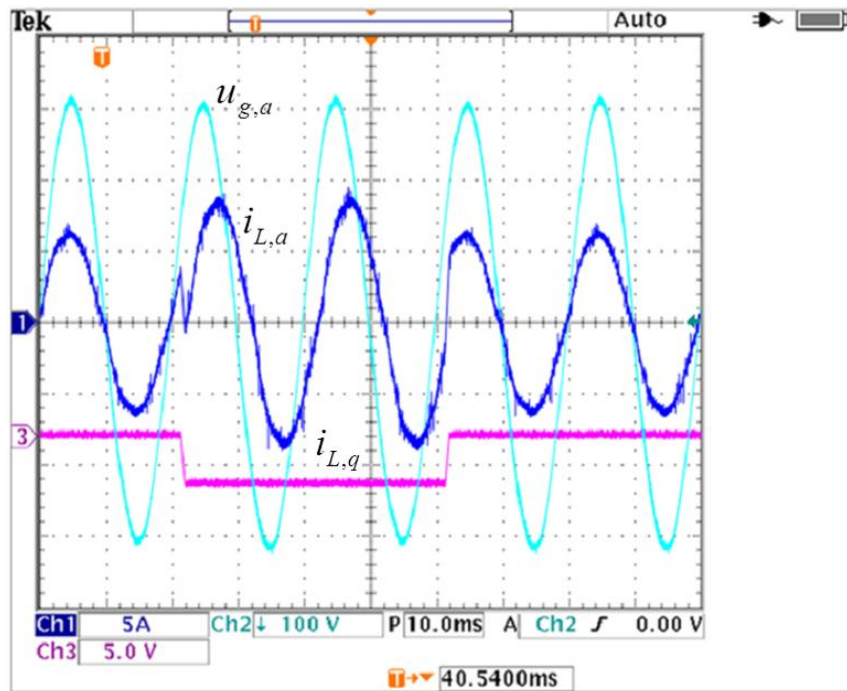


Fig. 4.60. Grid-voltage and grid-current, actual q-axis component $i_{L,q}$ of the grid current for a step change of $i_{L,q}^*$ (the same operative conditions of Simulation 3).

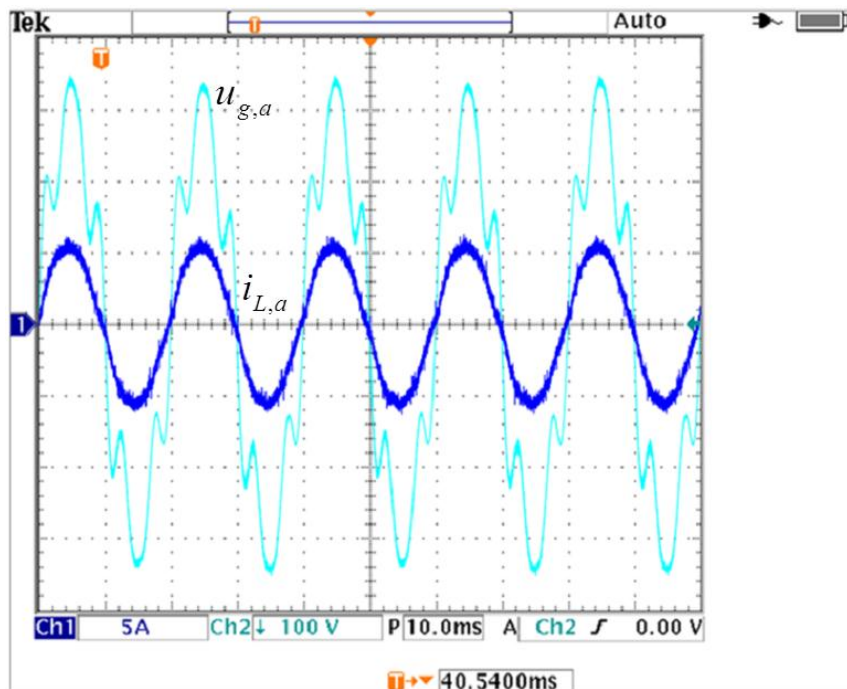


Fig. 4.61. Grid-voltage and grid-current under unbalanced conditions of grid-utility (the same operative conditions of Simulation 4)

In all the considered experimental tests the errors of d-q axis components of the grid-utility currents has been within ± 0.1 A.

Fig. 4.62. shows the DC-link voltage and current, the resonant capacitor voltage and the switch pulse signal of the IGBT of the quasi-resonant branch required to obtain a resonant frequency of 80 kHz under the same operative conditions of Simulation 1.

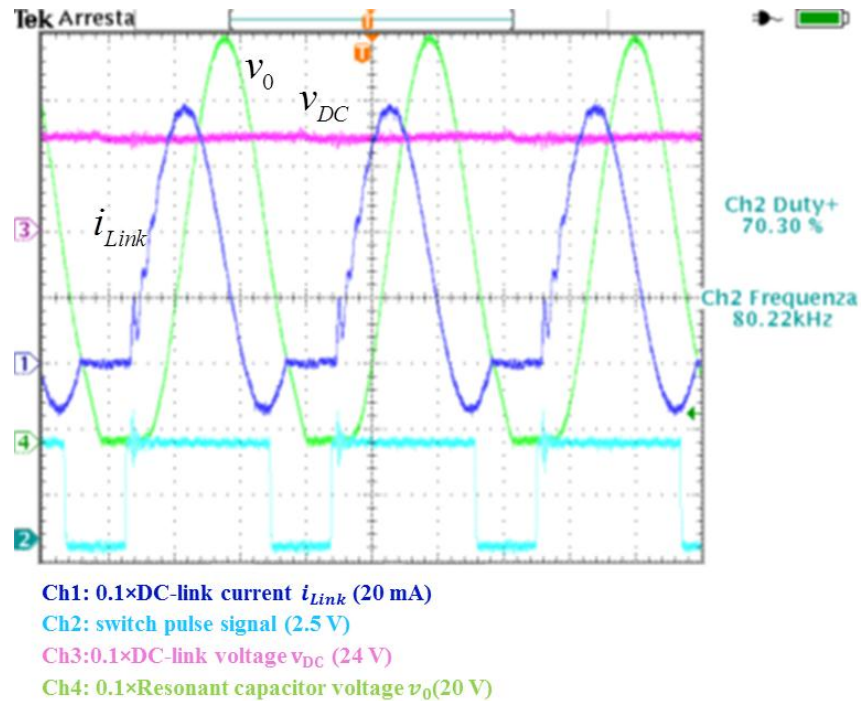


Fig. 4.62. Dc-link voltage and current, resonant capacitor voltage and switch pulse signal of IGBT of quasi-resonant branch under the same operative conditions of Simulation 1.

The Total Harmonic Distortion (THD) of the grid-current has been estimated by means of a FFT analysis of the steady-state grid-current harmonic spectra. Fig 4.63 shows the grid-current harmonic spectra where each harmonic amplitude is expressed in percentage of the amplitude of the fundamental. THD is about 4%.

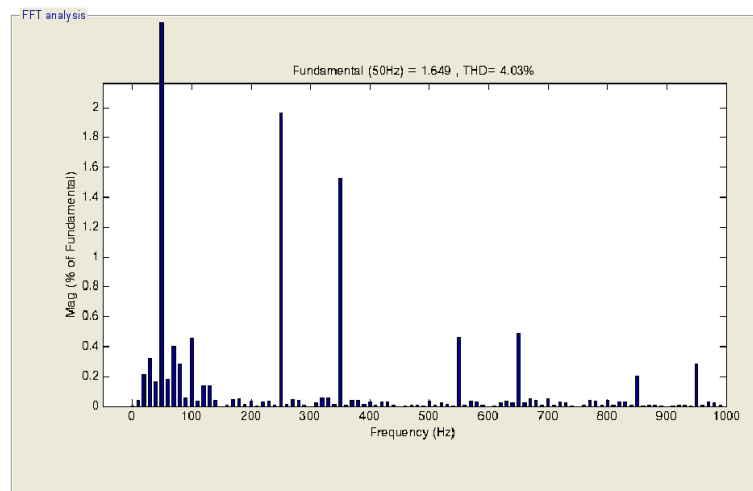


Fig. 4.63. Steady-state grid-current harmonic spectra.

Discussion of experimental results

As can be seen from the previous figures compared with the numerical results of subsection 4.1, the experimental results are in well accordance with the simulated ones in all the considered operative conditions

Thus the proposed control strategy is able to achieve the targets of the both stages of DSACPC under both balanced and unbalanced grid-utility conditions guaranteeing at same time a fast dynamic response of the controlled system.

CONCLUSIONS

In this Ph.D. thesis the design of a new Grid-connected Double-Stage AC-DC/DC-AC Power Converter (DSACPC) for a Concentrating Solar plant for Combined generation of Heat and Power (CS-CHP) is presented.

Thanks to Concentrating Solar Plant and the thermodynamic sub-system, the high-temperature heat, achieved using mirrors to concentrate the sun rays to a receiver tube crossed by thermal fluid, is converted into mechanical energy by means of a coupled Organic Rankine Cycle (ORC). So the mechanical energy outlet by turbine is input to electrical sub-system that uses it to generate electric power on the grid supply.

Since the steam cycle has a low efficiency, caused by low operating temperature (400°C for synthetic oil), and the CS-CHP has high cost of installing (i.e. the Concentrating Solar Plants are much larger than photovoltaic plant), a new Grid-connected Double-Stage AC-DC/DC-AC Power Converter (DSACPC) with Second-Order Super-Twisting Integral Sliding Mode Control for electrical sub-system is proposed, in order to maximize efficiency of the electrical sub-system so to maximize the global efficiency of proposed plan and to make competitive the grid-connected CS-CHP in small scale application.

The proposed Double Stage AC-AC Power Converter (DSACPC) consists of two fundamental parts:

- the **Stage 1** consists of a PMSG coupled in axis with turbine, a boost-type PWM rectifier and a DC-link capacitors bank; these components are controlled by means of full sliding mode control that is constituted by the Back-EMF and rotor angle sliding mode*

observer, an Integral Sliding Mode Control (ISMC) for the DC-link voltage control, a Super-Twisting Integral Sliding Mode Control (ST-ISMC1) in order to achieve a sliding mode current control of the Stage 1;

- the **Stage 2** consists of a three-phase Voltage Source Inverter (VSI) and a three-phase step-up transformer connected to the grid utility; the VSI is controlled by means of a Super-Twisting Integral Sliding Mode Control (ST-ISMC2) in order to achieve a sliding mode current control of the Stage 2.

The proposed control strategy applied both two stages of DSACPC is able to maximize the extracted energy from the thermodynamic subsystems, while to regulate the DC-link voltage and to achieve unity power factor and low distortions current.

In particular the targets of the proposed control strategy are different for the two stages of DSACPC and can be defined as follows:

for the Stage 1

- 1.a) keeping the DC-link voltage at a desired value;
- 1.b) tracking of the maximum power point draw from the thermodynamic sub-system.

for the Stage 2

- 2.a) generation of desired values of instantaneous active and reactive power on the grid utility, in the case of balanced conditions of the grid utility;
- 2.b) current harmonic rejection, in the case of unbalanced conditions of the grid utility.

For the formulation of the proposed control strategy the following means components were designed: the “Sliding Mode Observer” to estimate the electrical rotor angle and the back-EMFs of PMSG, the “Integral Sliding Mode Controller” the DC-Link voltage control, the “Second-Order Super-Twisting

Sliding Mode Controller” to realize a current control of both stages in order to achieve the fixed targets of the proposed control strategy. Each of the latter components has been designed and tested by means of simulations and an experimental prototype was carried out in order to validate the performance of the proposed control strategy.

The numerical and experimental results are explained in Section 4 and these prove the high efficiency and high performance of the full proposed control system; in fact, thanks to the proposed control law the controlled system exhibits fast dynamic response, strong robustness and good current harmonic rejection.

Moreover since the employed control strategy can regulate both the reactive and active instantaneous power given to the grid-utility under balanced conditions of the grid, the proposed system may be enclosed in a smart-grid contest thanks to its performance.

In conclusion in this Ph.D. thesis a small scale CS-CHP plant has been developed for urban area installation, using buildings roofs or factory sheds although the global efficiency is still low, but comparable with other renewable energy systems (i.e. Photovoltaic systems) for the spread in residential application.

REFERENCES

- [1] Giostri, M Binotti, M.Astolfi, P. Silva, E.Macchi, G.Manzolini, *Comparison of different solar plants based on parabolic trough technology*, Solar Energy, 86 (2012), 1208-1221.
- [2] Larson DL, *Final Report of the Coolidge solar irrigation project*. New Mexico: Sandia National Laboratories; 1983.
- [3] Price H, Hassani V., *Modular trough power plant cycle and systems analysis*, Colorado: National Renewable Energy Laboratory, 2002.
- [4] Prabhu E, *Solar trough organic Rankine electricity system (STORES) stage 1: power plant optimization and economics*, California: National Renewable Laboratory, 2006.
- [5] Pei G, Li J, Ji J. *Analysis of low temperature solar thermal electric generation using regenerative organic Rankine cycle*, Applied Thermal Eng. 2010, 30(8-9), 998-1004.
- [6] Zhuang Xu, Pengyao Ge and Dianguo Xu, *High Performance Control of a Permanent Magnet Wind Power Generation System Using an Adaptive Sliding Observer*, International Conference on Power Electronics and Drive System (2009), PEDS 2009, pp. 67-71, 2009.
- [7] S. Meo, V. Sorrentino, A. Zohoori, A. Vahedi, *Second-Order Sliding Mode Control of a Smart Inverter for Renewable Energy System*, International Review of Electrical Engineering (I.R.E.E.), vol. 9, n. 6, pp. 1090-1096, 2014.
- [8] X. Hao, T. Liu, X. Yang, L. Huang, *A Discrete-Time Integral Sliding-Mode Controller with Nonlinearity Compensation for Three-Phase Grid-connected Photovoltaic Inverter*, The 7th IEEE International Power Electronics and Motion Control Conference – ECCE Asia, 2012.

- [9] S. Meo and V. Sorrentino, *Discrete-Time Integral Variable Structure Control of Grid-Connected PV Inverter*, Journal of electrical Systems JES vol. 11, issue 1, pp. 102-116, 2015.
- [10] Bo Fan, Jiexin Pu, Gang Liu, *A Novel Study of Direct Power Control of Three-Phase Voltage Source PWM Rectifier Based on Virtual Flux*, (2013) International Review of Electrical Engineering (IREE), 8 (1), pp. 60-64, 2013.
- [11] Y. Quan, H. Nian, *Multi-resonant Based Sliding Mode Control of Grid-Connected Converter Under Distorted Grid Conditions*, Energy Conversion Congress and Exposition (ECCE), pp. 1702-1708, 2013.
- [12] Mohamed El Hachemi Benbouzid, Brice Beltran, Yassine Amirat, Sylvie Breton, *Sensorless Control of Doubly-Fed Induction Generator-Based Wind Turbines Using a High-Order Sliding Mode Observer*, (2014) International Review of Electrical Engineering (IREE), 9 (1), pp. 49-55, 2014.
- [13] A. Damiano, G. Gatto, I. Marongiu, S. Meo, A. Perfetto, A. Serpi: "A Direct-Drive Wind Turbine Control for a Wind Power Plant with an Internal DC Distribution System", International Review of Electrical Engineering (IREE), vol. 7 n. 4 (Part A), July-August 2012, pp. 4845-4856.
- [14] G. Gatto, I. Marongiu, S. Meo, A. Perfetto, A. Serpi, Predictive Control of Brushless DC Generators, International Review of Electrical Engineering (IREE), vol. 6 n. 5 (Part A), Sept.-October 2011, pp. 2368-2375.
- [15] K. Dhayalini, S. Sathiyamoorthy, C. Chirstober Asir Rajan, Evolutionary Programming based Optimal Wind and Thermal Generation Dispatch with valve point effect, International Review on Modelling and Simulations (IREMOS), Vol 7, No 4 (2014).
- [16] Kamel Djamel-Eddine Kerrouche, Abdelkader Mezouar, Larbi Boumediene, Kheira Belgacem, Modeling and Optimum Power Control based DFIG Wind Energy Conversion System, International Review of Electrical Engineering (IREE), Vol 9, No 1 (2014).
- [17] Smitha Elsa Peter, Santosh Kulkarni, I. Jacob Raglend, Sishaj P. Simon, Wavelet Based Spike Propagation Neural Network (WSPNN) for Wind Power Forecasting, International Review on Modelling and Simulations (IREMOS), Vol 6, No 5 (2013).
- [18] Navdeep Singh, Vineeta Agrawal, A Review on Power Quality Enhanced Converter of Permanent Magnet Synchronous Wind Generator,

International Review of Electrical Engineering (IREE), Vol 8, No 6 (2013).

- [19] V. Utkin, J. Guldner, J. Shi, *Sliding Mode Control in Electromechanical Systems*, Taylor & Francis, Chap. 2, pp. 24-27, 1999.
- [20] R. A. DeCarlo, S. H. Zak, G. P. Matthews, *Variable Structure Control of Nonlinear Multivariable Systems: A Tutorial*, Proceeding of the IEEE, Vol. 76, No. 3, pp. 212-232, 1988.
- [21] V. Utkin, J. Guldner, J. Shi, *Sliding Mode Control in Electromechanical Systems*, Taylor & Francis, Chap. 8, pp. 139-153, 1999.
- [22] V. Utkin, J. Guldner, J. Shi, *Sliding Mode Control in Electromechanical Systems*, Taylor & Francis, Chap. 9 pp. 160-161, 1999.
- [23] V. Utkin, J. Guldner, J. Shi, *Sliding Mode Control in Electromechanical Systems*, Taylor & Francis, Chap. 7 pp. 117-118, 1999.
- [24] D. Milosavljevic, *General condition for existence of a quasi-sliding mode on the switching hyperplane in discrete variable structure system*, Automat. Remote Contr., vol. 46, pp. 307-314, 1985.
- [25] K. Abidi, J. X. Xu and Y. Xinghuo, *On the discrete-time integral sliding mode control*, IEEE Trans. Autom. Control, vol. 52, pp. 709-715, 2007.
- [26] W. C. Su, S. Drakunov and U. Ozguner, *An $O(T^2)$ boundary layer in sliding mode for sampled-data systems*, IEEE Trans. Autom. Control, vol. 45, no. 3, pp. 482-485, 2000.
- [27] A. Levant (L.V. Levantovsky), *Sliding order and sliding accuracy in sliding mode control*, International Journal of Control, vol. 58, no. 6, pp. 1247-1263, 1993.
- [28] W. Perruquetti, J. P. Barbot, *Sliding Mode Control in Engineering*, Marcel Dekker, Inc., Chap. 3, 2002.
- [29] S. Drakunov, V. Utkin, *Sliding Mode Observers. Tutorial*, Proceedings of the 34th IEEE Conference on Decision & Control, vol. 4, pp. 3376-3378, 1995.
- [30] V. Utkin, J. Guldner, J. Shi, *Sliding Mode Control in Electromechanical Systems*, Taylor & Francis, Chap. 6, pp. 103-106, 1999.
- [31] V. Utkin, J. Guldner, J. Shi, *Sliding Mode Control in Electromechanical Systems*, Taylor & Francis, Chap. 11, pp. 251-252, 1999.

- [32] Zhuang Xu, Pengyao Ge and Dianguo Xu, *High Performance Control of a Permanent Magnet Wind Power Generation System Using an Adaptive Sliding Observer*, International Conference on Power Electronics and Drive System (PEDS), pp. 67-71, 2009.
- [33] Z.Q. Zhu, D. Howe, C.C. Chan, *Improved analytical model for predicting the magnetic field distribution in brushless permanent-magnet machines*, IEEE transactions on magnetics, vol. 38, no. 1, pp. 229-238, 2002.
- [34] Z.Q. Zhu, D. Howe, *Instantaneous magnetic field distribution in brushless permanent magnet dc motors, part I: open-circuit field*, IEEE transactions on magnetics, vol. 38, no. 1, pp. 124-135, 1993.
- [35] F. Meier, *Permanent-Magnet Synchronous Machines with Non-Overlapping Concentrated Windings for Low-Speed Direct-Drive Applications*, Doctoral thesis, Royal Institute of Technology, Stockholm, 2008.
- [36] S. Meier, *Theoretical design of surface-mounted pm-motors with field-weakening capability*, Master thesis, Royal Institute of Technology, Stockholm, 2002, pp. 24 and 71 for slot leakage inductance and 28-30 for iron losses.
- [37] Z.Q. Zhu, D. Howe, *Instantaneous magnetic field distribution in brushless permanent magnet dc motors, part II: armature-reaction field*, IEEE transactions on magnetics, vol. 38, no. 1, pp. 124-135, 1993.
- [38] C. Sadarangani, *Electrical machines - Design and analysis of induction and permanent magnet motors*, Department of electrical machines and power electronics, Royal Institute of Technology, 2000.
- [39] F. Magnussen, C. Sadarangani, *Winding factors and joule losses of permanent magnet machines with concentrated windings*, Electric Machines and Drives Conference, (IEMDC 2003), Vol. 1, pp. 333-339, 2003.